University of Genova

PhD school in science and technology for engineering

PhD course in fluid dynamics and environmental processes engineering

Cycle XXVIII

PhD Thesis

Mathematical models of fluid motion in the vitreous chamber of the human eye

Candidate: Krystyna Isakova

Supervisor: Rodolfo Repetto

Co-advisor: Jan Oscar Pralits

April 27, 2016

Contents

1 Introduction **1**
- 1.1 Anatomy of the eye . . . 1
- 1.2 Functionality and physiological properties of the vitreous humor . . . 2
- 1.3 Retinal detachment . . . 4
  - 1.3.1 Posterior vitreous detachment . . . 4
  - 1.3.2 Types of retinal detachment . . . 5
- 1.4 Treatments for retinal detachment . . . 6
  - 1.4.1 Treatments for retinal breaks . . . 6
  - 1.4.2 Treatment for retinal detachment . . . 6
- 1.5 Tamponade fluids . . . 7
- 1.6 Aims of the thesis . . . 10

2 Mathematical models of vitreoretinal tractions **12**
- 2.1 Fluid motion in a periodically rotating sphere . . . 14
  - 2.1.1 Mathematical formulation . . . 14
  - 2.1.2 Results . . . 16
  - 2.1.3 Discussion . . . 21
- 2.2 Vitreoschisis . . . 22
  - 2.2.1 Mathematical formulation. Two-dimensional model . . . 23
  - 2.2.2 Mathematical modeling of vitreoschisis in a spherical domain . . . 28
  - 2.2.3 Results . . . 32
  - 2.2.4 Discussion . . . 38
- 2.3 Vitreous humor with inhomogeneous properties . . . 40
  - 2.3.1 Problem definition . . . 40
  - 2.3.2 Leading order problem (δ^0) . . . 41
  - 2.3.3 First order problem(δ^1) . . . 42
  - 2.3.4 Results . . . 45
  - 2.3.5 Discussion . . . 46

3 Mathematical models of the vitreous chamber in the presence of hydrophobic tamponade fluids **48**
- 3.1 Equilibrium shape of the aqueous humour-vitreous substitute interface in vitrectomized eyes . . . 49
  - 3.1.1 Description of the model . . . 50
  - 3.1.2 Model geometry . . . 50
  - 3.1.3 Model validation . . . 52

3.1.4 Results . . . 55
3.1.5 Discussion . . . 62
3.2 A simple model of the flow of two immiscible fluids in a sphere . . . 64
3.2.1 Mathematical formulation . . . 64
3.2.2 Results . . . 67
3.2.3 Discussion . . . 68
3.3 Linear stability of the interface between aqueous humor and vitreous substitutes after vireoretinal surgery . . . 69
3.3.1 Mathematical formulation . . . 70
3.3.2 Model validation . . . 74
3.3.3 Energy analysis . . . 75
3.3.4 Estimation of the range of variability of the dimensionless parameters 76
3.3.5 Results . . . 76
3.3.6 Discussion . . . 81

4 Conclusions **84**

Appendices **87**

A Volume of fluids method **88**

B Basic concepts of elasticity **90**

Bibliography **93**

Summary of the thesis

In this thesis we present mathematical models of the flow in the vitreous chamber of the eye, both in the presence of the natural vitreous humor and of tamponade fluids, injected into the vitreous chamber after vitrectomy. In the following we provide a short description of the contents of each chapter of the thesis to improve its readability.

Chapter 1: Introduction

Contents of the chapter. In this chapter we introduce the topics treated in the thesis, giving a short introduction about the anatomy, physiology and diseases of the eye and describing the main aims of the work.

Chapter 2: Mathematical models of vitreoretinal tractions

Contents of the chapter. This chapter is devoted to investigate the motion of the vitreous humor in the eye during eye rotations, with the aim of understanding the generation of vitreoretinal tractions. We consider the case of normal eyes as well as eyes with different pathologies, such as vitreous humor liquefaction, vitreoschisis and focal vitreoretinal tractions. The main objective of the models proposed in this chapter is to obtain a better understanding of the stress generation and distribution on the retina during eye rotations. Throughout this chapter we model the vitreous chamber as a rigid sphere.

2.1 Fluid motion in periodically rotating sphere

The model presented in this section has already been proposed by other authors [1, 2], but it serves as the basis for what follows in the next sections. We consider the flow of a fluid (viscous or viscoelastic) contained in a rigid, hollow sphere that performs small amplitude harmonic torsional oscillations. We study how the stress on the retina depends on the viscosity and how results change when viscoelasticity is accounted for, which applies to the case of the natural healthy vitreous.

In the case of a purely viscous fluid, the maximum wall shear stress on the retina grows with increasing viscosity of the fluid in a highly nonlinear way and reaches an asymptotic value in the limit of high viscosity, which can be computed analytically.

Since the real vitreous humor is a viscoelastic fluid we also consider the case of a fluid with an elastic behavior. The results show that the motion of a viscoelastic fluid can be resonantly excited by eye rotations, leading to large values of the shear stress on the retina.

2.2 Vitreoschisis

With aging the vitreous humor undergoes liquefaction and also the vitreous cortex (the

outermost layer of the vitreous) progressively gets thinner. During the liquefaction and thinning processes small pockets of liquefied vitreous humor start to form and slowly move through the thin cortex layer to settle between the cortex and the retina. This can lead to the detachment of the cortex from the retina, a process called posterior vitreous detachment (PVD), which is harmless under normal circumstances.

However, in some cases liquefaction and cortex thinning do not occur simultaneously: the vitreous gel may liquefy while the cortex is still thick and tightly attached to the retina. This leads to an anomalous PVD, which may cause pathological conditions in the eye. Vitreoschisis is the consequence of an anomalous PVD with such a strong vitreo-retinal adhesion in some regions that the posterior vitreous cortex splits, leaving a vitreous layer attached to the retina, while the remainder of the vitreous collapses forward.

In this section we present a simple, yet instructive, model of vitreoschisis and, in particular, we study how the stresses exerted on the retina are spatially distributed in the presence of vitreoschisis. We adopt two different models, two and three-dimensional respectively, which are based on same assumptions. We assume that the split in the vitreous is very thin (which is realistic) with respect to the size of the domain. According to this view the vitreous split is thought of as a region in which the no-slip condition of the vitreous on the retina is partially relaxed. Thus we study vitreous motion induced by eye rotations in the presence of a spatially variable attachment condition of the vitreous on the retina (slip condition). We assume that the slip length is small, which allows us to adopt a perturbation approach. In the case of the simple two-dimensional model the solution can be found entirely analytically, and this makes it easy to understand and interpret the results. In the case of the three-dimensional spherical model the solution is also analytical, but the spatially variable slip condition needs to be expanded in vector spherical harmonics (which is done numerically). Qualitatively, the results of the two models are in the agreement.

The results show that in the regions of reattachment of the vitreous on the retina (at the boundary of the vitreous split) the retina experiences a strong increase of the wall shear stress with respect to the normal condition, i.e. when no split is present. The results confirm the clinical observation that the presence of the vitreoschisis locally increases tangential vitreoretinal tractions and thus provide a mechanical explanation of the possible occurrence of pathological conditions, such as macular tears and macular holes, which are the main risk factors for retinal detachment.

2.3 Vitreous humor with inhomogeneous properties

The natural healthy vitreous humor is not homogeneous throughout the vitreous chamber. In addition, it undergoes liquefaction with aging leading to the generation of liquid lacunae and regions of tight attachments with the retina that are related to locally higher values of the elastic modulus of the fluid. In this section we account for spatial variations of the mechanical properties of the vitreous (its elastic and viscous component).

Again, we assume that such variations are small, which allows us to adopt a perturbation approach. The model improves our understanding of the stress distribution on the retina during eye rotations.

Chapter 3. Mathematical models of the vitreous chamber in the presence of hydrophobic tamponade fluids

Contents of the chapter. Typically, tamponade fluids used during vitrectomy in order to

treat retinal detachments are hydrophobic. Owing to this property a layer of aqueous humor invariably forms between the retina and the vitreous substitute, at least in certain regions of the eye. The shape of the interface between the vitreous substitute and the aqueous is highly curved, due to surface tension effects. This affects the region of the retina effectively tamponated. During eye rotations the existence of a thin layer of aqueous that separates the tamponade from the retina has important mechanical implications, both for the stresses experienced on the retina and also for the possible occurrence of instability of the interface between the two fluids that might initiate the process of interface breakdown, eventually leading to emulsification (a common complication associated with the use of hydrophobic tamponades).

In this chapter we present mathematical models that help us shed some light onto these problems.

3.1 Equilibrium shape of the aqueous humor-vitreous substitute interface in vitrectomized eyes

For a given volume of tamponade fluid injected into the eye, the tamponated retinal surface is strongly affected by the shape of the interface between the tamponade fluid and the aqueous humor. In this section we study the equilibrium configuration of the interface between the tamponade fluid and aqueous humor. This depends on the physical properties of both fluids, in particular, on density difference, surface tension, contact angle with the retina and, obviously, also on head orientation.

We consider the two most commonly used tamponade fluids: silicone oil and intraocular gas. Different shapes of the vitreous chamber are studied. We first consider idealized yet realistic geometries of emmetropic and myopic eyes and also consider real eye shapes reconstructed from MRI-images. The shape of the interface between aqueous and vitreous substitute is determined numerically using the free software OpenFOAM and a solver based on the volume of fluid method.

The results show that for patients in the upright position the geometry of the vitreous chamber has a significant impact on the final equilibrium configuration of the interface between two fluids. Gases have better tamponating properties then silicone oils. We also find that the tamponating efficacy is reduced in highly myopic eyes.

This model can be applied to the eyes with pathological geometries which makes it a valuable tool for the clinical application. **3.2 A simple model of the flow of two immiscible fluids in a sphere**

In this section we adopt an idealized geometry consisting of a rigid sphere performing harmonic torsional oscillations, filled with two immiscible fluids (aqueous humor and vitreous substitute) arranged concentrically, with the aqueous in the external layer. In other words we assume that the thickness of the aqueous layer is uniform over the domain. This is not a very realistic assumption but it allows us to solve the problem for the fluid motion analytically and the obtained solution is likely to be approximately valid at least in the regions where the thickness on the aqueous layer in very thin compared to the radius of the sphere. We then compute the maximum value of the shear stress on the wall (retina).

The results show that the maximum wall shear stress on the retina can be significantly reduced in the presence of a layer of aqueous humor with respect to the case of single fluid filling the domain, even if the viscosity of the vitreous substitute is very large. Therefore, the

possible existence of an aqueous layer should be accounted for when estimating the mechanical stresses on the retina after injection of a vitreous substitute.

This work has been published in [3].

3.3 Linear stability of the interface between aqueous humor and vitreous substitute after vitreoretinal surgery

A common complication after vitrectomy is emulsification, i.e. formation of droplets of oil in the aqueous solution, which may travel to the anterior chamber of the eye. It is believed that mechanics plays an important role in this process. We performed a stability analysis of the aqueous humor-vitreous substitute interface by considering a simple two-dimensional case following the assumption that the thickness of the aqueous layer is much smaller then the radius of the eye.

The model consists of two fluids superposed over a flat surface, that oscillates harmonically. The aqueous humor occupies the region between the wall and the interface between two fluids and tamponade occupies the region from the interface to infinity. We study the linear stability of the interface with respect to two-dimensional perturbations using the normal mode analysis and assuming quasi-steady flow conditions.

We find that instability of the interface is possible in a range of parameters that are relevant for the problem that motivates the analysis. This suggests that shear instability is likely a possible mechanism triggering the onset of vitreous substitute-aqueous interface breakdown.

This work has been published in [4] and was chosen as *Research Highlights* in the December issue 2014 in Physics of Fluids.

Chapter 4: Conclusions

Contents of the chapter. We summarize in this chapter the main findings of the thesis and discuss their clinical implications. We, finally, outline some possible future developments.

Chapter 1

Introduction

1.1 Anatomy of the eye

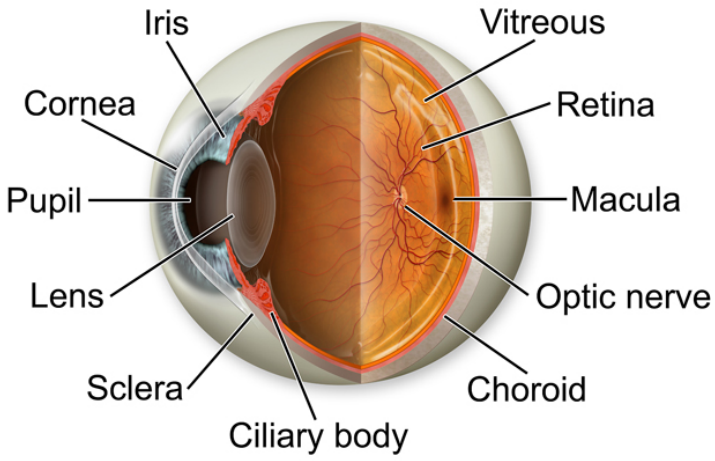

Figure 1.1.1: Cross-section of the human eye with an indication of its main components

The structure of the human eye enables it to receive light stimuli from the environment, and deliver these stimuli to the brain in the form of electrical signals. The eye has a nearly spherical shape; its antero-posterior and nasal-temporal lengths are about 24.2 mm [5] and its superior-inferior length in the normal eye is usually slightly larger. On the other hand, in myopic eyes the axial length is larger then the vertical one [6].

The interior of the eye can be divided into three different chambers: **anterior**, **posterior** and **vitreous chamber**. The anterior chamber is bounded by the cornea, the iris and the lens, while the posterior chamber is the region between the lens and the iris. Anterior and posterior chambers are connected through the pupil and they are filled with aqueous humor, a transparent liquid with properties similar to those of water, which is produced by the ciliary body. The aqueous humor delivers the nutrients to the cornea and the lens, which are avascular tissues.

The vitreous chamber is located in the back part of the eye and is bounded by the lens, the ciliary body and the retina. It is filled with the vitreous humor, a viscoelastic fluid, the functionality of which will be considered later on in this thesis.

The main **components of the eye** are the following:

Cornea The cornea is the clear front window of the eye, which transmits and contributes to focus the light on the retina.

Iris This is the colored part of the eye, which regulates the amount of light entering the eye. When there is a bright light, the iris contracts the pupil to let less light in. On the other hand, when the light is dim the iris opens up the pupil to let in more light.

Pupil It is the dark central opening in the middle of the iris and connects anterior and posterior chambers.

Lens It contributes to focus light rays onto the retina. The lens is a transparent avascular tissue. With age it often deteriorates, becoming stiffer and decreasing our capacity of focusing at short distances. With advancing age the lens also often loses its transparency (cataract). In such cases it can be replaced by artificial intraocular lenses.

Sclera The white outer external coat of the eye, which provides mechanical strength to the eye ball.

Ciliary body This is a muscular structure located behind the iris, which allows lens accommodation to occur. It is also responsible for the production of aqueous humor.

Vitreous humor It is the clear gel-like substance filling the central cavity of the eye.

Retina The retina is the layer lining the inner part of the back of the eye. The retina senses light and creates electrical impulses that are sent through the optic nerve to the brain.

Macula This is the area of the retina that contains special light-sensitive cells. In the macula these cells allow us to see fine details clearly in the center of our visual field. Deterioration of the macula is a common condition as we get older.

Choroid It is a layer containing blood vessels that lines the back of the eye and is located between the retina and the sclera.

Optic nerve It consists of more than a million nerve fibers, that carry visual signals from the retina to the brain. Glaucoma is a very serious condition that affects the optic nerve.

Retinal pigment epithelium is the pigmented cell layer located just outside the retina and it is attached to the chorioid. The RPE closely interacts with photoreceptors in the maintenance of visual function. The retinal pigment eptihelium also serves as the limiting transport factor that maintains the retinal environment by supplying small molecules while remaining a tight barrier to choroidal blood borne substances. It transports ions, water, and metabolic end products from the subretinal space to the blood.

1.2 Functionality and physiological properties of the vitreous humor

The vitreous humor is a clear gel-like substance that occupies the space between the lens and the retina of the eye. Transparency of the vitreous is obviously necessary for the functionality

of the eye. The vitreous humor is a viscoelastic, avascular fluid that is not actively regenerated as, for example is aqueous humor. Vitreous mechanical properties have been studied by several authors [7, 8, 9, 10].

The vitreous provides mechanical support to the eye. By filling up the vitreous chamber it prevents the retinal from detaching from the pigment epithelium (the layer just outer of the retina) and inhibits excessive deformation of the eye ball by absorbing external forces. It exchanges substances with the ciliary body and the retina.

The vitreous humor is composed of a highly-hydrated double network of protein fibrils and charged polysaccharide chains (figure 1.2.1). By the weight, vitreous is 99% water and 0.9% salts [11]. The remaining 0.1% is divided between protein and polysaccharide components. Most of the protein is found in collagen fibrils. The high concentration of protein fibrils in the vitreous base drops as the collagen fibrils fan out and fill the vitreous cavity. After the fibrils diverge they approach the retina at various points around the periphery and insert into the inner limiting membrane where they turn and run in the posterior direction to the optic nerve, following the curvature of the eye [12].

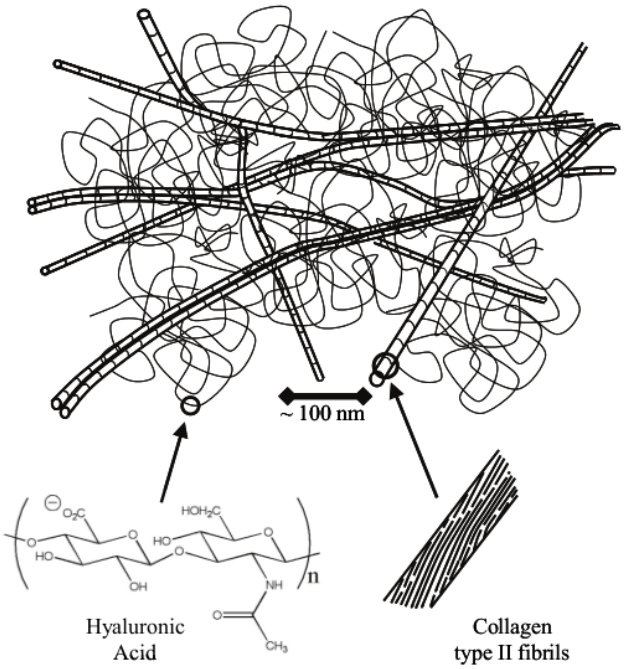

Figure 1.2.1: Sketch of the network structure of the vitreous. The vitreous is composed of a highly-swollen double network of collagen type II fibrils (15 nm in diameter) and hyaluronic acid. Taken from [11].

Collagen fibrils are hydrophobic and adhere to each other when they come in contact. In addition, a sufficient number of fibrils are also oriented nasal-temporally to form a fully crosslinked network. The network of collagen fibrils has been presumed to be responsible for the mechanical properties of the vitreous, because of the load-bearing capacity of collagen. Swollen hyaluronan polysaccharide chains play a passive role in the vitreous by filling the space between the fibrils to prevent extensive aggregation.

As it has been shown, the vitreous humor has a complicated and non-homogeneous structure. It is important from the clinical point of view to obtain a better understanding of vitreous structure and its mechanical properties, since it is an essential step forward in developing vitreous replacements, needed for various purposes and also because it is important to understand the generation of vitreoretinal tractions that might be responsible for the creating retinal breaks.

1.3 Retinal detachment

1.3.1 Posterior vitreous detachment

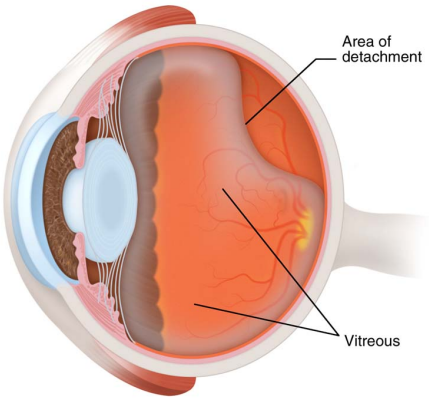

Figure 1.3.1: Posterior vitreous detachment

The healthy vitreous has a gel-like structure. As we age, the gel often undergoes liquefaction, shrinks, and eventually separates from the retina in the back of the eye. This process is called posterior vitreous detachment (PVD) (figure 1.3.1). PVD is very common and occurs in most adults. PVD may also occur in younger individuals who have undergone cataract surgery or are very nearsighted.

When PVD occurs, floaters are usually noticed. Floaters are small specks that move in and out of your field of vision. They maybe more noticeable when looking at a plain background. Another common symptom of a PVD is flashes of light in the periphery of the visual field, particularly in low ambient light. These flashes are the result of the retina being tugged on by the separating vitreous.

Normally PVD does not lead to any complications. However, if the retina is weak or the vitreous gel is abnormal, a retinal tear can occur (figure 1.3.2). If a retina tear is associated with a PVD and it is not treated with laser, the patient is at high risk of developing a **retinal detachment** and treatment will be necessary.

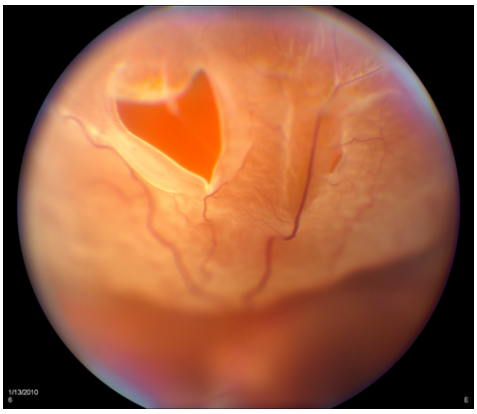

Figure 1.3.2: Teared retina as a result of PVD.

1.3.2 Types of retinal detachment

Retinal detachment is a serious sight threatening condition. There are three different categories of retinal detachment.

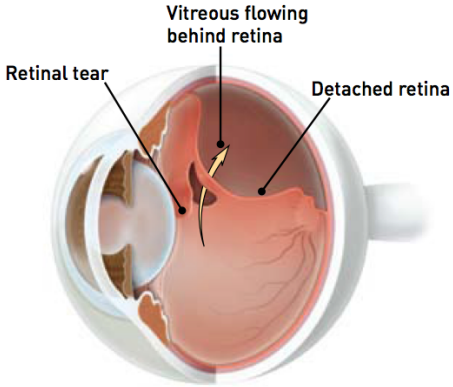

Figure 1.3.3: Retinal detachment as a result of PVD.

Rhegmatogenous Retinal Detachment Rhegmatogenous retinal detachment is the most common type of detachment. It occurs when the liquefied vitreous passes through a retinal break or tear and accumulates under the retina, separating it from the pigment epithelium. Symptoms include flashes and floaters. In the presence of retinal break, retinal detachment is likely to occur. In most cases rhegmatogenous retinal detachment first occurs in the peripheral retina, which affects side vision. As the detachment extends towards the macula, central vision will be lost, unless the detachment is treated. The patient may notice this as a "veil" or a "curtain" that obscures the peripheral vision and slowly encroaches on the center. With early surgical repair central vision can be preserved if the macula has not detached. In the case when the macula is already detached, visual recovery will not be complete. About 90% of rhegmatogenous retinal detachments can be repaired if treated during their initial stage.

Exudative Retinal Detachment It occurs when natural pumping of fluid outwards by the

retinal pigment epithelium is impaired, or fluid leaks through the normally impermeable retinal pigment epithelium from the underlying layer of blood vessels (choroid). Several conditions, ranging from inflammatory diseases, tumors, connective tissue diseases and macular degenerative conditions can cause this type of retinal detachment.

Tractional Retinal Detachment This occurs when a scar tissue within the vitreous cavity pulls on the retina, eventually causing it to detach. There are several conditions that can cause this type of detachment, including proliferative diabetics retinopathy and proliferative vitreoretinopathy (PVR). PVR is the most common reason why a rhegmatogenous retinal detachment repair fails (5-10% of the cases).

If the traction retinal detachment only involves the peripheral retina, surgery may not be necessary immediately. Close monitoring will be necessary to ensure it is not threatening the macula.

If the detachment involves the macula, the traction retinal detachment will need to be operated on. Most often the Trans Pars Plana Vitrectomy (TPPV) procedure is used to repair the detachment and often a scleral buckle will be used in conjunction with the TPPV.

The underlying cause of the detachment will ultimately determine the overall success of treatment. While some traction retinal detachment are easily repairable, others may be impossible to treat successfully.

1.4 Treatments for retinal detachment

1.4.1 Treatments for retinal breaks

The key ingredient to prevent retinal detachment is early detection of retinal tears. The most commonly way to treat a retinal break is a laser, which seals the tear and, thus, prevents liquefied vitreous from passing through the retinal break. Another option is cryotherapy, which produces a scar around the break by freezing it. Both treatments have a high rate of success in helping to prevent RD.

1.4.2 Treatment for retinal detachment

There are three types of surgical procedures that can be used to correct a RD. They are listed below.

Pneumatic Retinopexy In some cases RD can be treated by injecting a gas bubble into the eye and treating the retinal tear with either laser or cryopexy (freezing). Unfortunately, the overall success rate tends to be lower then other treatments. Some patients, however, are ideal candidates for this procedure which allows them to avoid unnecessary surgery.

Vitrectomy The vitrectomy, or Trans Pars Plana Vitrectomy (TPPV), is the most common way to treat the RD. At first the vitreous humor and subretinal fluid are removed from the eye by making small incisions into the eye ball. Then retinal tears are treated with laser to cause a permanent adhesive scar and prevent future detachment. At the last stage of the surgery a vitreous substitute (tamponade fluid) is injected into the eye chamber. The primary role of vitreous substitutes is to interrupt the communication

that was established through the retinal break between the subretinal space/retinal pigment epithelial cells and the pre-retinal space. Various fluids can be used during vitrectomy, depending on the particular condition of the patient. The various fluid tamponades and their properties will be considered later on in this work. Usually, a specific head position is required to ensure that the retina remains attached. When gas is used as a tamponade fluid no additional surgery is required since it dissolves on its own after some time. When the silicone oil is used during the surgery additional operation is needed in order to remove tamponade fluid from the vitreous chamber. Otherwise undesirable consequences might occur.

Scleral Buckling This is the oldest surgical procedure in the practice of RD treatment. A small piece of silicone is sutured around the eye in such a way that it indents the eyeball and brings the retinal break back in contact with its outer layers.

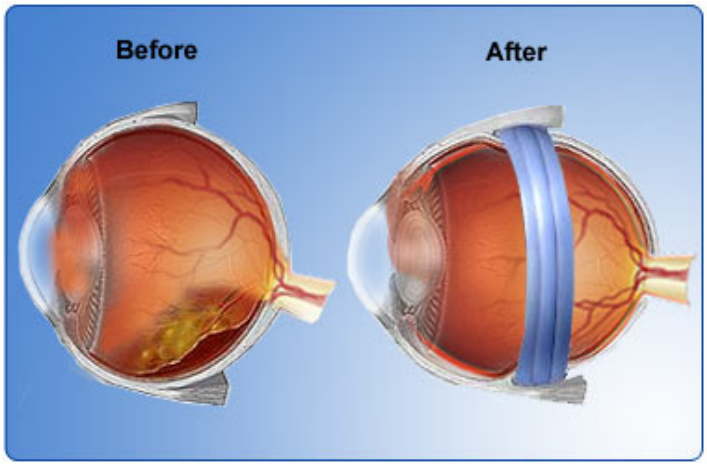

Figure 1.4.1: Scleral buckle surgery. A small piece of silicone is sutured around the eye in order to close the retinal breaks.

This allows the subretinal fluid to reabsorb and the retina to reattach. Sometimes an air or gas bubble is injected at the time of surgery to aid reattachment of the retina. One of the main advantages of the scleral buckling is that there is no need in postoperative positioning and no vitreous is removed.

1.5 Tamponade fluids

RD and some other pathologies require partial or total vitreous removal [8]. Presently, the role of intraocular vitreal substitutes is to ensure retinal adherence after cryo or laser retinopexy. One of the main challenges in vitreous substitute development is the control of inflammation. Interaction with intraocular anatomy and physiology as well as intraocular drug delivery are the main objectives for future tamponade fluids. Currently available long-term vitreous substitutes always have some disadvantages, which leaves the need of funding ideal vitreous substitute still an open problem. In many cases additional surgery is needed to remove the vitreous substitute after a certain amount of time.

The ideal vitreous substitutes have to meet a wide range of requirements (see Table 3 in

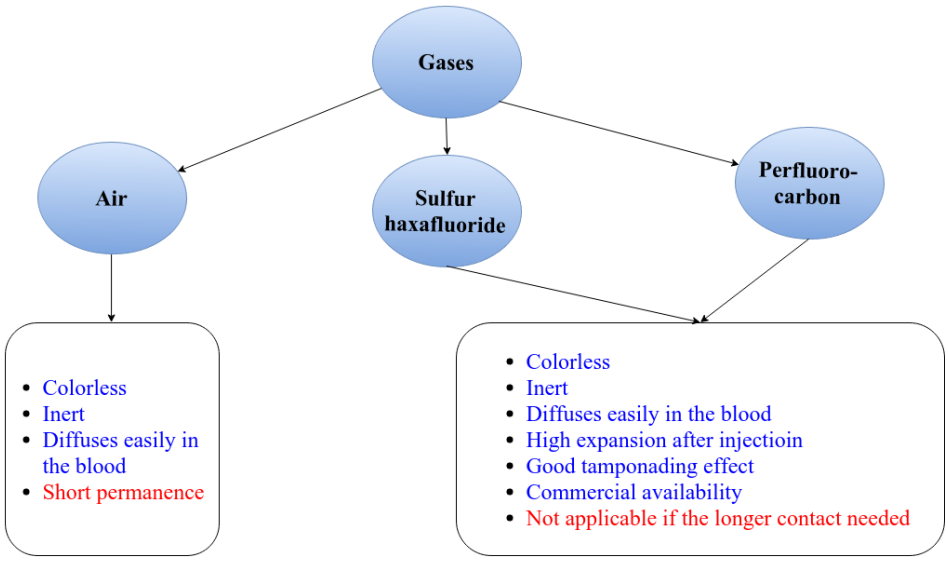

Figure 1.5.1: Three most commonly used gases at a tamponade fluids during vitrectomy. Advantages (blue) and disadvantages (red) are listed below. The main advantage of the intraocular gases is that no additional surgery is required which in not the case when liquid tamponade is used.

[13]). All currently available vitreous substitutes can be divided into two main categories: **gases** (figure 1.5.1) and **liquids** (figure 1.5.2). The choice depends on the particular case, i.e. type of RD, presence (and number) of macular holes etc.

Historically, the first gas injected into the vitreous camber was *air*. It is colorless and inert, diffuses easily in the blood circulation, reducing the tamponating effect in a few days and its naturally replaced by aqueous humor produced by the metabolism of ciliary body [14, 15]. Nowadays, however, other types of gases, such as sulfur hexafluoride, perfluoroethane and perfluorocarbon are used in pneumatic retinopexy and vitreoretinal surgery, as for their longer permanence compared to air [16, 17].

The intraocular gas bubble has buoyancy that keeps the retina against the pigment epithelium. The tamponade effect is conditioned by the dimension and position of the bubble and therefore by the position of patient's head [18, 19].

Saline solutions, perfluorocarbon liquids, semifluorinated alkanes and silicone oils are making the group of **liquid** tamponade fluids. Each of them has advantages and disadvantages with respect to others. The physical characteristics of *saline solution* are close to those of aqueous humor (transparency, refractive index and density [20]). Saline solutions are used as temporary vitreous substitutes during exchange with air or other liquids.

Perfluorocarbon liquids are hydrophobic and lipophobic substances used as a temporary tamponades to unfold and stabilize the retina during surgical manipulation. They have to be removed at the end of the surgical procedure [21, 22]. If left after the surgery, these substances may cause retinal toxicity and intraocular inflammatory reactions, and, due to their high immiscibility with water, they could form an emulsion.

The most commonly used fluids during vitrectomy are the *silicone oils*. Their refractive index are similar to that of the vitreous humor, the density is slightly lower than water and the kinematic viscosity may vary from 10^{-3} to $5 \cdot 10^{-3}$ m^2/s [23]. Due to their chemical inertness

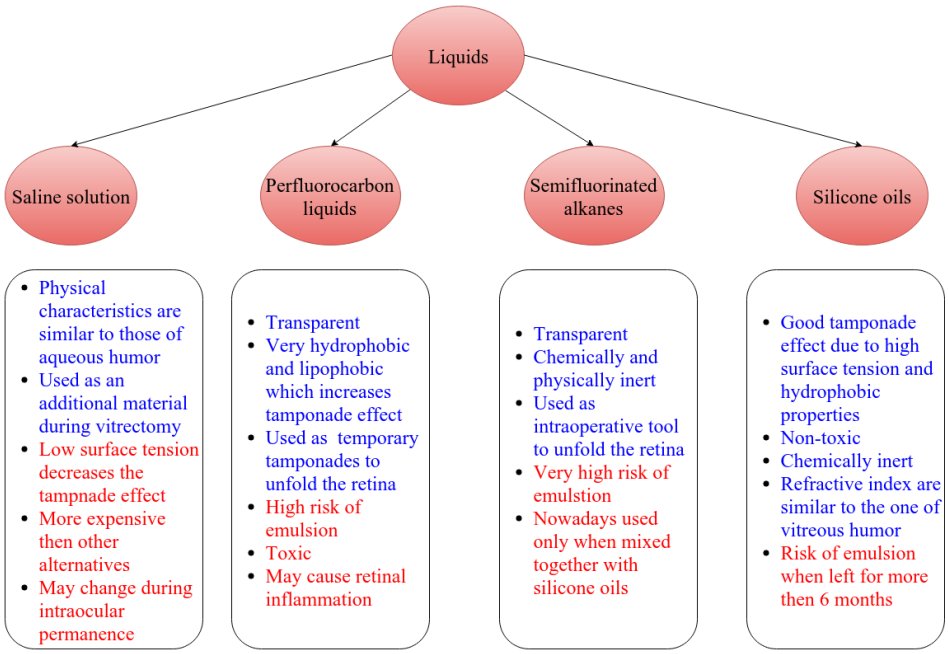

Figure 1.5.2: Most commonly used types of liquid tamponade fluids during vitrectomy. The advantages of each are listed in blue, and disadvantages in red. When the liquid tamponade is used the additional surgery is required in order to remove the substitute. Nowadays the most commonly used vitreous substitutes are silicone oils due to their low toxicity and high tamponade effect.

silicone oils are recommended as a long-term vitreous substitutes. In complicated cases, such as the presence of giant retinal tears, they might be the only recommended solution. Due to their hydrophobic properties and high surface tension silicone oils are considered as a good tamponades, with a tamponating effect that depends on the position of the bubble, i.e. patient's head position.

Complications related to the use of silicone oils are mainly cataract induction, corneal toxicity, glaucoma, and silicone retinopathy [24, 25]. Silicone oil droplets may disperse in the aqueous solution and these droplets that may travel to the anterior eye chamber. This process is called emulsification and is a common complication after the surgery with silicone oils. This causes many other complications and requires the removal of tamponade fluid.

Second generation silicone oils have similar properties to the silicone oils, but with much higher density. Usage of such fluids increases the risk of emulsion, however they have showed to have very high tamponating effect.

Combination of the silicone oils and fluorinated alkanes is called *heavy silicone oils*. As silicone oils, they are transparent and chemically inert. High density and viscosity lead to a good tamponating effect and reduction of emulsion tendency. They are also used as a long-term tamponades due to their stability. The removal of such fluids might be complicated by their high viscosity which cause their high adherence to the retina. Such "sticky oil phenomenon" causes inflammation and tissue reactivity [26].

Current clinical research for vitreous substitutes aims to reproduce some aspects of original vitreous. So far *polymer hydrogels* have shown suitable characteristics with great variability of chemical composition. However, experimental research is still advancing, since the ideal substitute must behave correctly in terms of biocompatibility and mechanical properties [13].

1.6 Aims of the thesis

There are many factors leading to the RD, such as aging, that is normally accompanied by vitreous liquefaction and posterior vitreous detachment, traumas or other pathological conditions. Whatever the mechanism that eventually leads to a RD mechanics is invariably heavily involved since ultimately what produces a retinal tear is a mechanical traction on the retina. The first aim of this thesis (see chapter 2) is to better understand the mechanics involved in the generation of retinal tears, which are the prerequisite to develop a rhegmatogeneous RD. In particular, we consider two cases that are typical when a patient experiencess the formation of a retinal break and are known risk factors for developing a RD. In section 2.2 we consider a pathological condition, known as vitreoschisis, which has been found in about half of the patients affected by retinal detachment [27]. Our purpose is to set up a simple mathematical model describing such a condition and aimed at understanding how the shear and normal stresses are distributed on the retina and how they are different from the normal condition, when no vitreoschisis is present.

In section 2.3 we model another possible risk factor of RD. In particular we model focal tractions on the retina that can be produced by a local hardening of the vitreous in a certain region. In fact, it is known that the mechanical properties of the vitreous body are variable in the vitreous chamber, and such variations can contribute to generate localised tractions on the retina during eye rotations. Adopting a simple mathematical model we study the effect of non-homogeneity of vitreous properties on the stress distribution on the retina.

In the second part of the thesis (chapter 3) we consider the case in which a tamponade

fluid is present in the vitreous chamber. Tamponade fluids used during vitrectomy usually are hydrophobic. After vitrectomy the tamponated retinal surface is strongly affected by shape of the interface between the aqueous humor and the tamponade fluid. In the thesis we aim at computing the shape of the interface, in order to obtain a better understanding of the efficiency of vitrectomy. In addition, we would like to study how the shape of the eye chamber might be the factor influencing the success of the surgery. The filling of the vitreous is never complete: the maximum filling of the vitreous chamber is around 90%. The hydrophobicity of the tamponade fluid results in the presence of the aqueous humor layer between the retina and the tamponade itself. Understanding how the stresses on the retina would change due to the presence of such a layer is one of the purposes of the thesis.

One of the possible complications related to the use of tamponade fluids, silicone oils in particular, is the formation of an emulsion, i.e. small droplets of oil in the aqueous solution. The mechanisms triggering the emulsification are poorely understood. It is believed, however, that shear instability at the aqueous humor-tamponade fluid interface might be responsible for the onset of emulsion. We would like verify the validity of this assumption from the purely mechanical point of view, by considering a simple mathematical model and study the stability of the interface between the aqueous humor and the vitreous substitute.

Chapter 2

Mathematical models of vitreoretinal tractions

Fluid motion in the vitreous chamber can be driven by different mechanisms, in particular, rotations of the eye ball or thermal differences between the anterior and posterior segments of the eye[1]. However, it can be shown by a simple order-of-magnitude argument that the fluid motion induced by eye rotations is much stronger then the thermally driven flow [28] and, therefore, we restrict our attention to the former.

Eye rotations induce motion in the fluid contained in the eye owing to the no-slip boundary condition, according to which the fluid in contact with a solid wall (e.g. the vitreous chamber wall) move at the same velocity as the wall itself. In other words, fluid particles do not flow across the wall and they do not slip over it.

In the section 2.1 we review results obtained by previous authors concerning the case of a rigid hollow sphere of radius R^*, modeling the vitreous chamber, filled with a fluid and study fluid motion generated by small-amplitude, periodic, torsional oscillations of the sphere. This problem has been studied in [1, 2] for the case of a viscoelastic fluid. In reality, the vitreous chamber is not perfectly spherical, particularly owing to the indentation produced in its anterior part by the lens. The effect of departure from the spherical shape on fluid motion has been studied theoretically and experimentally by several authors [29, 30, 31, 32, 33].

Fluid motion generates stresses on the wall, which were determined analytically. We discuss the qualitative characteristics of the flow and show the dependency of the stress at the wall on fluid viscosity. In addition to that we show how the results would change when a viscoelastic fluid is considered.

In section 2.2 we consider a pathological case of the eye, known as vitreoschisis, that might lead to retinal detachment and propose a mathematical model to describe it.

The natural vitreous humor is not homogeneous all over the domain. With aging it typically undergoes liquefaction, leading to the generation of liquid lacunae and regions of strong adherence with the retina that might be the site of high values of the elastic modulus. In section 2.3 we account for spatial variations of the mechanical properties of the vitreous (its elastic and viscous components). In order to treat the problem in a semi-analytical way we assume that the variations of vitreous properties are "small", in a sense that will be specified in the following. The model improves our understanding of the stresses distribution exerted on the retina during eye rotations. For simplicity we describe the domain as a sphere. However, we note that the method employed by Repetto et al. [31] to account for departure

of the geometry of the domain from the spherical one could be easily adopted also in this case. We feel, however, that this would unnecessary complicate the problem since the main aim of this work is to understand the effect of spatial variation of the vitreous mechanical properties on its dynamics.

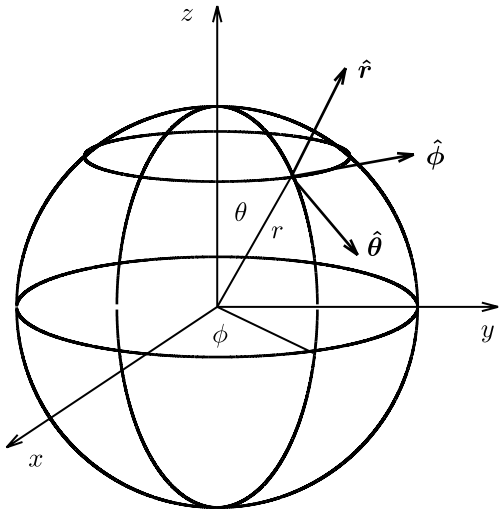

Figure 2.1.1: Spherical domain performing small amplitude torsional rotations filled with a viscoelastic fluid. The spherical system of coordinates is used for the model description.

2.1 Fluid motion in a periodically rotating sphere

2.1.1 Mathematical formulation

In this section we present a model already introduced by other authors [1, 2]. However, the model presented in this section serve as the basis to understand what follows in the rest of the chapter. Moreover, we discuss the results from a slightly different perspective with respect to what previous authors have done, focusing on the clinical application that motivates the work.

We consider a hollow rigid sphere with radius R^* performing periodic torsional oscillations of a small amplitude and frequency ω^* about an axis passing through its center (see figure 2.1.1). Here and later on the symbol $(*)$ refers to dimensional quantities. It is convenient for this analysis to adopt the spherical system of coordinates (r^*, θ, ϕ).

The velocity vector is composed of *radial* (u^*), *zenithal* (v^*) and *azimuthal* (w^*) components:

$$\mathbf{u}^* = [u^*, v^*, w^*]. \tag{2.1.1}$$

The angular displacement β of the sphere in time is described by the following time law:

$$\beta(t^*) = -A\cos(\omega^* t^*), \tag{2.1.2}$$

where A is the amplitude of oscillations and it is $A \ll 1$. This implies that the boundary condition at the wall is:

$$\mathbf{u}^* = A\omega^* R^* \sin(\theta)\sin(\omega^* t^*)\hat{\boldsymbol{\phi}} \quad \text{at} \quad (r^* = R^*), \tag{2.1.3}$$

where θ is the zenithal coordinate and $\hat{\boldsymbol{\phi}}$ is the unit vector in the azimuthal direction.

In order to make the problem dimensionless the following scaling has been used:

$$r^* = R^* r, \tag{2.1.4a}$$
$$\mathbf{u}^* = \omega^* R^* \mathbf{u}, \tag{2.1.4b}$$
$$p^* = \rho^* \omega^{*2} R^{*2} p, \tag{2.1.4c}$$
$$\tag{2.1.4d}$$

where ρ^* is the density of the fluid.

The fluid motion is governed by Navier-Stokes and continuity equations. The boundary conditions are no-slip boundary condition at the wall and regularity condition in the center of the sphere.

Taking advantage of the assumption of small amplitude eye rotations the system can be linearized, and it reduces to a single partial differential equation:

$$p = 0, \quad u = 0, \quad v = 0 \tag{2.1.5}$$

$$\frac{\partial w}{\partial t} = \frac{1}{\alpha^2}\Big[\frac{1}{r^2}\frac{\partial}{\partial r}\Big(r^2\frac{\partial w}{\partial r}\Big) + \frac{1}{r^2\sin\theta}\frac{\partial}{\partial\theta}\Big(\sin\theta\frac{\partial w}{\partial\theta}\Big) - \frac{w}{r^2\sin^2\theta}\Big] \tag{2.1.6a}$$
$$w = A\sin\theta\sin t \quad \text{at} \quad (r=1) \tag{2.1.6b}$$

where $\alpha = \sqrt{\rho^*\omega^* R^{*2}/\mu^*}$ is the Womersley number and μ^* is the dynamic viscosity of the fluid. In the case of a viscoelastic fluid the viscosity is given by a complex number, i.e. *complex viscosity* [34].

The equation (2.1.6) can be solved analytically by applying the separation of variables technique

$$w(r,\theta,t) = g(r)\sin\theta e^{it} + c.c. \tag{2.1.7}$$

where *c.c.* denotes the complex conjugate and $i = \sqrt{-1}$ is the imaginary unit.

The equation for $g(r)$ reads:

$$r^2 g'' + 2rg' + (k^2r^2 - 2)g = 0, \tag{2.1.8a}$$
$$g = -A\frac{i}{2} \quad \text{at} \quad (r=1), \tag{2.1.8b}$$

where prime ($'$) denotes the derivation with respect to the radial component r and $k = \alpha\sqrt{-i}$. The solution for $g(r)$ reads

$$g(r) = -A\frac{i}{2j_1(k)}j_1(kr) + c.c. \tag{2.1.9}$$

where j_1 is the modified Bessel function:

$$j_1(x) = \frac{\sin(x)}{x^2} - \frac{\cos(x)}{x}. \tag{2.1.10}$$

Hence the azimuthal velocity component equals to:

$$w(r,\theta,t) = -A\frac{i\big(\sin(kr) - kr\cos(kr)\big)}{2r^2\big(\sin(k) - k\cos(k)\big)}\sin(\theta)e^{it} + c.c. \tag{2.1.11}$$

The magnitude of the dimensionless wall shear stress τ (scaled with $A\rho^*\omega^{*2}R^{*2}$) is easily found and reads:

$$\tau = \big(w' - \frac{w}{r}\big)|_{r=1} = -\frac{1}{2}\Big(\frac{1}{1-k\cot k} - \frac{3}{k^2}\Big)\sin\theta e^{it} + c.c. \tag{2.1.12}$$

The maximum of τ is located on the equatorial plane $\theta = \pi/2$.

2.1.2 Results

From the clinical point of view it is of interest to understand the behavior of vitreous substitutes injected into the eye chamber during the vitrectomy. In particular, how their mechanical properties would change the stresses generated on the retina. Tamponade fluids are typically purely viscous fluids, where the visocsity varies over a wide range. The natural vitreous humor, however, is viscoelastic. The presence of elasticity influences the shear stress on the retina as it has been shown by Meskauskas et al [2]. We divide this subsection into two by studying separately viscous and viscoelastic fluids.

Viscous fluid

In figures 2.1.2 and 2.1.3 we plot vector field and velocity profiles attained for a two different viscous fluids on the equatorial plane orthogonal to the axis of the rotation. We note that this is the plane where the stress on the wall attains its maximum value. In figure 2.1.2 we show two velocity fields on the equatorial plane at the single time instant ($t = \pi/2$), which is the time of maximum wall velocity. In figure 2.1.3 we show the corresponding variation of the azimuthal velocity in the radial direction. Each curve in the plots corresponds to a different time within a period. The velocity is zero at the center of the domain ($r = 0$) and has the same velocity of the wall at $r = 1$. Both both cases flows the frequency is kept constant and equal to 20 rad/s, which is a realistic value for eye rotations. In figures 2.1.2(a) and 2.1.3(a) we use a viscosity typical of a silicone oil ($\mu^* = 1$ Pa·s), whereas figures 2.1.2(b) and 2.1.3(b) are obtained assuming the viscosity of water ($\mu^* = 0.001$ Pa·s). In the two cases the velocity profiles are significantly different. In the high viscosity case they are almost straight lines, in other words the fluid moves almost as if it was a rigid body. On the other hand, when the viscosity is small a thin layer forms at the wall in which the fluid moves and the velocity in the core of the domain is vanishingly small. This layer is referred to as an oscillatory boundary layer. The thickness of the oscillatory boundary layer at the wall is of order $\delta^* \sim \sqrt{\mu^*/(\rho^*\omega^*)}$. This means that similar results could have been obtained by keeping fixed the viscosity of the fluid and changing the frequency of oscillations. In fact, the problem is governed by a single dimensionless parameter α, the Womersley number, which can be physically interpreted as the ratio R^*/δ^* between the radius of the sphere and the thickness of the oscillatory boundary layer. Flows characterized by the same value of the Womersley number have identical velocity profiles. In purely viscous fluids, whatever the value of the viscosity, the maximum of the velocity is invariably attained at the wall ($r = 1$).

Since the shear stress depends linearly on the viscosity of the fluid and also on the spatial derivatives of the velocity profile, predicting if the stress will increase or decrease with the viscosity is not obvious. In fact, figures 2.1.3(a) and 2.1.3(b) show that as the viscosity decreases the derivative of the velocity at the wall increases. The dimensional magnitude of the wall shear stress is given by the following expression:

$$\tau^* = -\frac{\rho^* A}{2}(\omega^* R^*)^2 \Big(\frac{1}{1 - k\cot k} - \frac{3}{k^2} \Big) \sin\theta e^{i\omega^* t^*} + c.c. \tag{2.1.13}$$

The dynamic viscosity of the fluid μ^* is inversely proportional to the dimensionless parameter k as they are related as follows:

$$\mu^* = -\frac{i\rho^* R^{*2}}{k^2}, \tag{2.1.14}$$

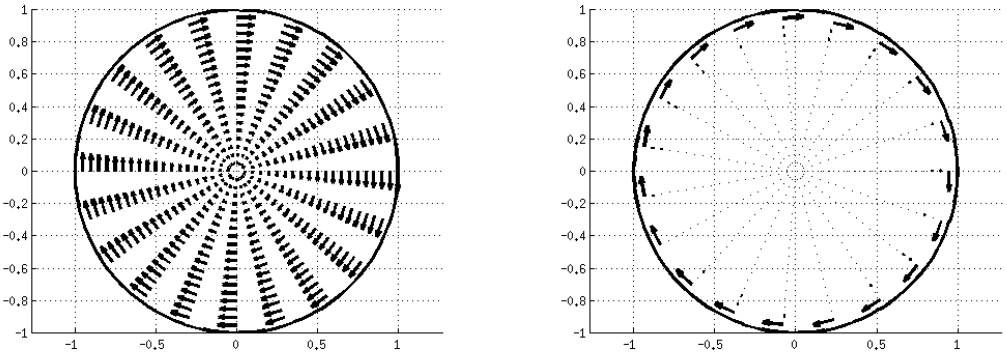

(a) (b)

Figure 2.1.2: Resulting velocity profile on the equatorial plane $\theta = \pi/2$ when the sphere undergoes oscillations of frequency $\omega = 20 \quad rad/s$ at the time instant $t = 0$. (a) Silicone oil, $\mu^* = 1 \quad Pa \cdot s$; (b) water, $\mu^* = 0.001 \quad Pa \cdot s$

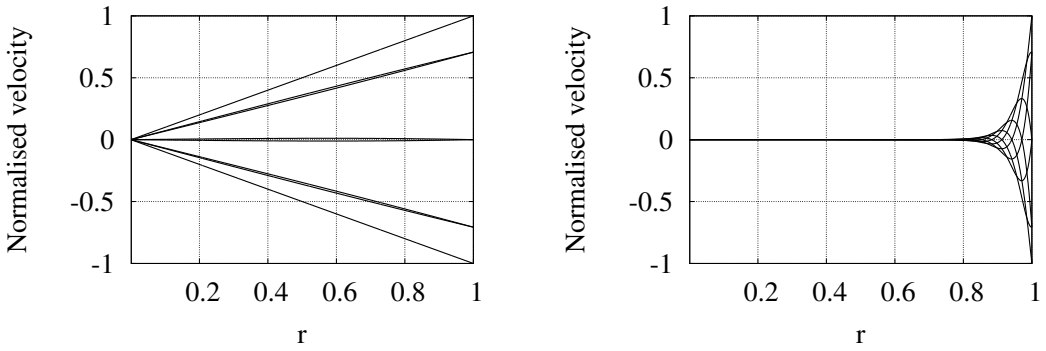

(a) (b)

Figure 2.1.3: Velocity profiles in the radial direction (scales with the maximum velocity). $r = 0$ corresponds to the center of the sphere and $r = 1$ to the location of the wall. The velocity is normalized with the maximum velocity at the wall. In both figures we assume that the sphere contains a purely viscous fluid and that the frequency of rotations is equal to 20 rad/s, which is typical of eye rotations. (a) Silicone oil, $\mu^* = 1 \quad Pa \cdot s$; (b) water, $\mu^* = 0.001 \quad Pa \cdot s$.

which implies that, in order to compute the limiting value of the maximum wall shear stress when viscosity grows to infinity, the limit of expression (2.1.13) when k tends to zero, has to be computed:

$$\tau^*_{max} = \lim_{\mu^* \to \infty} \tau^*(\theta = \pi/2) = \lim_{k \to 0} \tau^*(\theta = \pi/2) = \frac{A}{10}(\omega^* R^*)^2 \rho^* e^{i\omega^* t^*} + c.c., \tag{2.1.15}$$

which can be rewritten as

$$\tau^*_{max} = \frac{A}{5}(\omega^* R^*)^2 \rho^* \cos(\omega^* t^*). \tag{2.1.16}$$

In figure 2.1.4 we show how, in a viscous fluid, the maximum shear stress at the wall changes with the fluid viscosity. The results reported in figure 2.1.4 show that the maximum shear stress at the wall increases nonlinearly with the viscosity and attains an asymptotic value for very viscous fluids equals to $A\rho^*(\omega^* R^*)^2/5$ (equation 2.1.15). This implies that the adoption of highly viscous fluids as vitreous substitutes induces the generation of large mechanical stresses on the retina. In the figure 2.1.4 we report with vertical lines the cases corresponding to water and two often used silicone oils (0.96 and 4.8 $Pa \cdot s$) [13]. It appears that in the cases of the two oils the maximum wall shear stress on the retina is an order of magnitude higher then in the case of water. However, the differences between the two oils are small since, in the both cases, the value of the maximum stress on retina is almost equal to the maximum possible asymptotic value.

Viscoelastic fluid

The real healthy vitreous is a viscoelastic fluid [35, 36], i.e. a fluid in which the state of stress depends on the history of deformation. In other words, viscoelastic fluids have a memory. Figure 2.1.5 is obtained taking into account the viscoelasticity of the fluid. We have used the two-parameter model proposed by [2] in order to describe the viscoelastic behavior of the fluid. The velocity profiles show qualitative difference with respect to those obtained for purely viscous fluids. In particular, in the case of a viscoelastic fluid, the maximum velocity can be attained in the core of the domain and not at the wall. This phenomenon is due to a resonant excitation of vitreous motion. When resonance occurs, large values of the stress are attained on the boundary of the domain, i.e. on the retina.

In figure 2.1.4 we have reported points corresponding to viscoelastic case, adopting for the rheological properties of the vitreous the values measured in [35] and [36]. In these cases there is also an elastic component of the stress, the effect of which is to slightly increase the maximum wall shear stress with respect to purely viscous case.

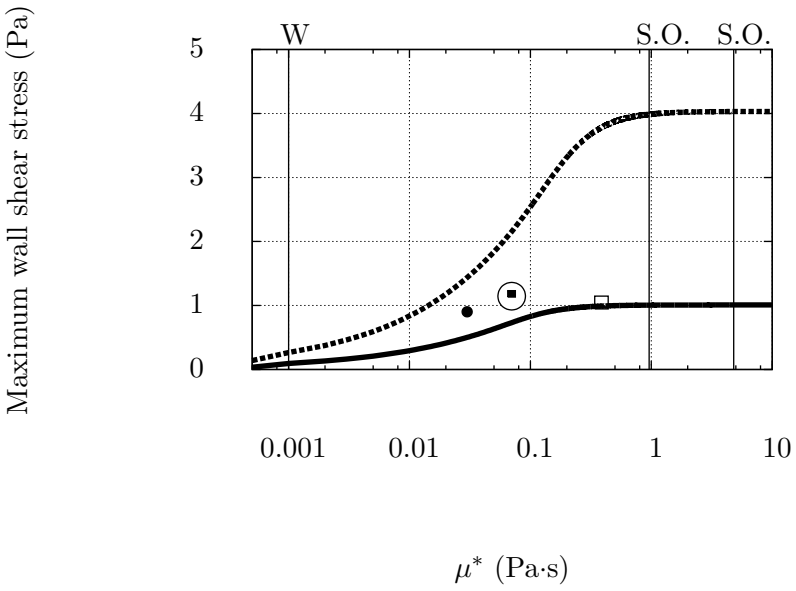

Figure 2.1.4: Dependency of the maximum shear stress at the wall on the viscosity in the case of purely viscous fluid. The two curves correspond to two different values of the frequency of eye rotations (dashed line 20 rad/s; solid line 10 rad/s; $A = 20$ deg $= \pi/9$rad). W: water; S.O.: silicone oils ($\rho^* = 960$ kg/m^3, $\mu^* = 0.96$ Pa·s, and $\mu = 4.8$ Pa·s.) In the figure we also report with symbols the values of maximum wall shear stress obtained in the case of a viscoelastic fluid and adopt the rheological properties measured in [35, 36]. Solid square: complex viscosity $\mu^* = 0.38 - i$ Pa·s, $\omega^* = 10$ rad/s [35]; empty square: $\mu^* = 0.07 - 0.28i$, $\omega^* = 10$ rad/s [35]; solid circle: $\mu^* = 0.07 - 0.28i$, $\omega^* = 12/57$ rad/s [36]; and empty circle: $\mu^* = 0.03 - 0.064i$, $\omega^* = 12.57$ rad/s [36].

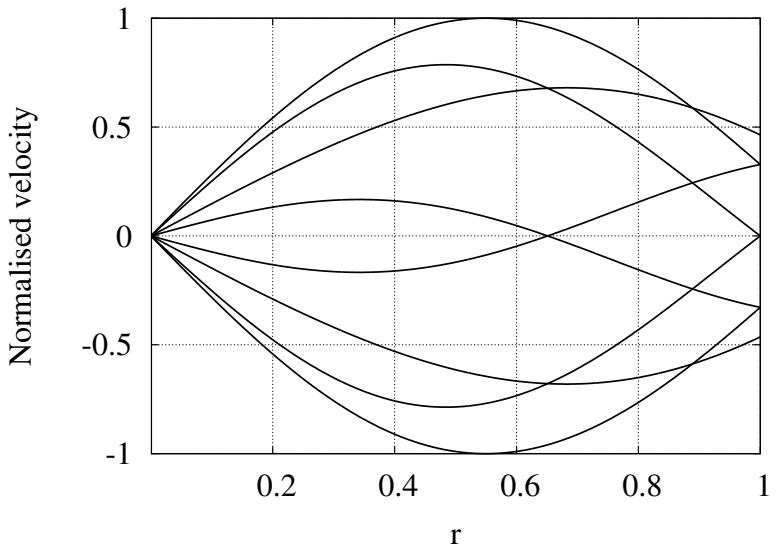

Figure 2.1.5: Azimuthal velocity profiles (scaled with the maximum velocity at the wall) using the initial values of [36]. The frequency of oscillations equals to $\omega^* = 21.61$ rad/s. The velocity is normalized by its maximum value. Each curve corresponds to a single time instant.

2.1.3 Discussion

In this section we have considered the case in which the whole vitreous chamber is filled with a single fluid and have modeled the chamber as a rigid sphere, performing sinusoidal small amplitude torsional oscillations, similarly to what was done by previous authors [1, 2]. We have shown that, when the fluid is purely viscous, the maximum velocity is invariably attained at the sphere wall and the velocity at the center of the domain is zero. In the limit of very large fluid viscosity the velocity profiles are approximately straight lines and the fluid moves almost as a rigid body. In the opposite limit of low viscosity, an oscillatory boundary layer forms at the wall and the fluid velocity in the core of the vitreous chamber is almost zero. We have shown that the maximum wall shear stress on the retina grows with increasing viscosity of the fluid in a highly nonlinear way and reaches an asymptotic value in the limit of high viscous fluid, which is easily predicted analytically. This is relevant for the choice of vitreous replacement fluids. In fact, the model shows that if the vitreous is replaced by a highly viscous fluid, mechanical actions of the retina should be expected to increase. This is,for instance, the case of silicone oils. In the clinical practice silicone oils with a viscosity of 10^{-3} m^2/s or $5 \cdot 10^{-3}$ m^2/s are typically adopted. We remark that in both cases the viscosity is so large that the maximum wall shear stress at the retina are close to its maximum possible values. This means that, in terms of mechanical stresses on the retina, the two oils are equivalent to each other. We will show in chapter 3 (section 3.2) that is a thin layer of aqueous separates the retina from the oil the wall shear stress can decrease dramatically.

We have also considered the flow characteristics in the case of a viscoelastic fluid filling the vitreous chamber. The real healthy vitreous has viscoelastic properties, and there is a large body of research devoted to the identification of vitreous replacement fluids with viscoelastic properties. We have recalled that the motion of a viscoelastic fluid can be resonantly excited by eye rotations and, if this happens, large values of the shear stress are expected to develop on the retina. This has important implications for the choice of ideal properties of vitreous substitutes. Soman and Banerjee [37] and Swindle and Ravi [38] review all materials currently in use, discuss their advantages and disadvantages, and list the characteristics of an ideal vitreous substitute. In their papers it is mentioned that the ideal substitute should have a large enough elastic component, so as to avoid excessive flow within the vitreous chamber. However, the possible occurrence of resonance as a risk factor for generating large mechanical stresses on the retina is disregarded. This was discussed in detail in [2, 39].

2.2 Vitreoschisis

The vitreous humor is a substance that consists mainly of water (≈98%), hyaluronan, collagen, and additional molecular components. In youth, the vitreous is tightly adherent to the retina. With advancing age, changes in vitreous macromolecular interactions result in the formation of liquefied vitreous that consists primarily of hyaluronan and water; in this case the collagen fibrils aggregate into bundles of parallel fibers [40]. Moreover, with aging the vitreous cortex gets thinner, leading to the formation of small pockets of liquefied vitreous humor. These pockets slowly move through the thin cortex layer and settle between the cortex and the retina. These two processes, vitreous liquefaction and cortex thinning, normally occur simultaneously and result, in the majority of cases, in posterior vitreous detachment (PVD) [27]. The effect of PVD may vary from negligible to significant, depending on the conditions of the vitreoretinal interface [41].

The variety of manifestations of anomalous PVD depends on where the vitreous gel is liquefied and where the vitreo-retinal adhesion is strong. In the peripheral fundus, advanced gel liquefaction in the presence of strong vitreo-retinal adhesion causes retinal tears and detachments [27]. At the macula, the damage of PVD depends on the vitreous cortex condition. It might be either intact (full thickness) or split (partial thickness). Full-thickness vitreous cortex adherence to the macula in presence of peripheral vitreo-retinal separation leads to vitreo-macular traction.

A split in the posterior vitreous cortex, known as vitreoschisis, may result in different pathologies, including macular holes, macula pucker and retinal detachment. Vitreoschisis is a consequence of anomalous PVD. It occurs when the vitreo-macular adhesion is very strong, such that the collapse of the vitreous humor owing to its liquefaction leads to the splitting in vitreous cortex, leaving the outermost layer attached to the macula while the reminder of the vitreous collapses forward.

Recently, combined optical coherence tomography/scanning laser ophthalmoscopy (OCT/SLO) was able to identify vitreoschisis clinically (figure 2.2.1). Studies have shown that vitreoschisis has been detected in 53% patients with macular holes and 43% with macula pucker [27]. This suggested that a split in the vitreous cortex causes tangential traction upon the underlying retina and results in macular pucker or macular holes if the vitreous is also attached to the optic disc, inducing outward (centrifugal) tangential contraction. In fact, it is believed that the point where the two layers re-join into one full-thickness layer is often site of significant tractions upon the retina [27].

In this section we study how the stresses exerted on the retina are spatially distributed in the presence of vitreoschisis. Based on clinical studies of vitreoschisis [27, 40, 41], we know that the split in the vitreous is very thin with respect to the size of the domain. We assume that its effect on the motion of the vitreous is related to the fact that particles on the two sides of the split do not necessarily move at the same velocity. Specifically, the outer side of the split has a velocity which is dictated by the motion of the eye, while the inner side of the split presumably moves at a slightly smaller velocity during eye rotations. We, therefore, model the presence of the split by modifying the boundary condition at the wall that the fluid within the vitreous cavity has to satisfy. More precisely, we model the vitreoschisis as a region in which the no-slip condition is partially relaxed. In order to face the problem analytically we assume that the relative velocity between the fluid and the wall in the region of the vitreoschisis is small compared to the wall velocity and adopt a perturbation approach.

Based on the same assumptions, we set up two different models, two- and three-dimensional,

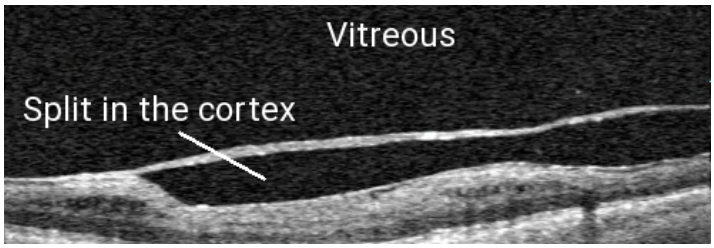

Figure 2.2.1: Clinical vitreoschisis. The outer layer of the split posterior vitreous cortex remains adherent to the retina.

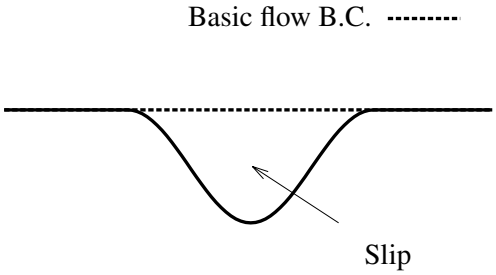

Figure 2.2.2: Boundary condition at the wall $y^* = 0$. The dashed line represents the case without vitreoschisis, i.e. it is the basic flow boundary condition. The solid line corresponds to the presence of vitreoschisis. We model a split in the vitreous cortex by relaxing the boundary condition of the basic flow.

respectively. In the case of the two-dimensional model we consider a semi-infinite domain and model the retinal surface as a flat wall, which performs oscillations (the eye movements) along its plane. The advantage of this model is that a solution can be found in closed form, which makes it easy to understand and discuss the results. A three-dimensional model, however, gives a more realistic view on the problem. In this case we consider a spherical domain. The spatially variable slip-condition is expanded in vector spherical harmonics.

2.2.1 Mathematical formulation. Two-dimensional model

Vitreoschisis is a small split in the vitreous cortex. The thickness of the split is much smaller with respect to the radius of the eye. Owing to this fact we start our analysis with a simple two-dimensional mathematical model.

The eye wall is modeled as a flat wall, placed at $y^* = 0$, that performs small-amplitude ($A^* \ll 1$, where A^* is the dimensional amplitude) harmonic oscillations along the x^*-direction. These oscillations represent eye movements. The fluid (vitreous humor) occupies the semi-plane $y^* \geq 0$. Even though the real saccadic eye rotations are not exactly harmonic in time, this time dependency of the velocity provides a good approximation of the real situation. Thus, the velocity of the wall in the x^*-direction is given by the following expression:

$$U^*_{wall} = A^* \sin(\omega^* t^*), \tag{2.2.1}$$

where ω^* is the frequency of oscillations.

Under normal conditions, when no vitreoschisis is present, the fluid adherent to the wall moves with the same velocity as the wall itself, i.e. the no-slip boundary condition holds. The fluid, however, may experience a slip at the wall when the vitreoschisis is present. This suggests us to relax the boundary condition (2.2.1) by adding a spatial variation of the velocity (see figure 2.2.2). Taking advantage of the infinite size of the domain in the x^*-direction, we can use a Fourier expansion in this direction. In the general case the boundary condition at the wall in the case of vitreoschisis can be written as

$$\overline{U}^*_{wall} = U^*_{wall} + \varepsilon u^*_{wall} \qquad (y^* = 0), \tag{2.2.2}$$

where $\overline{U}^*_{wall}$ is the fluid velocity at the wall, U^*_{wall} is the wall velocity (basic state, equation (2.2.1)) and εu^*_{wall} is the small ($\varepsilon \ll 1$) perturbation of the boundary condition that describes the split in the vitreous cortex.

Following equation (2.2.2) we now can split our variables into basic flow and perturbation terms

$$\overline{\mathbf{u}}^* = \mathbf{U}^* + \varepsilon \hat{\mathbf{u}}^*, \tag{2.2.3a}$$

$$\overline{P}^* = P^* + \varepsilon \hat{p}^*, \tag{2.2.3b}$$

$$\overline{\tau}^* = T^* + \varepsilon \hat{\tau}^*. \tag{2.2.3c}$$

Capital letters refer to the basic solution and small ones refer to the perturbations; $\overline{P}^*$ is the total pressure field and $\overline{T}^*$ is the total wall shear stress.

In order to make the problem dimensionless the following scaling is applied to all the variables involved in the system:

$$\overline{\mathbf{u}}^* = L^* \omega^* \overline{\mathbf{u}}, \quad t^* = \frac{1}{\omega^*} t, \quad (x^*, y^*) = L^*(x, y), \tag{2.2.4}$$

where L^* is the length of the split.

Owing to the small-amplitude of the oscillations ($A^* \ll 1$) the system is governed by the linearized Navier-Stokes and continuity equations. The dimensionless parameter involved in the governing system is the (complex) Womersley number, which is defined as

$$\alpha = \sqrt{\frac{\omega^* L^{*2}}{\nu^*}} \tag{2.2.5}$$

where ν^* is the fluid viscosity which might be complex when elasticity is taken into account. We denote by η the loss factor which is equal to the ratio between the imaginary and real part of the viscosity $\eta = \nu^*_{\mathcal{I}}/\nu^*_{\mathcal{R}}$. Then the complex Womersley number can be written as follows:

$$\alpha = \sqrt{\frac{\omega^* L^{*2}}{\nu^*_{\mathcal{R}}}} \sqrt{\frac{1}{1 + i\eta}} = \alpha_r \sqrt{\frac{1}{1 + i\eta}}, \tag{2.2.6}$$

where α_r is the real Womersley number, i.e. the Womersley number corresponding to the case when purely viscous fluid is considered.

In general case, if by $\mathbf{n}$ we denote the normal to the solid surface directed into the fluid, and by $\mathbf{t}$ - the tangential to the solid surfcae then the boundary condition proposed by Navier [42], can be written as

$$\overline{\mathbf{u}} \cdot \mathbf{n} = 0, \quad \overline{\mathbf{u}} = (A \sin t)\mathbf{t} + 2\varepsilon f(x)\{\mathbf{E} \cdot \mathbf{n} - [(\mathbf{E} \cdot \mathbf{n}) \cdot \mathbf{n}]\mathbf{n}\} \quad \text{at } y = 0, \tag{2.2.7}$$

where $\mathbf{E} = \frac{1}{2}(\nabla\mathbf{U} + \nabla\mathbf{U}^T)$ is the rate of strain tensor, which is equal to

$$\mathbf{E} = \begin{bmatrix} 0 & \frac{1}{2}\frac{\partial U}{\partial y} \\ \frac{1}{2}\frac{\partial U}{\partial y} & 0 \end{bmatrix} \tag{2.2.8}$$

The function $f(x)$ is known as the slip length. In the case when $f(x) = 0$ the classical no-slip boundary condition is recovered.

Basic flow

The dimensionless boundary condition at the wall ($y = 0$) for the basic flow is given by

$$U_{wall} = A\sin t = -A\frac{i}{2}e^{it} + c.c., \tag{2.2.9}$$

where $A = A^*/(L^*\omega^*)$.

The fact that the wall moves only in the horizontal direction suggests the following form of the solution for the basic flow

$$\mathbf{U} = [U(y,t), 0]. \tag{2.2.10}$$

Neglecting the effect of gravity the pressure is constant and can be set equal to zero without loss of generality. The Navier-Stokes equation in the x-direction reads:

$$\frac{\partial U}{\partial t} = \frac{1}{\alpha^2}\frac{\partial^2 U}{\partial y^2}, \tag{2.2.11}$$

which can be easily solved by separation of variables and applying the boundary condition (2.2.9) at the wall and zero velocity at infinity. The final solution of the basic flow reads:

$$U(y,t) = Ae^{-\sqrt{\frac{\alpha^2}{2}}y}\sin\left(t - \sqrt{\frac{\alpha^2}{2}}y\right). \tag{2.2.12}$$

The dimensionless shear stress at the wall T, scaled with $A\rho^*L^{*2}\omega^{*2}$, corresponding to this solution is given by:

$$T = \frac{1}{\alpha^2}\frac{\partial U}{\partial y}\bigg|_{y=0} = \frac{1}{2}\sqrt{\frac{-i}{\alpha^2}}e^{it} + c.c. \tag{2.2.13}$$

Solution for the perturbation

As in the case of the basic flow the system is governed by the linearized Navier-Stokes and continuity equations:

$$\frac{\partial \hat{u}}{\partial t} = -\frac{\partial \hat{p}}{\partial x} + \frac{1}{\alpha^2}\Big[\frac{\partial^2 \hat{u}}{\partial x^2} + \frac{\partial^2 \hat{u}}{\partial y^2}\Big], \tag{2.2.14a}$$

$$\frac{\partial \hat{v}}{\partial t} = -\frac{\partial \hat{p}}{\partial y} + \frac{1}{\alpha^2}\Big[\frac{\partial^2 \hat{v}}{\partial x^2} + \frac{\partial^2 \hat{v}}{\partial y^2}\Big], \tag{2.2.14b}$$

$$\frac{\partial \hat{u}}{\partial x} + \frac{\partial \hat{v}}{\partial y} = 0. \tag{2.2.14c}$$

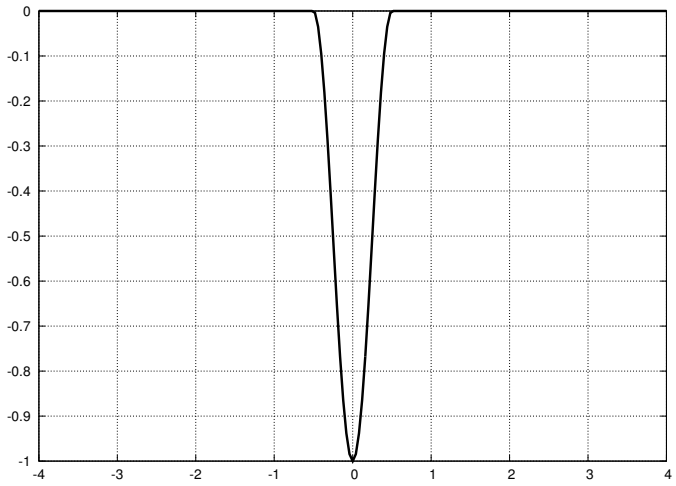

Figure 2.2.3: Slip length described by the function $f(x)$ given by equation (2.2.16)

The the boundary condition for the perturbation at infinity is zero and at the wall is given by

$$u_{wall} = f(x)\frac{\partial U}{\partial y}\bigg|_{y=0} = \frac{ipA}{2}f(x)e^{it} + c.c, \tag{2.2.15}$$

where $p = \alpha\sqrt{i}$. The function $f(x)$ models the presence of the split in the vitreous cortex. It is so called slip length (see [42, 43]).Let the function $f(x)$ be a periodic function defined on the interval $x \in [-\infty, \infty]$ and with a period of $2m$. The region of the split is at the interval $[-\frac{1}{2}, \frac{1}{2}]$ so that its length is one. The value of the parameter m is chosen such that the results far away from split are not influenced by its presence. The function $f(x)$ is zero everywhere except from the part with a split. We define this function as follows:

$$f(x) = \begin{cases} \frac{1}{2} + \frac{1}{2}\cos(2\pi x), & x \in [-\frac{1}{2}, \frac{1}{2}], \\ 0, & x \in [-m, -\frac{1}{2}] \cup [\frac{1}{2}, m]. \end{cases} \tag{2.2.16}$$

(see figure 2.2.3). Taking advantage of the infinity of the domain in the x-direction the function $f(x)$ can be expanded in the Fourier series. We thus write

$$f(x) = \frac{a_0}{2} + a_{2m}\cos(2\pi x) + \sum_{\substack{n=1 \\ n\neq 2m}}^{\infty} a_n \cos\left(\frac{n}{m}\pi x\right), \tag{2.2.17}$$

and the coefficients in the above expansion take the following values:

$$a_0 = -\frac{1}{2m}, \tag{2.2.18a}$$

$$a_{2m} = -\frac{1}{4m}, \tag{2.2.18b}$$

$$a_n = -\frac{\sin\left(\frac{n}{m}\frac{\pi}{2}\right)}{n\pi} - \frac{1}{2\pi n}\left[\frac{\sin\left((2+\frac{n}{m})\frac{\pi}{2}\right)}{2+\frac{n}{m}} + \frac{\sin\left((2-\frac{n}{m})\frac{\pi}{2}\right)}{2-\frac{n}{m}}\right]. \tag{2.2.18c}$$

This implies that the components of the velocity vector $\hat{\mathbf{u}} = [\hat{u}, \hat{v}]$, the pressure $\hat{p}$ and the wall shear stress $\hat{\tau}$ can be expanded as follows:

$$\hat{u}(x,y,t) = \sum_{n=0}^{\infty} u_n(y)\cos(n\pi x/m)e^{it} + c.c., \tag{2.2.19a}$$

$$\hat{v}(x,y,t) = \sum_{n=0}^{\infty} v_n(y)\sin(n\pi x/m)e^{it} + c.c., \tag{2.2.19b}$$

$$\hat{p}(x,y,t) = \sum_{n=0}^{\infty} p_n(y)\sin(n\pi x/m)e^{it} + c.c., \tag{2.2.19c}$$

$$\hat{\tau}(x,t) = \sum_{n=0}^{\infty} \tau_n\cos(n\pi x/m)e^{it} + c.c. \tag{2.2.19d}$$

Using this approach the solution is decomposed as a sum of Fourier harmonics. Substituting the above expansion (2.2.19) into the governing system of equations (2.2.14) we get

$$iu_n = np_n + \frac{1}{\alpha^2}\Big[-n^2u_n + u_n''\Big], \tag{2.2.20a}$$

$$iv_n = -p_n' + \frac{1}{\alpha^2}\Big[-n^2v_n + v_n''\Big], \tag{2.2.20b}$$

$$-nu_n + v_n' = 0, \tag{2.2.20c}$$

for $n = 1, \ldots, \infty$. Note that the harmonic $n = 0$ represents a correction to the basic flow as the corresponding solution does not depend on x.

The boundary conditions are then given by:

$$u_n = -A\frac{i}{2}a_n \qquad (y = 0), \tag{2.2.21a}$$

$$v_n = 0 \qquad (y = 0), \tag{2.2.21b}$$

$$u_n = 0 \qquad (y \to \infty), \tag{2.2.21c}$$

$$v_n = 0 \qquad (y \to \infty). \tag{2.2.21d}$$

In order to solve the above system (2.2.20) we substitute $u_n = v_n'/n$, obtained from the continuity equation (2.2.20c), into the Navier-Stokes equations, eliminate the pressure by deriving equation (2.2.20a) with respect to y and subtracting it from the equation (2.2.20a).

The system then reduces to the following a fourth-order ODE:

$$v_n'''' + av_n'' + bv_n = 0, \tag{2.2.22}$$

with

$$a = -2\Big(\frac{n\pi}{m}\Big)^2 - i\alpha^2, \tag{2.2.23a}$$

$$b = \Big(\frac{n\pi}{m}\Big)^4 + i\Big(\frac{n\pi}{m}\Big)^2\alpha^2, \tag{2.2.23b}$$

and subjected to the following four boundary conditions:

$$v_n = 0 \qquad (y = 0), \tag{2.2.24a}$$
$$v_n' = -A\frac{in}{2}a_n \qquad (y = 0), \tag{2.2.24b}$$
$$v_n = 0 \qquad (y \to \infty), \tag{2.2.24c}$$
$$v_n' = 0 \qquad (y \to \infty). \tag{2.2.24d}$$

The solution for u_n and v_n is then easily computed and reads:

$$u_n = A\frac{c_1 p_1 e^{p_1 y} + c_2 p_2 e^{p_2 y}}{n}, \tag{2.2.25a}$$
$$v_n = A\left(c_1 e^{p_1 y} + c_2 e^{p_2 y}\right), \tag{2.2.25b}$$

where p_1 and p_2 are given by

$$p_1 = -\sqrt{\frac{-a - \sqrt{a^2 - 4b}}{2}}, \tag{2.2.26a}$$
$$p_2 = -\sqrt{\frac{-a + \sqrt{a^2 - 4b}}{2}}, \tag{2.2.26b}$$

and the constants c_1 and c_2 are found applying the boundary conditions and read

$$c_1 = -\frac{in}{2(p_1 - p_2)}, \tag{2.2.27a}$$
$$c_2 = -c_1. \tag{2.2.27b}$$

Summing up all the terms of the expansion (2.2.19) the final solution for the perturbation is found.

The constants for the dimensionless perturbation to the wall shear stress, τ_n (again scaled with $A\rho^* L^{*2}\omega^{*2}$), are given by the expression

$$\tau_n = \frac{c_1 p_1^2 + c_2 p_2^2}{n\alpha^2}. \tag{2.2.28}$$

In the next section we present a three-dimensional version of the model and discuss all results in section 2.2.3.

2.2.2 Mathematical modeling of vitreoschisis in a spherical domain

Basic flow

We now describe a problem analogous to that described in the previous section but model the domain as a sphere, which is obviously more realistic than the flat case. This will give us a better understanding on how the stresses are distributed on the retina in the presence of vitreoschisis.

We model the vitreous chamber as a sphere of a radius R^*, which performs small-amplitude periodic torsional rotations about an axis passing through its center with a frequency ω^*. The

angular displacement $\beta(t^*)$ of the sphere in time is described by equation (2.1.2), and again we assume $A \ll 1$, with A denoting the amplitude of rotations.

It is convenient to adopt a spherical system of coordinates (r^*, θ, ϕ) (see figure 2.1.1 of section 2.1). The velocity vector $\overline{\mathbf{u}}^* = [\overline{u}^*, \overline{v}^*, \overline{w}^*]$, where $\overline{u}^*$, $\overline{v}^*$ and $\overline{w}^*$ denote the radial, zenithal and azimuthal components.

We scale the problem as follows, using the radius of the sphere as length scale:

$$r^* = R^* \cdot r, \tag{2.2.29a}$$
$$\overline{\mathbf{u}}^* = \omega^* R^* \cdot \overline{\mathbf{u}}, \tag{2.2.29b}$$
$$(\overline{p}^*, \overline{\tau}^*) = \rho^* \omega^{*2} R^{*2} \cdot (\overline{p}, \overline{\tau}), \tag{2.2.29c}$$

where ρ^* is the density of the fluid filling the domain, $\overline{p}^*$ is the dimensional pressure and $\overline{\tau}^*$ is the dimensional wall shear stress. Similarly to what we did in the previous section we decompose the variables into a basic flow (the motion is a rotating sphere) and a perturbation (induced by the relaxation of the no-slip condition in certain regions of the sphere surface). Thus we write

$$\overline{\mathbf{u}} = \mathbf{U} + \varepsilon \hat{\mathbf{u}}, \tag{2.2.30a}$$
$$\overline{p} = P + \varepsilon \hat{p}, \tag{2.2.30b}$$
$$\overline{\tau} = T + \varepsilon \hat{\tau}, \tag{2.2.30c}$$

where $\varepsilon \ll 1$.

The system is governed by the Navier-Stokes equations which can be linearized due to small-amplitude of the oscillations. The boundary condition at the wall $r = 1$ for the basic flow according to the angular displacement $\beta^*(t)$ equals to

$$\mathbf{U} = [0, 0, A \sin t \sin \theta] \quad (r = 1). \tag{2.2.31}$$

The second boundary condition is the regularity at the origin

$$|\mathbf{U}| \text{ is bounded} \quad (r = 0). \tag{2.2.32}$$

The solution of the basic flow is that described in section 2.1 and we recall it here for convenience

$$U = 0, \quad , V = 0, \quad P = 0, \tag{2.2.33a}$$
$$W(r, \theta, t) = -A \frac{i\big(\sin(kr) - kr\cos(kr)\big)}{2r^2\big(\sin(k) - k\cos(k)\big)} \sin(\theta) \tag{2.2.33b}$$

where $k = \alpha\sqrt{-i}$ and $\alpha = R^*\sqrt{\rho^*\omega^*/\mu^*}$ is the Wormersley number.

The dimensionless wall shear stress corresponding to the basic flow, scaled with $A\rho^*\omega^{*2}R^{*2}$, is given by the following expression

$$T = -\frac{1}{2}\Big(\frac{1}{1 - k\cot k} - \frac{3}{k^2}\Big)\sin\theta \tag{2.2.34}$$

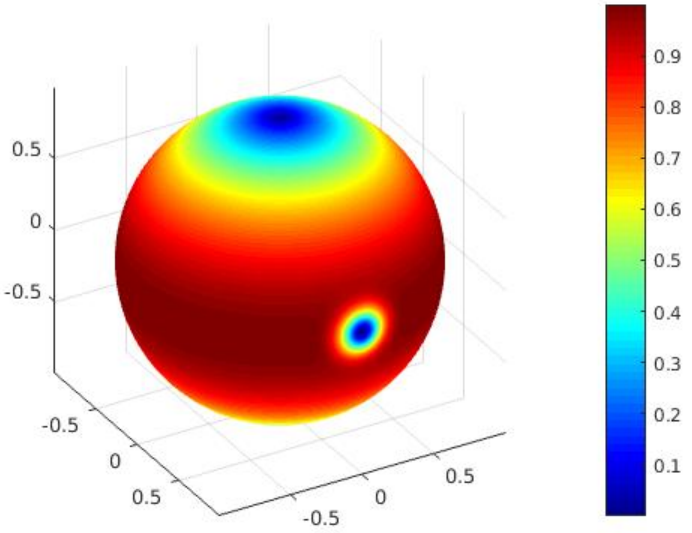

Figure 2.2.4: Normalized veloctiy imposed at the wall at time $t = \pi/2$. The blue spot on the equatorial plane is where the no-slip condition is relaxed.

Solution for the perturbation

The perturbation is induced by a "small" relaxation of the no-slip condition in a certain region of the surface of the sphere. We thus write

$$\mathbf{u}_w = [u_w, v_w, w_w] = \left[0, 0, \left(W' - \frac{1}{r}W\right)\Big|_{r=1} f(\theta, \phi)\right]. \tag{2.2.35}$$

For the function describing the slip length $f(\theta, \phi)$ we choose the following form

$$f(\theta,\phi) = \begin{cases} \frac{1}{4}\cdot[1+\cos(k_1\phi)]\cdot[(1+\cos(k_2\theta))] & \text{if } \phi \in [-\frac{\pi}{n}, \frac{\pi}{n}], \\ & \theta \in [\frac{\pi}{2} - \frac{\pi}{n}, \frac{\pi}{2} + \frac{\pi}{n}], \\ 0 & \text{otherwise.} \end{cases} \tag{2.2.36}$$

The azimuthal component of the velocity at the boundary is plotted in figure 2.2.4. It shows that we are modeling a localized relaxation of the no-slip condition centered on the equatorial plane. In the figure the axis of rotation is vertical. In equation (2.2.36) the parameters k_1 and k_2 define the size of the vitreoschisis and $\varepsilon \ll 1$.

In order to solve the problem for the perturbation we expand the vector (2.2.35) in terms of spherical harmonics. The scalar spherical harmonics of degree n and order m, for $n \geq 0$ and $-n \leq m \leq n$ are defined as

$$Y_{mn}(\theta,\phi) = (-1)^m \sqrt{\frac{2n+1}{4\pi}\frac{(n-m)!}{(n+m)!}} P_{mn}(\cos(\theta)) e^{im\phi}, \tag{2.2.37}$$

where

$$P_{mn}(x) = \begin{cases} (1-x^2)^{m/2}\left(\frac{d}{dx}\right)^m P_n(x) & \text{for} \quad m \geq 0, \\ (-1)^{|m|}\frac{(n-|m|)!}{(n+|m|)!}P_{|m|n}(x) & \text{for} \quad m < 0, \end{cases} \tag{2.2.38}$$

and P_n is the Legendre polynomial of order n. The vector spherical harmonics of degree n and order m, $\mathbb{P}_{mn}(\theta,\phi)$, $\mathbb{B}_{mn}(\theta,\phi)$ and $\mathbb{C}_{mn}(\theta,\phi)$, are defined for $n \geq 0$ and $-n \leq m \leq n$ as

$$\mathbb{P}_{mn} = Y_{mn}\hat{\mathbf{r}} = \begin{pmatrix} Y_{mn} \\ 0 \\ 0 \end{pmatrix}, \tag{2.2.39a}$$

$$\mathbb{B}_{mn} = \frac{r}{s_n}\nabla Y_{mn} = \frac{1}{s_n}\begin{pmatrix} 0 \\ \frac{\partial Y_{mn}}{\partial \theta} \\ \frac{1}{\sin\theta}\frac{\partial Y_{mn}}{\partial \phi} \end{pmatrix}, \tag{2.2.39b}$$

$$\mathbb{C}_{mn} = \frac{1}{s_n}\nabla \times (Y_{mn}\mathbf{r}) = \frac{1}{s_n}\begin{pmatrix} 0 \\ \frac{1}{\sin\theta}\frac{\partial Y_{mn}}{\partial \phi} \\ -\frac{\partial Y_{mn}}{\partial \theta} \end{pmatrix}, \tag{2.2.39c}$$

where $\mathbf{r}$ represents the position vector, $\hat{\mathbf{r}}$ the unit vector in the same direction and $s_n = \sqrt{n(n+1)}$. For $n = m = 0$, $\mathbb{B}_{00} = 0$ and $\mathbb{C}_{00} = 0$.

We thus expand the vector defining the boundary condition at $r = 1$ as follows:

$$\mathbf{u}_w = \sum_{n=0}^{\infty}\sum_{m=-n}^{n}\left[f_1^{mn}\mathbb{P}_{mn}(\theta,\phi) + f_2^{mn}\mathbb{B}_{mn}(\theta,\phi) + f_3^{mn}\mathbb{C}_{mn}(\theta,\phi)\right], \tag{2.2.40}$$

with f_1^{mn} equal to zero due to (2.2.35).

The velocity vector and pressure term are also expanded in terms of spherical harmonics in the following way:

$$\mathbf{u} = \sum_{n=0}^{\infty}\sum_{m=-n}^{n}\Big[U_{mn}(r)\mathbb{P}_{mn}(\theta,\phi) + V_{mn}(r)\mathbb{B}_{mn}(\theta,\phi) + W_{mn}(r)\mathbb{C}_{mn}(\theta,\phi)\Big]e^{it} + c.c., \tag{2.2.41a}$$

$$p = \sum_{n=0}^{\infty}\sum_{m=-n}^{n} P_{mn}(r)Y_{mn}(\theta,\phi)e^{it} + c.c. \tag{2.2.41b}$$

Substituting these expansions into the linearized Navier-Stokes equations the governing system of equations for each n and m reads

$$iU_{mn} = -\frac{d}{dr}P_{mn} + \frac{1}{\alpha^2}\Big(\Big(D_n - \frac{2}{r^2}\Big)U_{mn} + \frac{2s_n}{r^2}V_{mn}\Big), \tag{2.2.42a}$$

$$iV_{mn} = -\frac{s_n}{r}P_{mn} + \frac{1}{\alpha^2}\Big(\frac{2s_n}{r^2}U_{mn} + D_nV_{mn}\Big), \tag{2.2.42b}$$

$$iW_{mn} = \frac{1}{\alpha^2}D_nW_{mn}, \tag{2.2.42c}$$

where D_n is defined as

$$D_n = \frac{d^2}{dr^2} + \frac{2}{r}\frac{d}{dr} - \frac{s_n^2}{r^2}. \tag{2.2.42d}$$

The continuity equation is given by

$$\left(\frac{2}{r} + \frac{d}{dr}\right)U_{mn} - \frac{s_n}{r}V_{mn} = 0. \tag{2.2.43}$$

Finally, the boundary conditions read

$$U_{mn} = 0 \qquad (r = 1), \tag{2.2.44a}$$
$$V_{mn} = f_2^{mn} \qquad (r = 1), \tag{2.2.44b}$$
$$W_{mn} = f_3^{mn} \qquad (r = 1), \tag{2.2.44c}$$
$$U_{mn}, V_{mn}, W_{mn} \text{ are bounded} \qquad (r = 0). \tag{2.2.44d}$$

The above system can be solved analytically and the solution reads

$$U_{mn} = c_1 r^{n-1} + c_2 \frac{J_{n+1/2}(ar)}{r^{3/2}}, \tag{2.2.45a}$$
$$V_{mn} = c_1 s_n \frac{r^{n-1}}{n} + c_2 \frac{arJ_{n-1/2}(ar) - nJ_{n+1/2}(ar)}{s_n r^{3/2}}, \tag{2.2.45b}$$
$$W_{mn} = c_3 \frac{J_{n+1/2}(ar)}{r^{1/2}}, \tag{2.2.45c}$$
$$P_{mn} = c_1 \frac{a^2}{n}, \tag{2.2.45d}$$

where $a = \alpha\sqrt{-i}$, J_i are the Bessel function of first kind of order i and the constants are found by applying the boundary conditions and read:

$$c_1 = -\frac{s_n J_{n+1/2}(a) f_2^{mn}}{aJ_{n-1/2}(a) - (2n+1)J_{n+1/2}(a)}, \tag{2.2.46a}$$
$$c_2 = \frac{s_n f_2^{mn}}{aJ_{n-1/2}(a) - (2n+1)J_{n+1/2}(a)}, \tag{2.2.46b}$$
$$c_3 = \frac{f_3^{mn}}{J_{n+1/2}(a)}. \tag{2.2.46c}$$

2.2.3 Results

Two-dimensional model

The main aim of this analysis is to investigate how the stress on the retina changes in the presence of vitreoschisis. In this section we present the results obtained with the two-dimensional model described in section 2.2.1. We consider a viscoelastic fluid which is the case of real natural vitreous humor.

Figure 2.2.5 shows a snapshot of the perturbation flow field taken at $t = \pi/2$ that is the time at which the velocity is maximum. The split is located along the x-axis in the region $-1/2 \leq x \leq 1/2$. It is shown that the presence of the region in which the no slip condition is relaxed generates a two-dimensional flow field in the form of a circulation.

In figure 2.2.6 we show the wall shear stress of the basic flow (black curves) and of the perturbation (blue curves) versus time at different locations. In particular, the left panel refers to the point at which the split closes ($x = -1/2$) and the right panel to the mid point of the split ($x = 0$). Let us consider the left plot first. In this case the wall shear stresses generated by the basic flow and the perturbation are almost in phase. This means that where the split closes (at the end of the vitreoschisis) the total wall shear stress (the sum of basic flow and perturbation) is expected to be larger than in the absence of vitreoschisis.

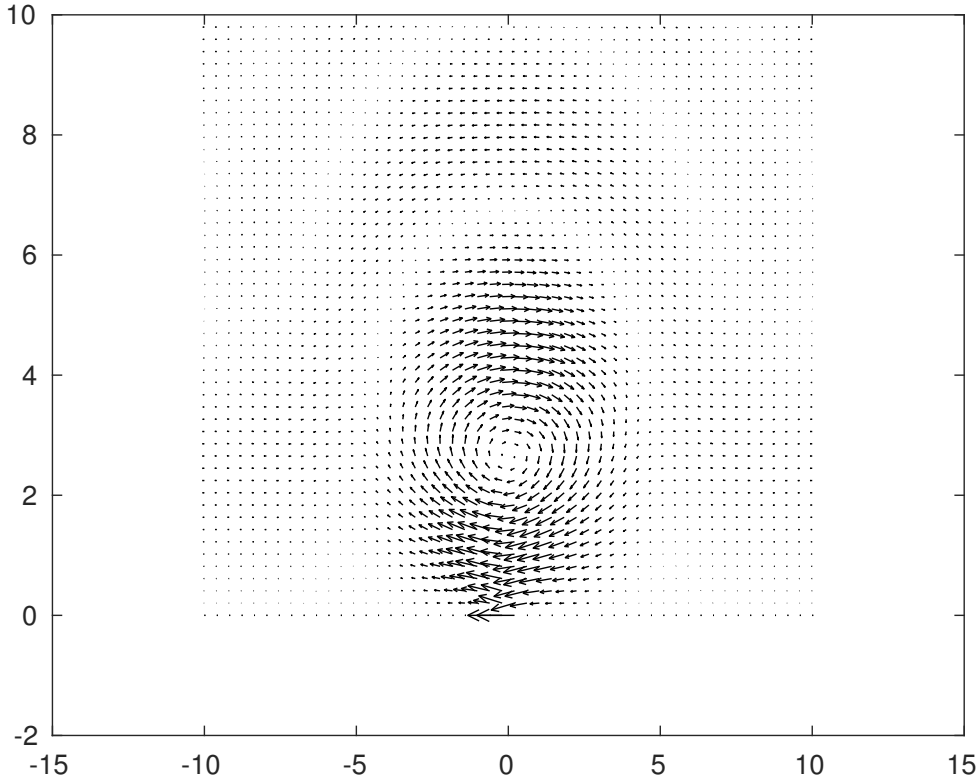

Figure 2.2.5: Perturbation flow field. The Womersley number α_r is equal to 0.16, $\eta = 2.5$ and $t = \pi/2$ that is the time at which the velocity of the perturbation is maximum. The split is located along the x axis in the region $-1/2 \leq x \leq 1/2$.

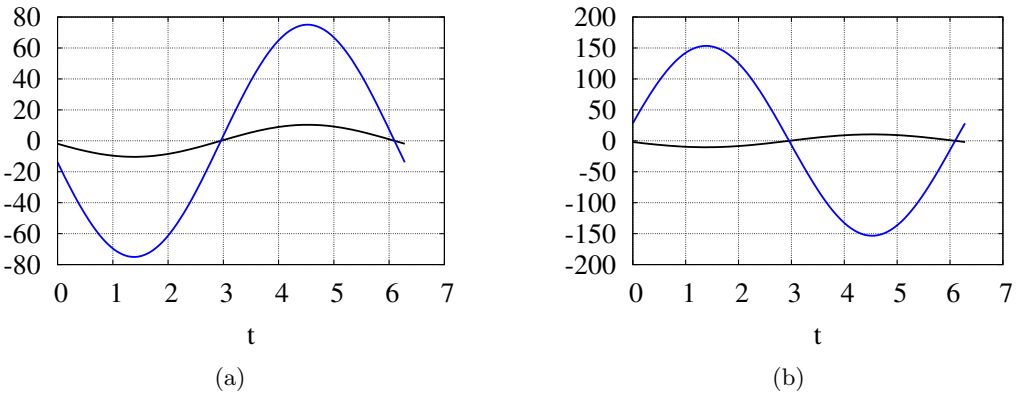

Figure 2.2.6: Wall shear stress of the basic flow (black curves) and of the perturbation (blue curves) versus time at different locations and for different values of the Womersley number. (a) $x = -1/2$ (in correspondence of the point where the split closes) and (b) $x = 0$ (in correspondence of midpoint of the split). The fluid under consideration is viscoelastic with the parameters $\alpha_r = 1.6$, $\eta = 2.5$, which corresponds to the data given by Nickerson et al [35].

The situation is opposite in $x = 0$, i.e. at the mid point of the vitreoschisis (plot in the right). In this case basic flow and perturbation are almost in opposition of phase and thus the effect of the perturbation is to decrease the wall shear stress compared to the case of absence of the split.

In figure 2.2.7 we plot the difference between the phases of the basic flow and perturbation for two different points of the domain - $x = -1/2$ (where the split closes) and $x = 0$ (mid point of the split) for different values of the real Womersey number α_r. The loss factor is fixed and equals to $\eta = 2.5$. The results of both plots are given in radians. At the point where the split closes (figure 2.2.7 (a)) the difference between the phases is relatively small even for large values of α_r, i.e. the perturbation amplifies the resulting value of the maximum wall shear stress at the re-joining point. The opposite result can be observed at the mid point (figure 2.2.7 (b)). The basic flow and the perturbation at this point are almost in opposition of phase and the perturbation will decrease the final value of the maximum wall shear stress at this point.

These results are better understood looking at figure 2.2.8, where the maximum wall shear stress in time (obtained by summing up basic flow and perturbation) is plotted as a function of x. The wall shear stress is normalized with the corresponding value in the absence of vitreoschisis. In the figure we arbitrarily set the small parameter $\varepsilon = 0.06$. The parameters in this case are taken to be equal $\alpha_r = 0.16$, $\eta = 2.5$. This values correspond to the following values of the dimensional parameters: $\omega = 10$ s^{-1}, $G' = 10$ Pa and $G'' = 3.9$ Pa, which were taken from the Nickerson et al [35]. The black curves corresponds to the normalized maximum wall shear stress in the presence of the split while the blue ones corresponds the basic flow. The two vertical red lines show the location of the split: the region of space between the two red lines is where the no-slip condition is partially relaxed.

In agreement with the speculations put forward the wall shear stress peaks at the ends of the vitreoschisis and is minimum at its mid point. This is in agreement with the clinical assumption that in the rejoining poits of the split in the vitreous cortex the retina can

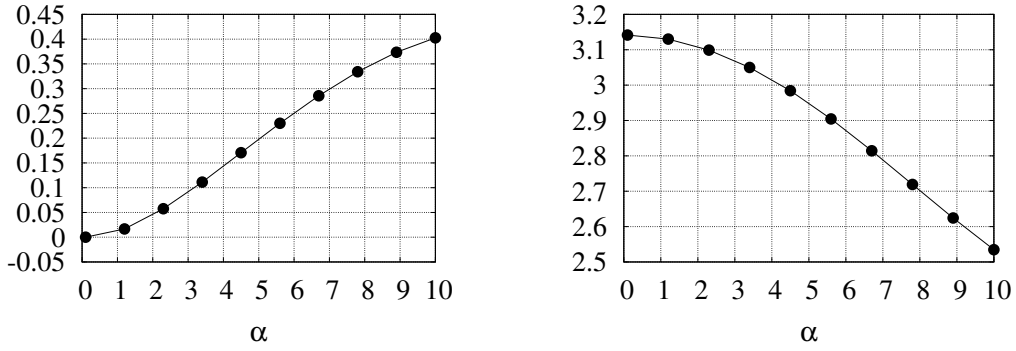

(a) (b)

Figure 2.2.7: The difference between phases in radians of perturbation and basic flow in two different points of the domain - the point where split closes (a) and the middle of the split (b) for different values of the Womersley number. The loss factor is kept fixed and equals to $\eta = 2.5$.

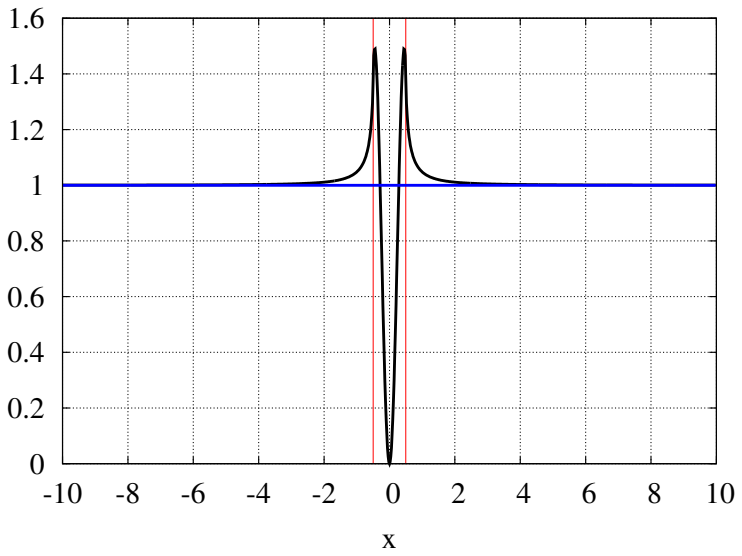

Figure 2.2.8: Maximum (in time) wall shear stress (basic flow plus perturbation) with $\alpha_r = 0.16$, $\eta = 2.5$ and $\varepsilon = 0.06$, along x direction. The stress is normalized with the value corresponding to the basic flow (blue line). The red vertical lines mark the boundary of the split.

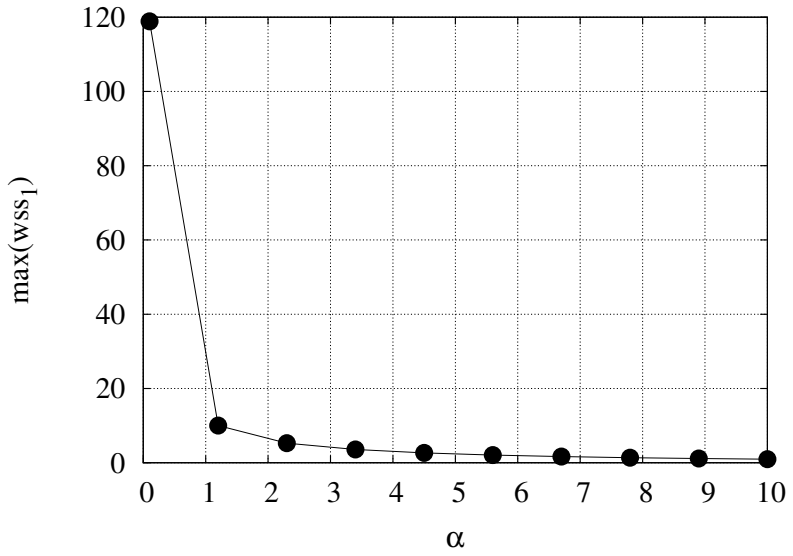

Figure 2.2.9: Maximum wall shear stress for the perturbation at the re-joining point plotted as a function of α_r. The loss factor is fixed and equals to $\eta = 2.5$

experience significant tangential tractions.

In figure 2.2.9 we plot the maximum wall shear stress (in time) at the re-joining point for the perturbation only. The value of the maximum wall shear stress decreases when α_r increases. This implies that when more viscous fluid filles the domain, the stresses at the re-joining point are much higher with respect to the basic state. The fluid under consideration is viscoelastic and the loss factor equals to $\eta = 2.5$.

Three-dimensional model

In figure 2.2.10 we plot the total the maximum total wall shear stress over the surface. We consider a viscoelastic fluid with the complex modulus equal to $G = 10+3.9i$ Pa and frequency of oscillations $\omega = 10$ s^{-1}, which corresponds to the Womersley number $\alpha = 0.7969 + 0.5446i$ (or $\alpha_r = 1.6$ and $\eta = 2.5$). The stress is normalized with the maximum value of the wall shear stress for the basic flow. The figure shows that in the region where the split closes peaks of wall shear stress are predicted by the model (dark red regions).

In figure 2.2.11 we plot the corresponding maximum wall shear stress along the equatorial plane. The red lines indicate the re-joining points of the split. In these regions wall shear stress peaks, whereas it has a minimum in the middle of the vitreoschisis.

The results of the three-dimensional model along the equatorial plane show a very similar behavior as those of the flat case model. The values of the wall shear stress at the joining point can become significantly higher with respect to the basic state during eye rotations.

In figure 2.2.12 we plot the vector field of the velocity at the equatorial plane for the perturbation at time $t = \pi/2$, when the velocity attains its maximum at the wall.

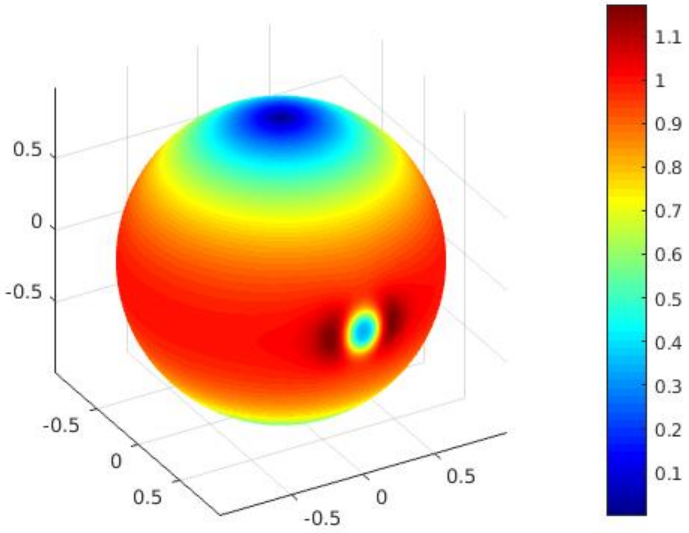

Figure 2.2.10: Map of the total maximum wall shear stress. The complex Womersley number equals to $\alpha_r = 1.6$, loss factor - to $\eta = 2.5$ and $\varepsilon = 0.05$.

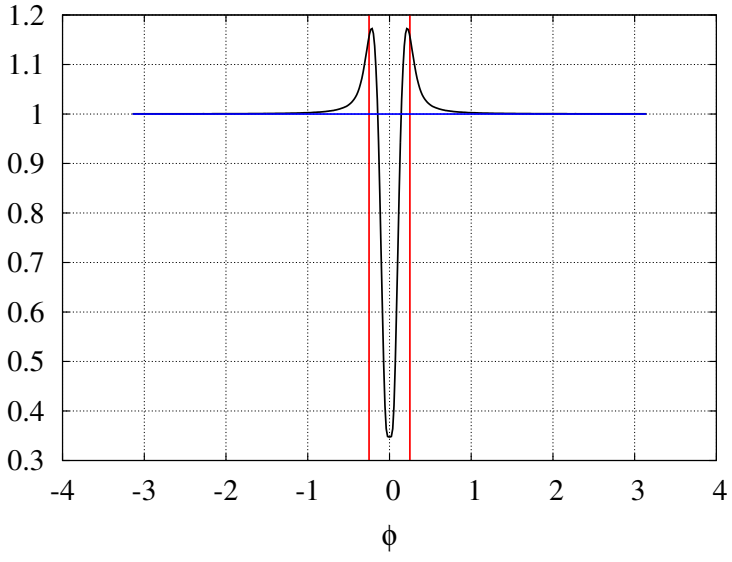

Figure 2.2.11: Maximum wall shear stress along the equatorial plane $\theta = \pi/2$. The stress is normalized with the maximum value of wall shear stress of the basic flow (solid blue line). The red lines mark the points where the split re-joins. The frequency of oscillations is equal to $\omega = 10$ s^{-1}.

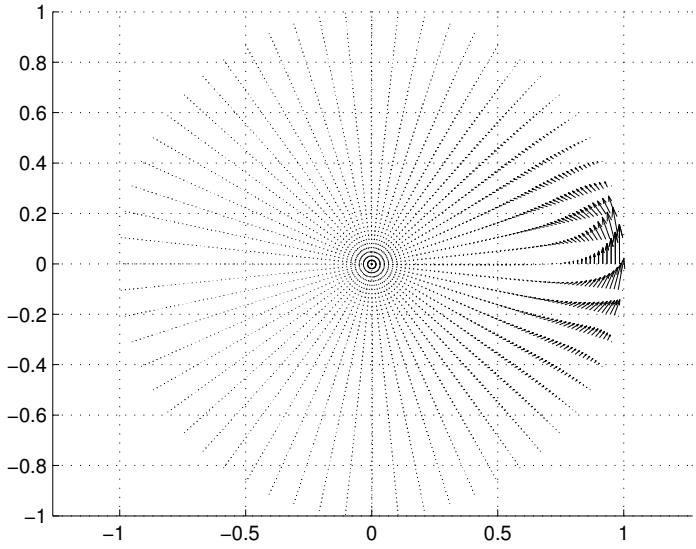

Figure 2.2.12: Velocity vectors on the equatorial plane ($\theta = \pi/2$) for the perturbation in the case of viscoelastic fluid with complex modulus $G' = 10$ Pa, $G'' = 3.9$ Pa and a frequency of oscillations $\omega = 10$ s$^{-}1$.

2.2.4 Discussion

In this section we have presented a model of vitreoschisis, i.e. a split in the vitreous cortex that is found in approximately half of patients with retinal holes and retinal puckers. Vitreoschisis occurs when the vitreo-macular adhesion is very strong. It is believed that the shear stresses at the points where vitreous cortex splits are higher with respect to the rest of the retina.

In this section we set up two different mathematical models with the purpose of studying the mechanics of vitreoschisis. In particular, our aim is to understand how the stress is distributed along the retina in the presence of vitreoschisis and how the maximum stress on the retina changes with respect to the normal conditions.

We first presented a simple two-dimensional model in which the retinal wall is described as a flat surface and the vitreous chamber as a semi-infinite plane. The surface moves harmonically along its plane, to mimic eye rotations. In the second model we consider more realistic conditions, describing the vitreous chamber as a spherical domain, which performs small-amplitude torsional rotations around an axis passing through its center. The sphere is filled with a fluid than can be viscous or viscoelastic.

Both models are based on the assumption that the thickness of the split is much smaller then the size of the domain. Taking advantage of this assumption we do not model the split itself in detail but just account for its effect on the fluid flow by modifying the boundary condition at the wall. In particular, we assume that the effect of the split is to allow some slip between the fluid and the retina. In other words, in correspondence of the split in the vitreous cortex we relax the no-slip boundary condition.

In order to make analytical progress in the analysis we have assumed that the relaxation of the no-slip boundary condition at the wall is "small" which implies that the relative velocity between the fluid and the wall is small compared with the wall velocity. In this way we

can make use of a perturbation approach. We thus consider a "basic flow", which occurs in the absence of vitreoschisis, and a perturbation to the basic flow, induced by the split. The perturbation adds a spatial variation of the velocity at the wall.

The advantage of using the two-dimensional model is that it allows us to obtain a fully analytical solution and to easily interpret the results. We show that the three-dimensional model provides results that are in good qualitative agreement with those of the two-dimensional case.

The results of both models show that during eye rotations, when vitreoschisis is present, the values of the maximum wall shear stress on the re-joining points (where the split closes) is higher with respect to the basic state. This provides a mechanical basis for the clinical observation that these regions are site of significant tractions.

2.3 Vitreous humor with inhomogeneous properties

The natural vitreous humor has a complex structure [9, 40, 44] and it is not homogeneous throughout the vitreous chamber. Moreover, with aging the vitreous gel structure undergoes a progressive disruption. This happens mostly due to degradation of hyaluronic acid, a main component of the vitreous gel structure [45]. In addition, the concentration of collagen in the vitreous structure decreases over time and the vitreous gel collapses. Such a process is known as syneresis. Liquefaction and syneresis together lead to the formation of the liquid lacunae in the vitreous humor structure. These lacunae have a very low collagen concentration with respect to the rest of the vitreous. The decreasing of collagen concentration presumably leads to lower viscosity and/or lower elasticity in these regions. The presence of liquefied regions close to the interface with the retina can lead to the posterior vitreous detachment (PVD), which is harmless in most of the cases.

However, PVD in some cases may be incomplete. This leads to the regions of stronger vitreo-macular adhesion. Shear and normal forces at these regions may cause retinal damage and, consequently, lead to retinal detachment.

In one of the previous sections (2.1) we recall the work of previous authors [1, 2], where the vitreous chamber is modeled as a spherical cavity and the vitreous humor is considered as a homogeneous viscous or viscoelastic fluid. The results show that the shear stress grows with the fluid viscosity, and the viscoelastic fluid can be resonantly excited by eye rotations, leading to large values of the shear stress on the retina.

In section 2.1 we considered a vitreous humor as a homogeneous fluid. In the current section we wish to study shear and normal stresses distribution on the retina in the case of non-homogeneous vitreous properties. In particular, we investigate how the presence of regions with larger viscosity (and viscoelasticity), which can be representative of regions with strong vitreo-macular adherence, might change tractions on the retina during eye rotations.

We model the vitreous chamber as a sphere, which is filled with a fluid that has small variations of its properties throughout the domain; i.e. we assume that the difference in the viscosity and elasticity in different regions of the vitreous is small. This allows us to use a perturbation approach as in the previous section. We assume that in the basic state the fluid is homogeneous, and the perturbation describes the variations of the mechanical properties of the fluid. The solution of the basic flow is exactly the same as was described in section 2.1. The solution for the perturbation is solved by expanding the unknown quantities in terms of vector spherical harmonics and solving the resulting system numerically.

2.3.1 Problem definition

We model a vitreous chamber as a sphere of a radius R^* that performs small amplitude harmonic torsional rotations around the axis that passes through its center with frequency ω^*. As in the previous section it is convenient to work in spherical coordinates (see figure 2.1.1). The velocity vector $\overline{\mathbf{u}}^*$ is composed of the radial $\overline{u}^*$, zenith $\overline{v}^*$ and azimuthal $\overline{w}^*$ components.

The angular displacement of the sphere β is again described by following time law

$$\beta = -A\cos(\omega^* t^*), \tag{2.3.1}$$

where we assume $A \ll 1$. This implies that the velocity of the domain is given by

$$\mathbf{u}^* = A\omega^* R^* \sin\theta \sin(\omega^* t^*)\hat{\boldsymbol{\phi}}. \tag{2.3.2}$$

In order to model a realistic situation, the domain is filled with a viscoelastic fluid that has properties which are non homogeneous throughout the domain, i.e. we assume that the viscous and elastic component of this fluid varies in space in a given way.

The motion of the vitreous humor in the domain is governed by the linearized (following the assumption $A \ll 1$) Navier-Stokes and continuity equations. The boundary conditions we impose are regularity condition at the center of the domain ($r^* = 0$) and the no-slip condition at the wall ($r^* = R^*$).

In this model we assume that the variation of the vitreous humor properties, such as viscosity and elasticity, are of order δ, where $\delta \ll 1$, anywhere in the domain.

We denote by $G^*(r^*, \theta, \phi)$ the complex modulus that describes the viscosity and elasticity of the fluid throughout the domain. Based on the assumption explained above we decompose complex modulus as follows

$$G^*(r^*, \theta, \phi) = G_0^*(1 + \delta G_1(r^*, \theta, \phi)), \tag{2.3.3}$$

where G_0^* is a constant function all over the domain and G_1 is a continuous function, describing spatial variation of the fluid properties.

In the same manner we decompose the velocity vector and pressure field in a basic flow and a perturbation

$$\overline{\mathbf{u}}^* = \overline{\mathbf{U}}^* + \delta\hat{\mathbf{u}}^*, \tag{2.3.4a}$$

$$p^* = P^* + \delta\hat{p}^*. \tag{2.3.4b}$$

The no-slip boundary condition holds. For the leadint order (δ^0) the velocity at the boundary equals to the velocity of the domain (equation (2.3.2)). In order to pass from dimensional to dimensionless variables we use the following scaling:

$$r^* = R^* r, \tag{2.3.5a}$$

$$\overline{\mathbf{u}}^* = \omega^* R^* \overline{\mathbf{u}}, \tag{2.3.5b}$$

$$\overline{p}^* = \rho^* \omega^{*2} R^{*2} \overline{p}. \tag{2.3.5c}$$

The dimensionless parameter of the system is complex Womersley number α which equals to

$$\alpha = \sqrt{\frac{\rho^* \omega^* R^{*2}}{G_0^*/(i\omega^*)}} \tag{2.3.6}$$

Now we solve two problems separately and the final solution is given by the sum of the leading order (δ^0) and perturbation (δ^1) problems.

2.3.2 Leading order problem (δ^0)

Collecting the terms of order δ^9 we obtain that the pressure, radial and zenithal components of the velocity are equal to zero

$$P = 0, \quad U = 0, \quad V = 0, \tag{2.3.7}$$

and the system reduces to the single partial differential equation the solution of which is identical to one in the section 2.1

$$W = -\frac{iA\big(\sin(kr) - kr\cos(kr)\big)}{2r^2\big(\sin(k) - k\cos(k)\big)}\sin(\theta) + c.c., \tag{2.3.8}$$

where $k = \alpha\sqrt{-i}$; and *c.c.* stands for the complex conjugate.

The dimensionless wall shear stress corresponding to the basic flow, scaled with $A\rho^*\omega^{*2}R^{*2}$, is given by the following expression

$$T = -\frac{1}{2}\Big(\frac{1}{1 - k\cot k} - \frac{3}{k^2}\Big)\sin\theta + c.c. \tag{2.3.9}$$

2.3.3 First order problem(δ^1)

The first-order problem is governed by the Navier-Stokes and continuity equations. The boundary conditions are the regularity condition at $r = 0$ and no-slip condition at $r = 1$. As in the case of the basic flow, we apply a separation of temporal and spatial dependencies as follows

$$\hat{\mathbf{u}}(r,\theta,\phi,t) = \mathbf{u}(r,\theta,\phi)e^{it} + c.c., \tag{2.3.10a}$$
$$\hat{p}(r,\theta,\phi,t) = p(r,\theta,\phi)e^{it} + c.c., \tag{2.3.10b}$$

We denote by $\mathbf{\Sigma}_1$ the Cauchy stress tensor at order δ^1. It is given by expression

$$\mathbf{\Sigma}_1 = -p\mathbf{I} + \frac{2}{\alpha^2}\mathbf{D}_1 + \frac{2}{\alpha^2}G_1\mathbf{D}_0. \tag{2.3.11}$$

$\mathbf{D_0}$ and $\mathbf{D}_1$ are the rate of deformation tensors for the base and perturbed flows respectively. Then the governing system of equations reads

$$i\mathbf{u} = \nabla\cdot\mathbf{\Sigma}_1, \tag{2.3.12a}$$
$$\nabla\cdot\mathbf{u} = 0, \tag{2.3.12b}$$
$$|\mathbf{u}| < M, M \in \mathcal{R} \quad (r = 0), \tag{2.3.12c}$$
$$\mathbf{u} = [0 \quad 0 \quad 0] \quad (r = 1). \tag{2.3.12d}$$

Substituting the expression of the Caushy stress tensor 2.3.11 into the governing equation 2.3.12a we get

$$i\mathbf{u} = -\nabla p + \frac{1}{\alpha^2}\nabla^2\mathbf{u} + \frac{1}{\alpha^2}\underbrace{\Big(G_1\nabla^2\mathbf{U} + 2\nabla G_1\cdot\mathbf{D}_0\Big)}_{\mathbf{F}}, \tag{2.3.13}$$

where the components of the vector $\mathbf{F}(r,\theta,\phi) = [F_1, F_2, F_3]$ depend on the solution of the leading order problem $\mathbf{U}$ and the choice of the function $G_1(r,\theta,\phi)$. The components of this vector in the general case are given by:

$$F_1 = \frac{1}{r}\frac{\partial G_1}{\partial\phi}\Big(g' - \frac{1}{r}g\Big), \tag{2.3.14a}$$
$$F_2 = 0, \tag{2.3.14b}$$
$$F_3 = \frac{\partial G_1}{\partial r}\Big(g' - \frac{1}{r}g\Big)\sin(\theta) + i\alpha^2 g G_1\sin(\theta). \tag{2.3.14c}$$

In order to solve the problem at first order (δ^1), $\mathbf{u}$, p and $\mathbf{F}$ are expanded in terms of spherical harmonics.

The scalar spherical harmonics of degree n and order m, for $n \geq 0$ and $-n \leq m \leq n$ are defined by equations (2.2.37) and (2.2.38). The vector spherical harmonics of degree n and order m, $\mathbb{P}_{mn}(\theta,\phi)$, $\mathbb{B}_{mn}(\theta,\phi)$ and $\mathbb{C}_{mn}(\theta,\phi)$ are defined for $n \geq 0$ and $-n \leq m \leq n$ by the equation (2.3.15). The unknown terms of the system, expanded in spherical harmonics:

$$\mathbf{u} = \sum_{n=0}^{\infty}\sum_{m=-n}^{n}\Big[U_{mn}(r)\mathbb{P}_{mn}(\theta,\phi) + V_{mn}(r)\mathbb{B}_{mn}(\theta,\phi) + W_{mn}(r)\mathbb{C}_{mn}(\theta,\phi)\Big], \tag{2.3.15a}$$

$$P = \sum_{n=0}^{\infty}\sum_{m=-n}^{n} P_{mn}(r)Y_{mn}(\theta,\phi), \tag{2.3.15b}$$

$$\mathbf{F} = \sum_{n=0}^{\infty}\sum_{m=-n}^{n}\Big[F_1^{mn}(r)\mathbb{P}_{mn}(\theta,\phi) + F_2^{mn}(r)\mathbb{B}_{mn}(\theta,\phi) + F_3^{mn}(r)\mathbb{C}_{mn}(\theta,\rho)\Big], \tag{2.3.15c}$$

where the functions to determine are $U_1^{mn}(r)$, $V_1^{mn(r)}$, $W_1^{mn}(r)$ and $P_1^{mn}(r)$. The coefficients $F_1^{mn}(r)$, $F_2^{mn}(r)$ and $F_3^{mn}(r)$ are known and depend on the definition of the complex modulus $G_1(r,\theta,\phi)$.

The boundary conditions of the problem are homogeneous. The governing equations for every n and m become:

$$iU_{mn} = -\frac{d}{dr}P_{mn} + \frac{1}{\alpha^2}\Big(\Big(D_n - \frac{2}{r^2}\Big)U_{mn} + \frac{2s_n}{r^2}V_{mn}\Big) + \frac{1}{\alpha^2}F_1^{mn}, \tag{2.3.16a}$$

$$iV_{mn} = -\frac{s_n}{r}P_{mn} + \frac{1}{\alpha^2}\Big(\frac{2s_n}{r^2}U_{mn} + D_nV_{mn}\Big) + \frac{1}{\alpha^2}F_2^{mn}, \tag{2.3.16b}$$

$$iW_{mn} = \frac{1}{\alpha^2}D_nW_{mn} + \frac{1}{\alpha^2}F_3^{mn}, \tag{2.3.16c}$$

where D_n is defined as

$$D_n = \frac{d^2}{dr^2} + \frac{2}{r}\frac{d}{dr} - \frac{s_n^2}{r^2}. \tag{2.3.16d}$$

The continuity equation is given by

$$\Big(\frac{2}{r} + \frac{d}{dr}\Big)U_{mn} - \frac{s_n}{r}V_{mn} = 0. \tag{2.3.17}$$

For $n = 0$ and $m = 0$ the problem is given by:

$$\frac{2}{r}U_{00} + U_{00}'' = 0, \tag{2.3.18a}$$

$$r^2V_{00} + 2rV_{00}'' + a^2r^2V_{00} = -\alpha^2r^2F_2^{00}, \tag{2.3.18b}$$

$$r^2W_{00} + 2rW_{00}'' + a^2r^2W_{00} = -\alpha^2r^2F_3^{00}, \tag{2.3.18c}$$

where the symbol $(')$ denotes the derivation with respect to the radial coordinate r. The solution reads

$$U_1^{00} = \frac{C_0^{00}}{r^2}, \tag{2.3.19a}$$

$$V_1^{00} = C_1^{00}\frac{\sin(ar)}{r} + C_2^{00}\frac{\cos(ar)}{r} - \frac{\alpha^2\sin(ar)}{ar}\int rF_2^{00}\cos(ar)dr + \frac{\alpha^2\cos(ar)}{ar}\int rF_2^{00}\sin(ar)dr, \tag{2.3.19b}$$

$$W_1^{00} = C_3^{00}\frac{\sin(ar)}{r} + C_4^{00}\frac{\cos(ar)}{r} - \frac{\alpha^2\sin(ar)}{ar}\int rF_3^{00}\cos(ar)dr + \frac{\alpha^2\cos(ar)}{ar}\int rF_3^{00}\sin(ar)dr. \tag{2.3.19c}$$

For any $n > 0$ the equation for U_{mn} reads:

$$\begin{aligned} r^4 U_{mn}'''' + 8r^3 U_{mn}''' + r^2 U_{mn}''(12 - 2s_n^2 + a^2 r^2) + 4r U_{mn}'(k^2 r^2 - s_n^2) \\ + U_{mn}(s_n^4 - 2s_n^2 + 2k^2 r^2 - s_n^2 k^2 r^2) = s_n r^2 (s_n F_1^{mn} - F_2^{mn} - r\frac{d}{dr} F_2^{mn}) \end{aligned} \tag{2.3.20}$$

We denote by $\tilde{F}$ the inhomogeneous part of the equation above by

$$\tilde{F} = s_n r^2 (s_n F_1^{mn} - F_2^{mn} - r F_2^{mn'}). \tag{2.3.21}$$

The solution for the U_{mn} then is given by

$$U_{mn} = C_1^{mn} r^{n-1} + C_2^{mn} \frac{J_{n+1/2}(ar)}{r^{3/2}} + r^{-n-1} I_1 + r^{n-1} I_2 + \frac{J_{n+1/2}(ar)}{r^{3/2}} I_3 + \frac{Y_{n+1/2}(ar)}{r^{3/2}} I_4, \tag{2.3.22}$$

where the integrals I_1, I_2, I_3 and I_4 depend on the definition of the complex modulus and can be found numerically.

$$I_1 = \int_0^1 \frac{r^n \Big(J_{n+1/2}(ar) Y_{n+3/2}(ar) - J_{n+3/2}(ar) Y_{n+1/2}(ar) \Big) \tilde{F} \pi}{2a(2n+1)} dr, \tag{2.3.23a}$$

$$I_2 = \int_0^1 \frac{r^{1-n} \Big(- J_{n+1/2}(ar) Y_{n+3/2}(ar) + J_{n+3/2}(ar) Y_{n+1/2}(ar) \Big) \tilde{F} \pi}{2a(2n+1)} dr, \tag{2.3.23b}$$

$$I_3 = \int_0^1 \frac{\pi \tilde{F} Y_{n+1/2}(ar)}{2r^{3/2} a^2} dr, \tag{2.3.23c}$$

$$I_4 = -\int_0^1 \frac{\pi \tilde{F} J_{n+1/2}(ar)}{2r^{3/2} a^2} dr. \tag{2.3.23d}$$

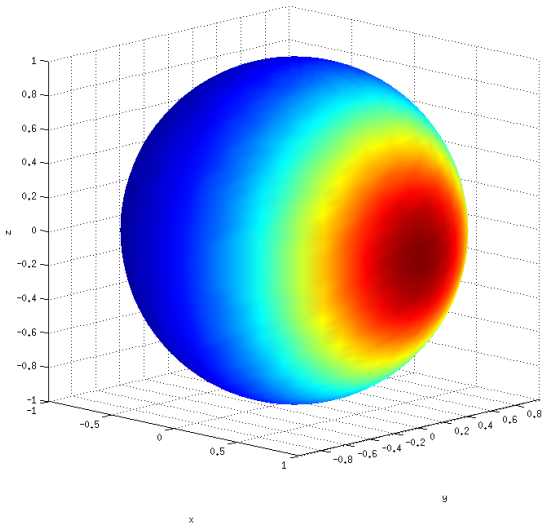

Figure 2.3.1: Viscosity distribution over the surface of the sphere. The maximum value of the viscosity is reached at the point $(x, y, z) = (1, 0, 0)$ or $(\rho, \theta, \phi) = (1, \pi/2, 0)$

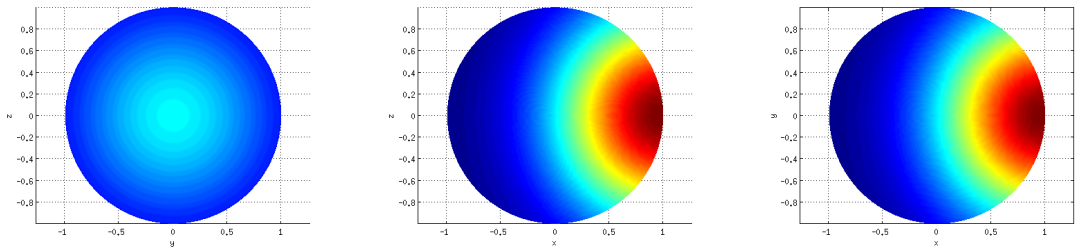

(a) (b) (c)

Figure 2.3.2: Two-dimensional view on the viscosity distribution - three cuts are made normal to x, y and z directions respectively.

2.3.4 Results

The model aims to show how the stresses generated on the retina due to eye rotations are distributed in the case of real vitreous humor, which is a viscoelastic fluid with properties varying in space.

As a first case we have considered a purely viscous fluid, the viscosity of which has a Gaussian distribution, in order to model the situation when the viscosity of the vitreous humor has its maximum value at the back of the eye and it decreases throughout the domain (see figure 2.3.1 and 2.3.2). The mathematical expression describing this variation is as follows

$$G_1 = ie^{-(x-1)^2} e^{-y^2} e^{-z^2}, \tag{2.3.24}$$

so that the maximum viscosity value is on the boundary of the domain at the point $(x, y, z) = (1, 0, 0)$.

In figure 2.3.3 we plot the maximum wall shear stress (WSS). Note that we plot here only the perturbation induced by the variation of the viscosity with respect to the baseline level.

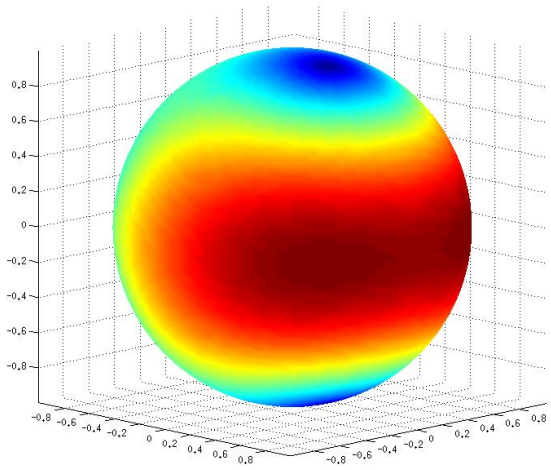

Figure 2.3.3: Maximum wall shear stress for the viscosity plotted on figure 2.3.1.

The WSS peaks where the viscosity is larger than normal.

In figure 2.3.4 we plot the velocity profiles (again only the perturbation with respect to the basic flow) on the plane $\theta = \pi/2$ at two different instants of time ($t = 0,\ \pi/2$). In the figure colors represent the perturbation of the viscosity. It appears that the velocity is larger where the viscosity is larger, since there the velocity of the wall is transmitted into the fluid more efficiently.

2.3.5 Discussion

In this section we studied the fluid motion in the spherical domain, that models vitreous chamber of the eye. The main purpose of this work was to investigate what happens in the real eye when vitreous undergoes natural changes in its structure due to aging. In particular, it is known, that vitreous humor loses hyaluronic acid and the concentration of collagen decreases in some parts of its regions. Both, hyaluronic acid and collagen, are responsible for the elasticity of the vitreous humor and their decrease leads to formation of regions in the vitreous chamber with lower viscosity and/or elasticity. On another hand, vitreous can have regions of higher viscosity and/or elasticity. We aimed in this work to study how such a spatial inhomogeneity in the mechanical properties of the vitreous humor influences the resulting stresses on the retina, generated by eye rotations.

We assumed that the variation of the vitreous humor properties throughout the domain is small, which let us apply a perturbation approach. The solution of the basic flow, which corresponds to the case of homogeneous fluid filling the domain, is given in section 2.1. The perturbation takes into account the variation of mechanical properties of the vitreous humor in space. The solution was found by expanding all the variables in terms of spherical harmonics. The problem has an analytical solution apart from the final integrals, which depend on the definition of the function describing the viscosity and elasticity in space. These integrals were computed numerically.

This model gives us better understanding of what could happen in reality when vitreous

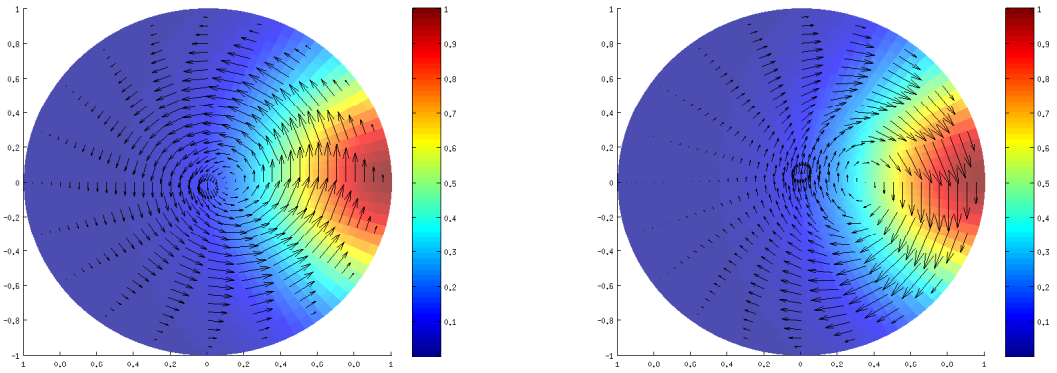

(a) (b)

Figure 2.3.4: Velocity distribution on the plane $\theta = \pi/2$ for two different instants of time - (a) $t = 0$ and (b) $t = \pi/2$. The color bar represents the values of the perturbation of the viscosity.

undergoes changes in its structure due to the aging. In particular, we show that inhomogeneity of its mechanical properties can leads to the generation of high stresses on the retina, which may be related to the formation of retinal holes and retinal breaks. This observation is in agreement with the clinical finding that a inhomogeneous vitreous is required in order to generate potentially harmful tractions on the retina [46].

Chapter 3

Mathematical models of the vitreous chamber in the presence of hydrophobic tamponade fluids

Vitrectomy is a surgical approach to treat retinal detachment, which aims to relieve vitreous tractions on the edge of the retinal breaks [47]. In order to obtain the closure of the passage between the preretinal and subretinal space, it is necessary to induce the retinopexy between retina and choroid. Intraocular tamponades used during vitreoretinal surgery aim at facilitating retinopexy, keeping the contact between retina and choroid in correspondence of the retinal break, until the chorio-retinal scar is well formed [48]. In the early post-operative period the patient has to maintain a precise head position after the surgery, in such a way as to maintain the tamponade fluid in contact with retinal breaks [49].

Typically tamponade fluids used during vitrectomy to treat retinal detachments are hydrophobic. As a consequence of such a property, a thin layer of aqueous is invariably present between the retina and the intraocular tamponade agent.

For a given volume of tamponade fluid injected in the eye, the tamponated retinal surface is strongly affected by the shape of the interface between the tamponade fluid and the aqueous humour. In section 3.1 we study the equilibrium configuration of the interface between the tamponade fluid and aqueous humour, which depends on the physical properties of both fluids, (in particular on density difference, surface tension, contact angle with the retina), on the geometry of the domain and on head orientation.

How the mechanical actions on the retina would change due to the presence of an aqueous layer that separates the tamponade from the retina is not obvious. In section 3.2 we adopt an idealized geometry consisting of a rigid sphere filled with two immiscible fluids (aqueous and vitreous substitute) arranged concentrically, with the aqueous in the external layer, in other words we assume that the thickness of the aqueous layer is uniform over the surface of the retina. This allows us to solve the problem for the motion of two fluids analytically including the maximum value of the shear stress on the wall (retina).

A common problem related to usage of tamponade fluids is generation of emulsion, i.e. the formation of droplets of oil inside the aqueous solution. It is believed that shear instability of the aqueous humour-vitreous substitute interface might be a possible mechanism leading to the emulsification. In section 3.3 we study numerically the linear stability of such interface in the case of a simple two-dimensional geometry using normal mode analysis and assuming

quasi-steady approach.

3.1 Equilibrium shape of the aqueous humour-vitreous substitute interface in vitrectomized eyes

The development of rhegmatogenous retinal detachment (RRD) classically involves the presence of three factors: vitreous traction on the retinal surface, full-thickness retinal breaks, and liquefied vitreous allowing the passage of fluid from the preretinal space, through the retinal breaks (RBs), into the subretinal space [50]. The intraocular surgical approach to treat RRD is vitrectomy that aims to relieve vitreous tractions on the edge of the RBs [47]. In order to obtain the closure of the passage between the preretinal and subretinal space, it is necessary to induce the retinopexy between retina and choroid by closing the passage between the preretinal and subretinal space. Intraocular tamponades, used during vitreoretinal surgery, aim at facilitating retinopexy, keeping in contact retina and choroid in correspondence of the RBs until the chorio-retinal scar is well formed [48]. In the early post-operative period, the patient has to maintain a precise head position after the surgery in such a way as to maintain the tamponade fluid in contact with the RBs [49].

Due to the hydrophobic properties of tamponade fluids used after vitrectomy a pocket of aqueous humor is invariably present in the vitreous chamber after surgery. The maximum filling that the surgeon normally can obtain is approximately 90% of the volume of the vitreous chamber [51]. For a given volume of tamponade fluid injected in the eye, the tamponated retinal surface is strongly affected by the shape of the interface between the tamponade fluid and the aqueous humor. The difference between densities of two fluids, surface tension, contact angle and head position (i.e. the direction of gravity) define the final equilibrium configuration of the interface.

This problem was studied by Eames et al. [52], who modeled the vitreous chamber as a sphere, filled with two different fluids, and determined the shape of the interface using a mathematical approach as well as experiments on a physical model. From their analysis the authors obtained a relationship between retinal coverage and the volume of the injected tamponade fluid.

The main assumption underlying the work by Eames et al. [52] is related to the use of a spherical eye model. In reality, the vitreous chamber is not spherical, in particular owing to the indentation produced in the front part by the lens. The change of concavity of the domain in the anterior part is likely to significantly affect the shape of the interface and it is therefore of clinical interest to study the equilibrium configuration of a tamponade fluid in a realistic eye geometry. In addition, it is relevant to understand how the interface shape might change in myopic eyes, which are at a higher risk of developing retinal detachment and the shape of which is different with respect to that of emmetropic eyes.

To increase the success rate of the surgery it is important to predict the surface of the retina that will be effectively tamponated. In this work we compute the shape of such an interface, both in emmetropic and myopic eyes, which are characterized by vitreous cavities with different geometries. We first consider idealized but realistic shapes of the vitreous chamber and then also use a real eye geometry, reconstructed from magnetic resonance imaging (MRI) measurements. We focus our attention to cases in which the patient maintains the upright position, but the method could be applied to other cases without additional difficulties.

3.1.1 Description of the model

The shape of the interface is computed numerically using the VOF (volume of fluids) method. The basic idea of the method is to introduce a function F, which gives the volume fraction of the tracked phase in the computational cell. This function is equal to 1 when the cell in entirely occupied by one fluid, vanishes when it is entirely occupied by the other fluid and assumes intermediate value when the cell contains the interface.

$$F = \begin{cases} 1 & \text{cell is occupied by fluid 1,} \\ 0 & \text{cell is occupied by fluid 2,} \\ (0,1) & \text{cell contains interface.} \end{cases} \tag{3.1.1}$$

An additional equation for the function F is introduced, which imposes that F moves together with the fluid (its material derivative is zero)

$$\frac{DF}{Dt} = \frac{\partial F}{\partial t} + \mathbf{u} \cdot (\nabla F) = 0 \tag{3.1.2}$$

The VOF method is known to provide a simple and economical way of tracking an interface between two fluids in three-dimensions [53, 54]. The details of the method are given in the Appendix.

Numerical simulations are performed using the free software OpenFoam [55]. All meshes are generated using the *snappyHexMesh* tool by OpenFoam, which produces unstructured meshes consisting of tetragonal and hexahedral volumes. We perform fully three-dimensional simulations using meshes consisting on average of 1.7 millions volumes, and run the code in parallel on a 32 processor computer. For all simulations careful mesh-independence tests have been carried out.

The numerical simulations are run by imposing the volume ratio (ratio of the volume of the injected tamponade fluid to the total volume of the domain) and setting an initially flat and horizontal shape of the interface. Advancing in time the interface evolves towards its equilibrium shape. When a steady solution is obtained, the simulation in completed.

Viscosity does not affect the final configuration reached by the interface. However, it affects the transient phase of the computation, before the steady state is reached. If the viscosity of the two fluids is very large convergence is reached over long times. On the other hand, in the case of low viscosity, waves may form on the interface that can lead to numerical instabilities. In the simulations we tuned the values of the viscosities of two fluids in order to optimize numerical efficiency.

3.1.2 Model geometry

We first consider idealized, yet realistic shapes of the vitreous chamber of the eye. The geometry is constructed on the basis of data from Atchison et. al [5]. The vitreous chamber for an emmetropic eye is shown in Figure 3.1.1(a) on a vertical cross-section of symmetry. The domain is axisymmetric with respect to the horizontal axis that passes through the center of the lens.

Geometries representing myopic eyes are also considered in this section and are constructed using data reported by Atchison et al. [6] (see table 1 of their paper), by stretching the emmetropic eye shape in all directions. For simplicity, we maintained the domain axisymmetric, thus imposing that the inferior-superior and nasal-temporal lengths of the vitreous chamber

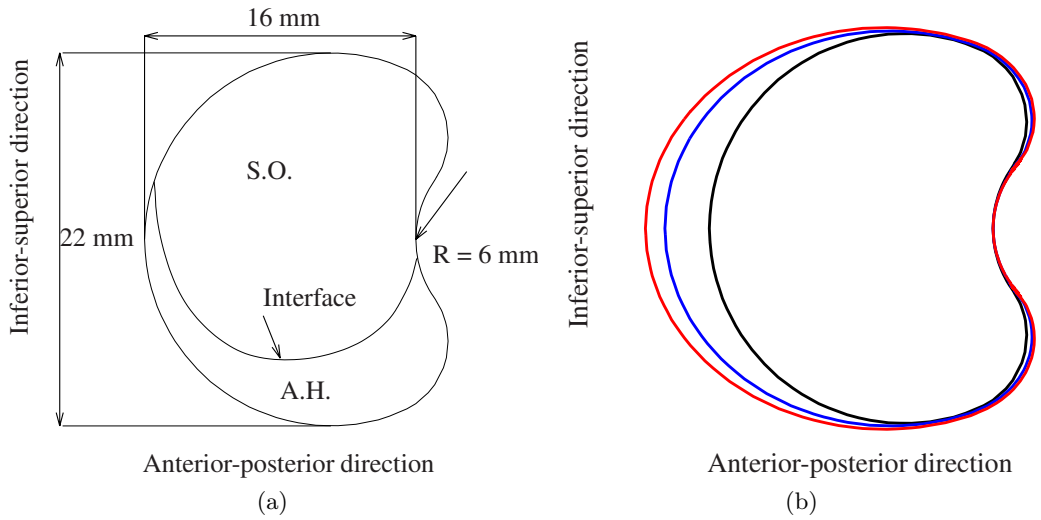

Figure 3.1.1: (a) Vertical symmetry cross-section of the domain for an emmetropic eye. The domain is filled with two immiscible fluids: the tamponade fluid (T.F.) and the aqueous humor (A.H.). All geometrical measurements are taken from Atchison et al. [5]. (b)Vertical cross-sections of myopic eyes. The domains have been obtained stretching the shape of the emmetropic eye in all directions, according to Atchison et al. [6]. In the figure the black line corresponds to the normal eye, blue line refers to myopic eyes with an axial length of 25.5 mm, height and width of 22.3 mm and red line to an axial length of 26.6 mm, height and width of 22.85 mm.

are equal to each other (we took the average of the values reported by Atchison et al. [6] for such lengths). In fact, according to table 1 in the authors' paper, differences between these two lengths are very small. Various myopic eye shapes reconstructed in this way are shown in figure 3.1.1(b), corresponding to different refractive errors.

Obviously, real eyes have more complex shapes than this. However, adopting idealized but realistic geometries allows us to draw general conclusions.

The real eye shape is also considered, with the purpose of showing that the present mathematical model is also applicable in such cases. Contours of real eyes were obtained from high-resolution MR-images by collaborators at the University of Leiden, The Netherlands. In the following we briefly recall the procedure adopted for reconstructing the geometry of the vitreous chamber. The interested reader should refer to the original papers where the methodology is described in detail [56]. Ocular MRI measurements were performed on a Philips (Best, The Netherlands) Achieva 7 Tesla whole body magnet using a custom-made receive eye coil [57]. The images were acquired using a 3D inversion recovery turbo gradient echo technique with an inversion time of 1280 ms, a shot interval of 3 s, and a turbo field echo factor of 92. The TR/TE/flip angle were: 2.5 ms/4.55 ms/16^0. A cued-blinking protocol was used to minimize eye-motion artefacts [58]. The scan resulted in a spatial resolution of $0.5\times0.5\times1.0$ mm^3 and the scan time was slightly less than 3 minutes.

The MR-images were subsequently segmented semi-automatically by in-house developed software, based on the rapid-prototyping platform MevisLab (Fraunhofer MeVis, Bremen, Germany). The central axis, the MR equivalent of the optical axis, was defined as the line from the center of the lens to the center of the vitreous body. A study on the reliability of

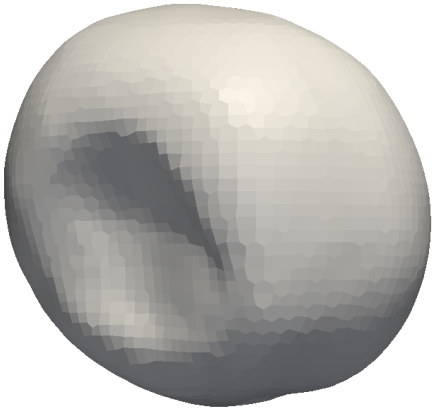

Figure 3.1.2: Reconstructed shape of the vitreous body of an emmetropic eye from MRI.

the technique showed a good agreement with partial coherence interferometry with a mean difference of 0.08 mm between the segmented MR-data and biometry [56]. An example of a reconstructed shape of the vitreous chamber is shown in figure 3.1.2.

3.1.3 Model validation

In order to validate the numerical model we compared the numerical results with the predictions of a home-made numerical model, that computes the shape of the interface between two fluids in a spherical domain. Owing to the axisymmetry of the sphere, in this case the problem reduces to compute the shape of a line, which is the intersection of the interface with a vertical plane across the axis of symmetry (figure 3.1.3).

Mathematically this problem is governed by a system of ordinary differential equations, derived from Laplace-Young law [59]. This problem was studied also by Eames et al. [52]. The Laplace-Young equation is given by:

$$2k_m = \frac{\Delta\rho g}{\gamma} x_I + B, \tag{3.1.3}$$

where the parameters are defined below.

- k_m is the mean curvature of the interface between two fluids; and it equals the divergence of the normal to the interface

  $$2k_m = -\nabla \cdot \mathbf{n}, \tag{3.1.4}$$

  where the choice of the normal defines the sign of the curvature. The curvature is positive if the surface curves towards the normal;

- $\Delta\rho = \rho_2 - \rho_1$ is the density difference;

- g is the acceleration due to gravity;

- γ is the surface tension between two fluids;

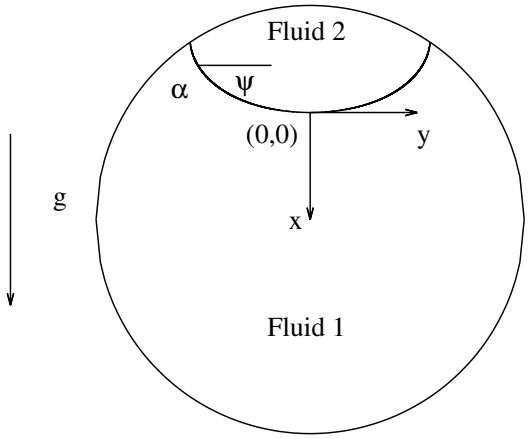

Figure 3.1.3: Cross-section of the spherical domain with two superposed fluids. The origin in placed in the lowest point of the interface between fluids. The governing system of ordinary differential equations is given in terms of parameter ψ, a slope angle of the interval $[0, \alpha]$ with α being a contact angle.

- $x_I = x_I(y)$ is the unknown shape of the interface between two fluids (see figure 3.1.3 for the coordinate system);
- B is a constant, equal to the value of the mean curvature at the origin.

It is convenient to use a parametric representation of the function defining the position of the interface in terms of the slope angle ψ (figure 3.1.3):

$$x = x(\psi), \quad y = y(\psi), \quad \psi \in [0, \alpha], \tag{3.1.5}$$

where α is the contact angle between the interface and the wall (retina). The governing system is given by two ODEs:

$$\frac{dx}{d\psi} = \frac{\sin\psi}{Q}; \quad \frac{dy}{d\psi} = -\frac{\cos\psi}{Q}, \tag{3.1.6a}$$

$$x(0) = 0; \quad y(0) = 0, \tag{3.1.6b}$$

$$Q = \frac{\sin\psi}{y} - \frac{\Delta\rho}{\gamma}x - B. \tag{3.1.6c}$$

The value of the mean curvature at the origin B is initially unknown, i.e. the system has to be solved iteratively. In order to solve the system of equations we adopt the bisection method (see figure 3.1.4).

It requires two initial guesses for the unknown variable B: B_1 and B_2 such that the values of the resulting contact angle $\alpha_1(B_1)$ and $\alpha_2(B_2)$ after integration satisfy the condition

$$(\alpha_1 - \alpha) \cdot (\alpha_2 - \alpha) < 0. \tag{3.1.7}$$

The interval (B_1, B_2) is divided into two and then one of the values of B is updated in such a way that the condition (3.1.7) holds. The iteration method proceededs until a desirable tolerance is reached:

$$|\alpha_1 - \alpha_2| < \text{tol}, \tag{3.1.8}$$

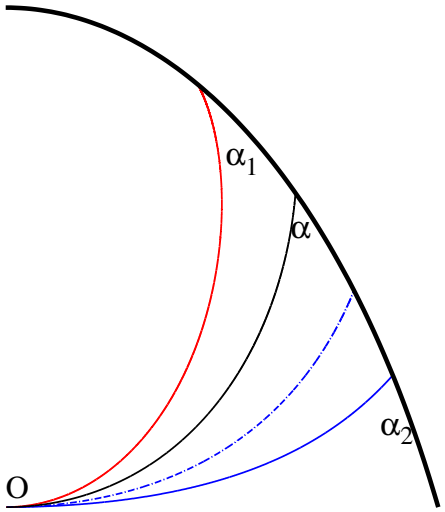

Figure 3.1.4: In this figure we demonstrate the idea of the bisection method. The thick black line is the boundary of the domain. The integration starts from the origin **O**. Starting with two initial guesses for the value of mean curvature at the origin - B_1 and B_2 - we obtain two different resulting curves for the shape of the interface - red for the B_1 and blue (solid) for the B_2. Each of them results corresponding value of the contact angle α_1 and α_2. Then we compute the mean value between B_1 and B_2 wich defines the new value either for B_1 or B_2, such that the curve we are looking for (black line) is placed between two resulting curves. This require that the signs of the differences $(\alpha - \alpha_1)$ and $(\alpha - \alpha_2)$ were different. Updating the value for B_2 (in this case) we get the new curve - dashed blue - and new value for the α_2. This process of undating B_1 and B_2 we continue till the difference between α_1 and α_2 is small enough, i.e. both curves are pleced very close to the correct one.

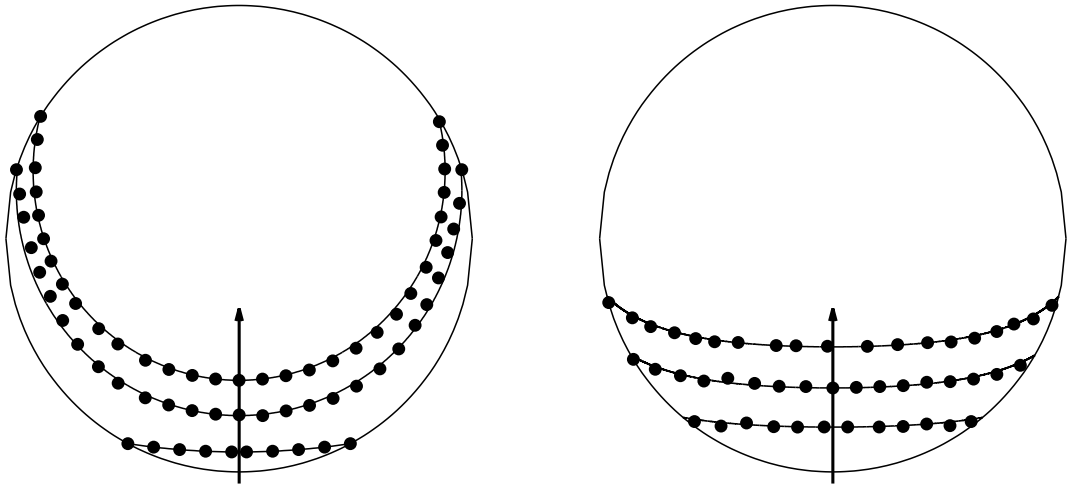

Figure 3.1.5: Equilibrium shapes of the interface in the spherical domain from the analytical solution (solid lines) and from the numerical model(dots) for different volume fractions of the tamponade fluid. (a)Silicone oil; (b) gas. The arrows indicate decreasing values of volume fraction.

i.e. the value of contact angle equals to its real value with the given tolerance.

In figure 3.1.5 we plot the shape of the interface on a cross-section of the sphere. The solid line is obtained with the axysimmetric model, whereas dots are relative to the fully three-dimensional numerical solution obtained with the VOF method. Figure 3.1.5(a) refers to the case of aqueous-silicone oil interface and figure 3.1.5(b) to the gas-aqueous interface. In both cases the fluid below the interface is aqueous humour. The different curves correspond to different volume ratios. Invariably, the results from the two approaches are in very good agreement, which confirms suitability of the VOF method for the purpose of this work.

3.1.4 Results

Emmetropic eyes

We first consider the case of emmetropic eyes with the idealized eye shape reported in figure 3.1.1. Various equilibrium configurations of the interface are shown in figure 3.1.6. Each curve corresponds to a different degree of filling of the vitreous chamber by the tamponade fluid. Figures 3.1.6(a,b) are related to the case of SO and figure 3.1.6(c,d) to the case of gas. In figure 3.1.7 we show three-dimensional views of the interface, corresponding to the case shown in figure 3.1.6 (a) and (c) for a filling ratio $V_{T.F.}/V = 0.85$, where $V_{T.F.}$ denotes the volume of the tamponade fluid and V the total volume of the vitreous chamber. Figures 3.1.7 (a) and (b) correspond to the cases of SO and gas, respectively.

The equilibrium shape of the interface in the real eye is significantly different from that in a sphere. This is most evident looking at the anterior-posterior cross-section (figures 3.1.6 (a),(c)). The indentation produced by the lens, since it induces a change of the concavity of the domain, has a strong effect on the interface shape. In particular, the elevation reached by the interface in the front and back regions of the domain can be very different. Interestingly enough the contact line is higher in the front of the eye for high degrees of filling and the

opposite happens when the filling degree is small (figure 3.1.6(a)).

Comparing the case of the SO to the case of the gas (figures 3.1.6(a,b) vs 3.1.6(c,d)) it appears that the interface is flatter in the case of gas and thus the gas has better tamponating properties than the SO. This is clearly shown in Figure 3.1.8, where we plot the relative tamponated surface (i.e. the ratio between the surface of vitreous chamber in contact with the tamponade fluid $S_{\text{tamponated}}$ and the total bounding surface of the vitreous chamber S) as a function of the volume fraction $V_{\text{T.F.}}/V$. The two curves refer to SO and gas, respectively. The curve corresponding to gas is invariably higher than that corresponding SO. This implies that, for a given amount of tamponade fluid injected into the eye (a given ratio $V_{\text{T.F.}}/V$), the amount of surface tamponated by the gas is larger than that tamponated by the SO.

In Figure 3.1.9 we show the interface shape obtained in the case of a real emmetropic vitreous chamber reconstructed from MRI images, the geometry of which is shown in Figure 3.1.2. The curves correspond to those shown in Figure 3.1.6. In Figure 3.1.8 we also report, with open symbols, the results obtained for the case of the real eye. The model predictions for the idealized and the real geometry are very close to each other. Also in the case of the real geometry the curves corresponding to SO and gas are clearly separated, with that relative to gas showing a larger amount of tamponade surface compared to SO.

In addition to the relative tamponaded area we also calculated the angular coverage of the retina. In this case we only considered the surface of the vitreous chamber covered by the retina. Following the clinical practice this is defined as the region posterior to a plane orthogonal to the axis of the eye and at a distance of 6 mm from the limbus in the antero-posterior direction (see Figure 3.1.10a). We then introduce the angles Ψ and Φ, shown in Figure 3.1.10 and defined as follows. The angle Ψ is the angle of retinal coverage along an antero-posterior plane orthogonal to the equator (see Figure 3.1.10 (a)); the angle Φ is the retinal coverage along the equatorial plane (see Figure 3.1.10(b)).

Comparisons of the tamponade properties of a SO and gas in terms of these quantities are shown in Figure 3.1.11. Again it appears that the gas has better tamponating properties than the SO.

Myopic eyes

We now show the results obtained in the case of myopic eyes and compare them to those found in emmetropic eyes. For the sake of space we consider here only the case of SO. The results for the gas would be analogous but the differences with normal eyes would be smaller than those obtained for the SO, owing to the fact that the interface in the former case is flatter than in the latter.

In figure 3.1.12 we plot the equilibrium shape of the interface for the case of a myopic eye, considering an eye with axial length of 26.6 mm. This figure is analogous to figure 3.1.6(a,b), i.e. we consider three different volume fractions of the SO.

In Figure 3.1.13 we plot the relative tamponated retinal area versus the filling ratio for the case of the emmetropic eye and the corresponding curve for a highly myopic eye. The figure shows that the tamponating effect in the case of the myopic eye is smaller than in the emmetropic one. In fact, the relative tamponated surface $S_{\text{tamponated}}/S$ monotonically decreases with the axial length of the eye, as it is shown in Figure 3.1.14.

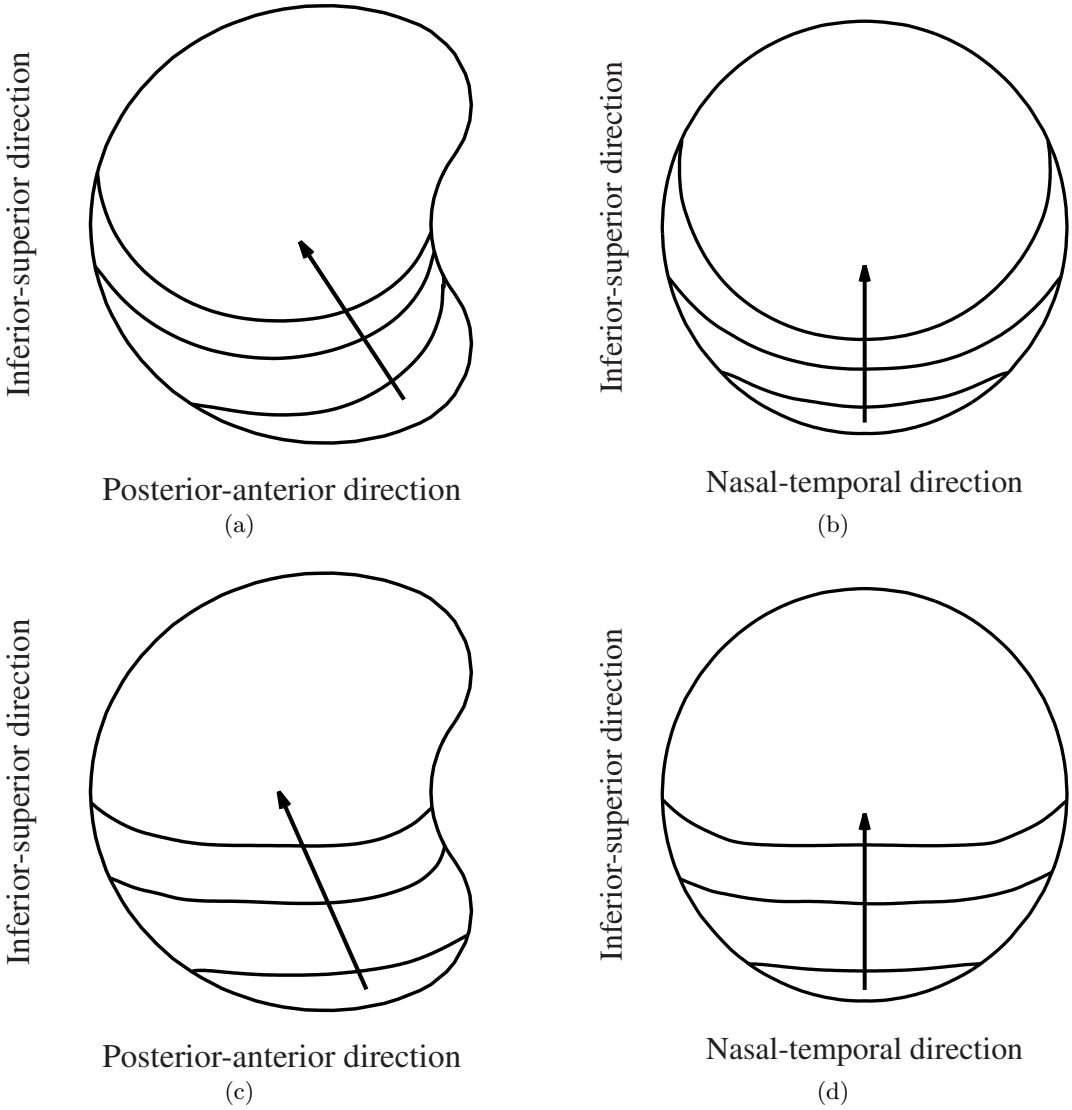

Figure 3.1.6: Resulting shape of the interface in the normal eye for the SO (a,b) and gas (c,d). For both cases we considered three different degrees of filling ($V_{\mathrm{T.F.}}/V = 0.6,\ 0.75,\ 0.9$). The arrows indicate decreasing values of $V_{\mathrm{T.F.}}/V$.

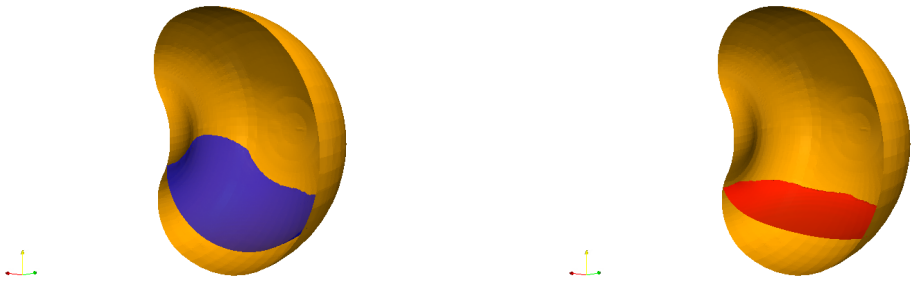

(a) (b)

Figure 3.1.7: Three-dimensional view of the interface shape from two different visual angles. Figure (a) is obtained from the simulation for the SO and figure (b) - for the gas. The degree of filling is $V_{\mathrm{T.F.}}/V = 0.85$ in both cases.

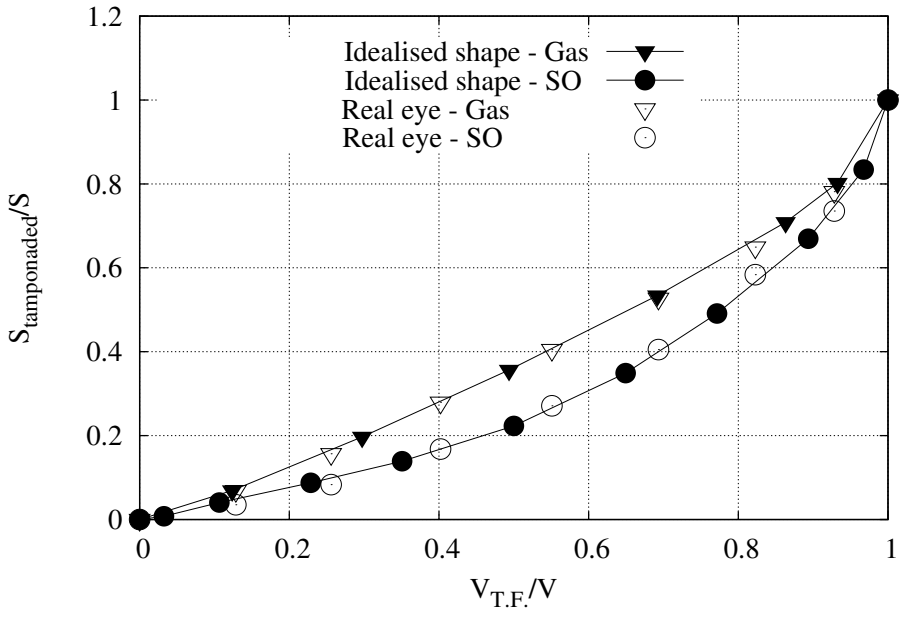

Figure 3.1.8: Relative tamponaded surface as a function of the volume fraction for the case of SO and gas. Solid symbols refer to the idealized shapes of the vitreous chamber and open symbols to a real, reconstructed eye.

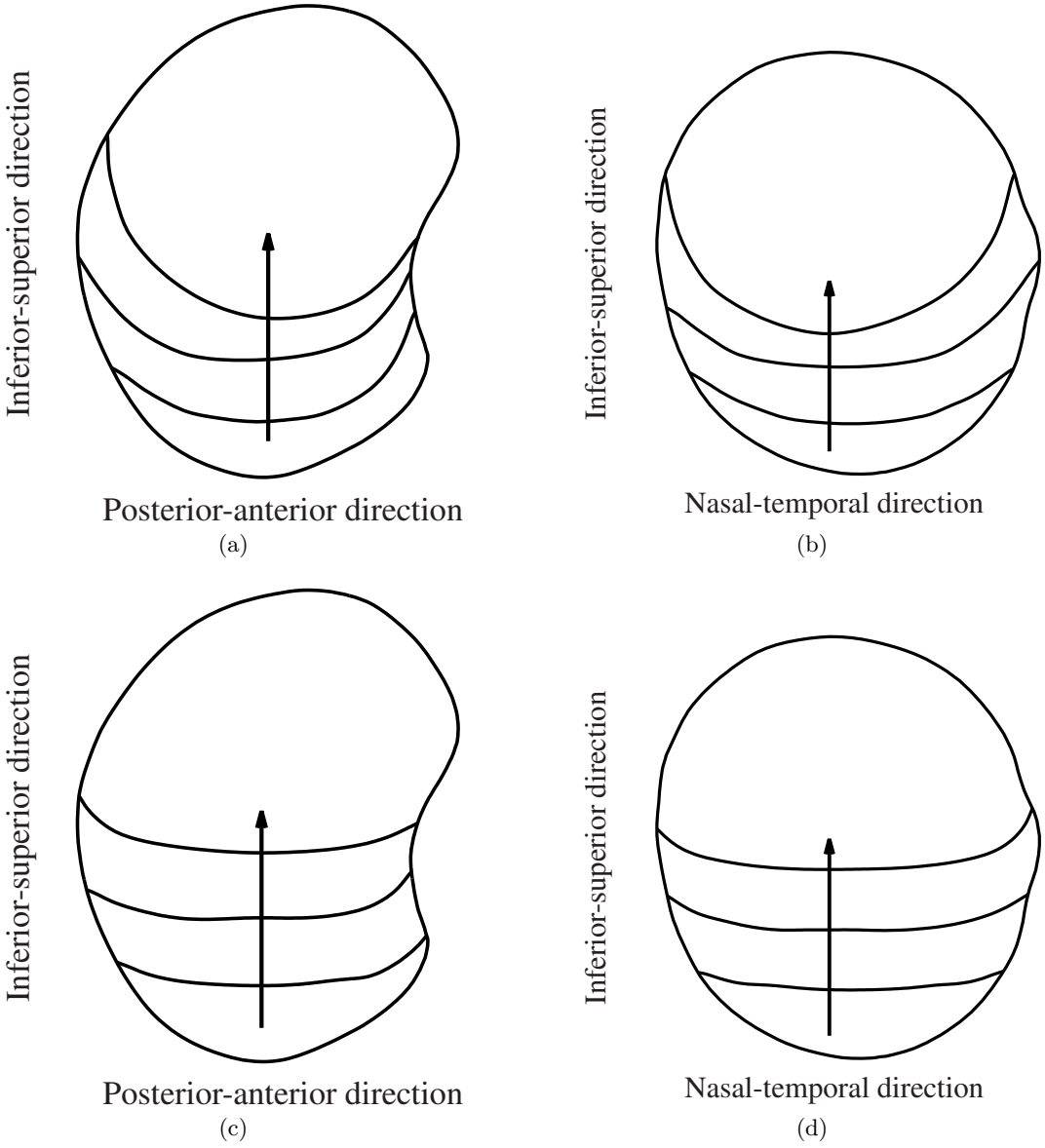

Figure 3.1.9: Equilibrium shapes of the interface in the real eye domain for the SO (a,b) and gas (c,d). The degrees of filling are $V_{\text{T.F.}}/V = 0.6,\ 0.75,\ 0.9$. The arrows indicate decreasing values of $V_{\text{T.F.}}/V$.

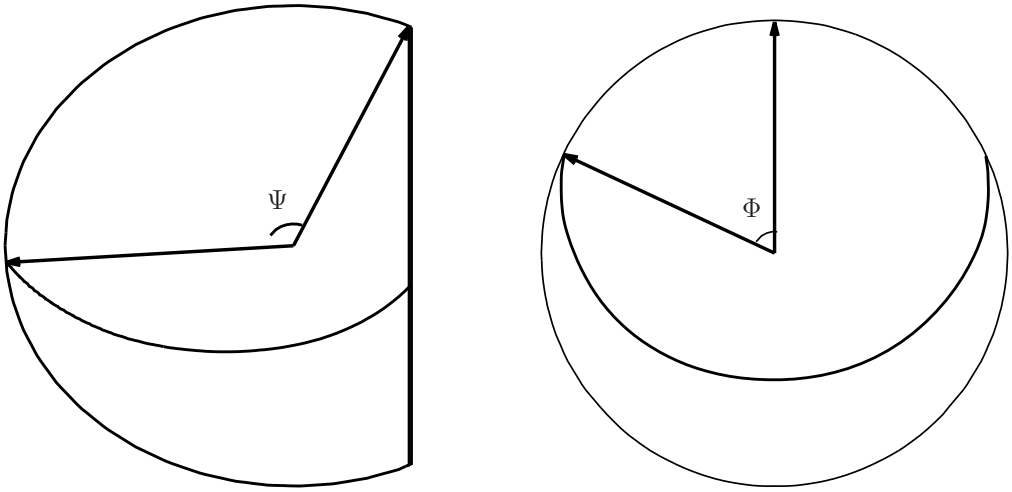

(a) (b)

Figure 3.1.10: Coverage angles Ψ and Φ. In figure (a) we show the way we measure the coverage angle Ψ on the antero-posterior cross-section and in figure (b) the angle Φ on the equatorial plane.

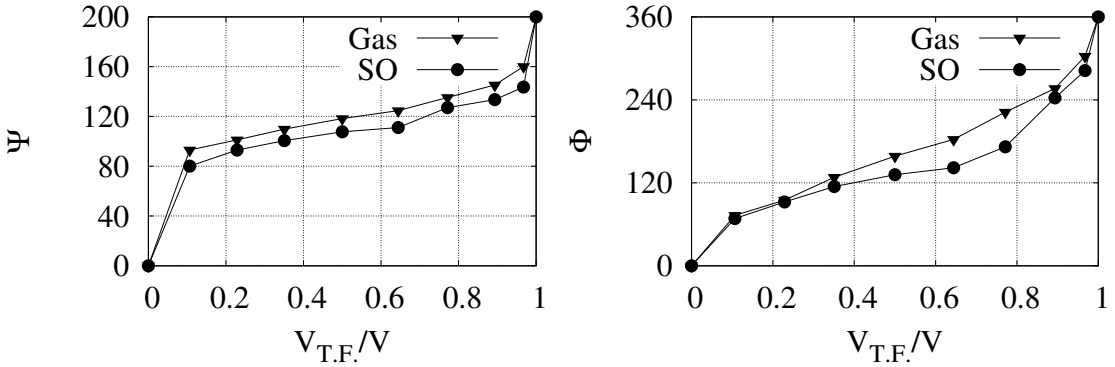

(a) (b)

Figure 3.1.11: Coverage angles Ψ and Φ in degrees versus the filling ratio $V_{\text{T.F.}}/V$ in the case of SO and gas.

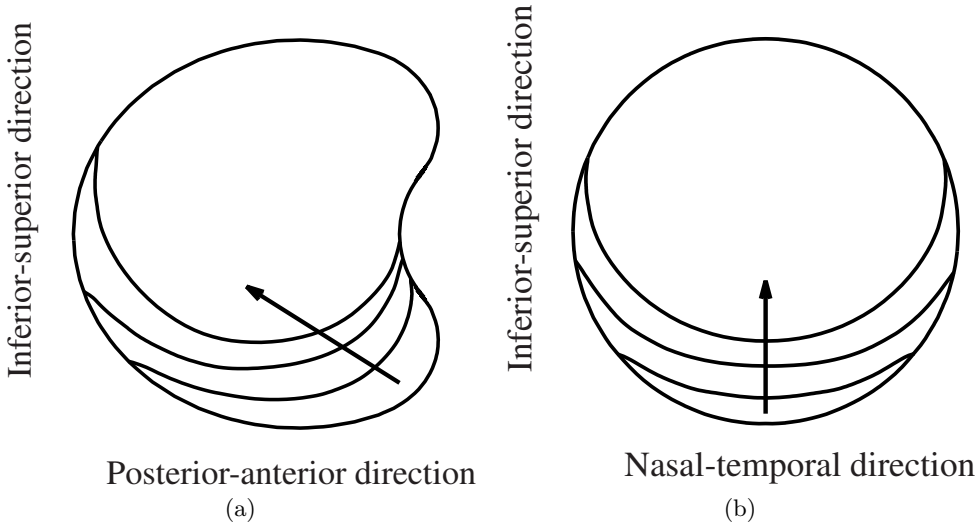

Figure 3.1.12: Equilibrium shapes of the interface in a highly myopic eye for the cases of SO. Axial length is 26.6 mm, height and width are 22.75 mm. The arrows indicate decreasing values of $V_{\mathrm{T.F.}}/V$ and the volume fractions are the same as in figure 3.1.6.

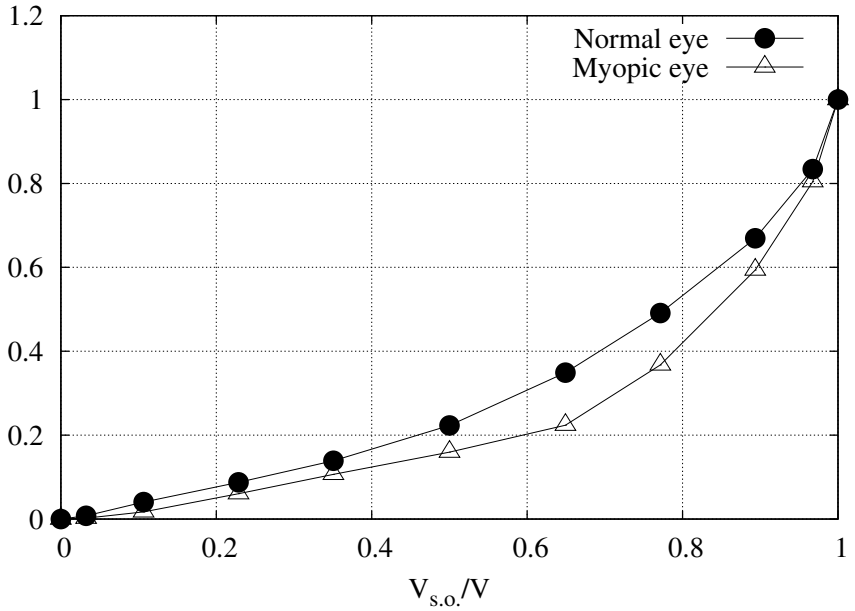

Figure 3.1.13: Relative tamponated surface as a function of the volume fraction for an emmetropic and a highly myopic eye, in the case of SO. The axial length is 24.6 mm.

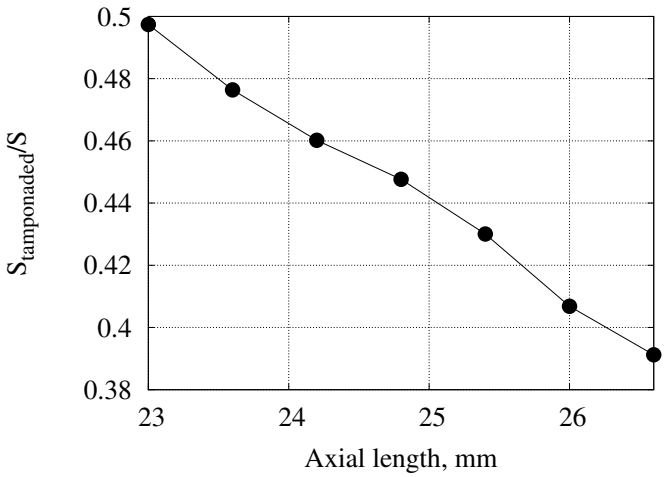

Figure 3.1.14: Relative tamponated surface in the case of SO as a function of the axial length. Filling ratio $V_{\text{T.F.}}/V = 0.81$.

3.1.5 Discussion

Tamponade compounds play an important role in the treatment of retinal detachment. In order to get the best tamponating effect, the surgeon aims to reach a complete filling of the vitreous cavity with the endotamponades at the end of the surgery. Previous reports showed that in the surgical practice the surgeon can not achieve a 100% filling of the vitreous cavity with the tamponade [60] and, an under filling is always present due to the hydrophobic properties of the tamponade. The filling ratio that can be effectively obtained is also affected by the shape of the eyeball and the physical properties of the fluids (mainly their interfacial tension and density). Owing to incomplete filling, the endotamponade is kept away form the retina at least in certain regions of the vitreous chamber, leaving a portion of the retinal surface without any support. Considering that RBs are often multiple and are localized in different quadrants of the retinal surface, it is important for the surgeon in his daily practice to have a better understanding of the shape of the vitreous substitute-aqueous interface and, hence, of the tamponating effect.

Hillier et al [61] investigated the influence of axial myopia on the tamponade efficacy. The experiments were conducted in vitro using 19-mm and 25-mm spherical model chambers to mimic the vitreous cavity. The tamponating efficacy was estimated by measuring the maximum height of the bubble and the arc of contact subtended by the bubble. The authors reported no significant difference in tamponade efficacy according to the size of the eye chamber simulator. The main limit of such a remarkable experiment is the assumption of spherical shape of the vitreous chamber.

In our work we employed a mathematical model and studied the tamponating effect of two different fluids used during the vitrectomy: intraocular gas and SO. We note that the model is based on the solution of well known equations and numerical methods and the results should be expected to be highly reliable.

We considered idealized eye shapes and real eye geometries obtained from MRI-images. In addition to this we also considered idealized eyes with different degrees of myopia. We restricted our attention to the case in which the patient keeps an upright position, however,

the method could be easily adopted to treat cases of different head orientations.

The results show that for patients in the upright position the geometry of the vitreous chamber has a significant impact on the final equilibrium configuration of the interface between the two fluids. This is because the interface intersects the anterior region of the vitreous chamber, where the indentation produced by the lens induces a significant change in the curvature of the vitreous chamber wall.

Gas showed better tamponating properties than SO. This is due to two combined effects. First, the contact angle is smaller in the case of the SO and, second, the density difference is much higher in the case of the gas (see table 1 at the Introduction). As a result the interface with the aqueous is flatter in the case of gas than in the case of SO.

The results obtained in the case of a real eye shape reconstructed from MRI images are very close to those obtained in the idealized case.

We found that the tamponating efficacy is reduced in highly myopic eyes. The curve corresponding to the normal eye is everywhere above that corresponding to the myopic eye, meaning that with the same volume fraction the tamponade effect of the SO is reduced in the myopic eye. This result is interesting and counter intuitive since one would expect that, in a larger domain (as a highly myopic eye is), the interface should be flatter and thus providing a better tamponating effect. This not being the case, implies that changes in the shape play a more important role than changes in the volume of the posterior chamber.

Finally, we would like to note that this work can be clinically valuable tool for eyes with pathological geometries (such as staphyloma) in which the equilibrium shape and position of the tamponade compound might differ significantly from the idealized eye-shapes and a patient-specific evaluation is needed.

In the following section we study how the mechanical actions on the retina would change due to the usage of tamponade fluids and how the properties of such a fluid influence the stresses exerted on the retina.

3.2 A simple model of the flow of two immiscible fluids in a sphere

Recently, the only long-term vitreous substitutes widely employed in the clinical practice are silicone oils. They have suitable properties of chemical stability and transparency and have a high surface tension with the aqueous humor, which is desirable. Depending on the location of the RB oils with different densities (either higher or lower then aqueous) can be adopted [62, 63].

The possible presence of an aqueous layer that separates the tamponade from the retina and forms owing to hydrophobicity of SO is irrelevant where the retina is attached to the pigment epithelium. However, it is crucial in correspondence with the break. In the previous section 3.1 we have showed that the supported area of the retina in static condition is strongly affected by the contact angle between the oil and the retina in static conditions.

The mechanical properties of tamponade fluids (density, viscosity and surface tension with aqueous) influence the efficiency of the treatment and, therefore, a full understanding of the mechanical implications associated with the surgery is desirable. In the current section we aim at clarifying, from a purely mechanical point of view, the implications of adopting tamponade fluids with different mechanical properties. The problem is very complex even if only mechanics is accounted for, and therefore, we introduce an extremely simple theoretical model that sheds some light on specific, yet crucial aspects on the problem.

In Chapter 2, section 2.1 we already considered the effect of the viscosity of the tamponade fluid on the mechanical actions exerted on the retina during eye rotations. We now investigate further factors leading to the successful surgery. In particular, we investigate the changes of the maximum wall shear stress, accounting for the presence of a thin layer of aqueous separating the retina from tamponade fluid.

3.2.1 Mathematical formulation

As in the previous, chapter we consider a spherical domain with radius R^* that performs small amplitude torsional harmonic rotations about an axis that passes through the center of the shpere. The domain is filled with two fluids that we assume are arranged concentrically as shown in figure 3.2.1, so that the aqueous layer thickness is constant and equals to d^*. This is obviously a very strong assumption. However, this allows us to obtain a fully analytical solution. The results are expected to be approximately valid in the cases in which the thickness of the aqueous layer is very small compared to the radius of the eye. We assume that two fluids have densities ρ_a^* and ρ_{vs}^* and viscosities μ_a^* and μ_{vs}^*. The subscript a denotes the aqueous humor and vs the vitreous substitute.

The problem is governed by the Navier-Stokes and continuity equations for two fluids. At the interface between two fluids we impose the continuity of the velocity and the dynamic boundary condition. Zero velocity and no-slip boundary conditions are imposed at the center and the boundary of the domain respectively.

The problem is scaled in the following way:

$$t^* = \frac{t}{\omega^*}, \quad (r^*, d^*) = R^* \cdot (r, d), \quad \mathbf{u_i^*} = \varepsilon \omega^* R^* \cdot \mathbf{u}. \quad p_i^* = \varepsilon \mu_a^* \omega^* \cdot p_i, \tag{3.2.1}$$

where ω^* is the frequency of oscillations and ε is the amplitude of the rotations ($\varepsilon \ll 1$) performing by the domain. Upon scaling the governing equations the following dimiensionless parameters appear:

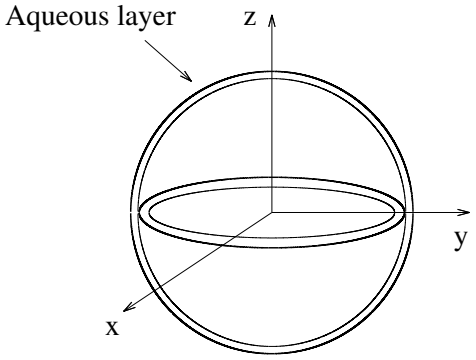

Figure 3.2.1: Sketch of the problem under the consideration. Two fluids arranged concentrically in the sphere are set in motion by the small amplitude torsional rotations of the domain. The internal fluid represents the intraocular tamponade agent while the external fluid is the aqueous humour that separates vitreous substitute and the retina.

$$\alpha = R^* \sqrt{\frac{\omega^* \rho^*_{vs}}{\mu^*_{vs}}}, \quad m = \frac{\mu^*_a}{\mu^*_{vs}}, \quad \gamma = \frac{\rho^*_a}{\rho^*_{vs}}. \tag{3.2.2}$$

To solve the problem it is convenient to consider the Navier-Stokes equations in spherical coordinates. The velocity vectors are $\mathbf{u}_i = [u_i, v_i, w_i]$, where u_i is the radial component, v_i is the zenithal component and w_i is the azimuthal component of the velocities and $i = (a, vs)$.

Owing to the small amplitude oscillations the problem can be linearized. The boundary conditions are the no-slip boundary condition at wall, the continuity of the velocities and the stress across the interface between two fluids, and the regularity at the origin. Due to the specific movement of the domain, i.e. torsional rotations, the radial and zenithal components of the velocity assume the value zero on the boundary, leading to the solution

$$u_{vs} = 0, \quad u_a = 0, \quad v_{vs} = 0, \quad v_a = 0, \tag{3.2.3}$$

so that the only non-zero components of the velocities are the azimuthal ones (w_a and w_{vs}). The system governing the problem is derived from the linearized Navier-Stokes equations and reads:

$$\frac{\partial w_{vs}}{\partial t} = \frac{1}{\alpha^2}\Big[\frac{1}{r^2}\frac{\partial}{\partial r}\Big(r^2\frac{\partial w_{vs}}{\partial r}\Big) + \frac{1}{r^2\sin\theta}\frac{\partial}{\partial\theta}\Big(\sin\theta\frac{\partial w_{vs}}{\partial\theta}\Big) - \frac{w_{vs}}{r^2\sin^2\theta}\Big], \tag{3.2.4a}$$

$$\frac{\partial w_a}{\partial t} = \frac{1}{\alpha^2}\frac{m}{\gamma}\Big[\frac{1}{r^2}\frac{\partial}{\partial r}\Big(r^2\frac{\partial w_a}{\partial r}\Big) + \frac{1}{r^2\sin\theta}\frac{\partial}{\partial\theta}\Big(\sin\theta\frac{\partial w_a}{\partial\theta}\Big) - \frac{w_a}{r^2\sin^2\theta}\Big]. \tag{3.2.4b}$$

We impose the no-slip boundary condition at the wall ($r = 1$), the regularity condition at the origin ($r = 0$) and across the interface ($r = d$) we impose the continuity of the velocity and the continuity of the stress. Normal component of the stress for both fluids equal to zero. So that only the continuity of the tangential stress has to imposed accross the interface. The

components of the tangential stress for the vitreous substitute and aqueous are given by:

$$\tau_{vs} = \frac{\partial w_{vs}}{\partial r} - \frac{1}{r} w_{vs}, \tag{3.2.5a}$$

$$\tau_a = m\Big[\frac{\partial w_a}{\partial r} - \frac{1}{r} w_a\Big]. \tag{3.2.5b}$$

The boundary conditions are then given by:

$$w_a = \sin(\theta)\sin(t) \qquad (r = 1), \tag{3.2.6a}$$

$$w_{vs} \text{ is bounded} \qquad (r = 0), \tag{3.2.6b}$$

$$w_{vs} = w_a \qquad (r = d), \tag{3.2.6c}$$

$$\frac{\partial w_{vs}}{\partial r} - \frac{1}{r} w_{vs} = m\Big[\frac{\partial w_a}{\partial r} - \frac{1}{r} w_a\Big] \qquad (r = d). \tag{3.2.6d}$$

In order to solve the problem we use the following separation of variables for the unknown quantities:

$$w_i = g_i \sin\theta e^{it} + c.c., \quad i = (vs, a), \tag{3.2.7}$$

with *c.c.* standing for the complex conjugate. Substituting these expansions into the governing system of Navier-Stokes equations we get the system for the unknown functions $g_{vs}(r)$ and $g_a(r)$:

$$r^2 g_{vs}'' + 2r g_{vs}' - 2g_{vs} - i\alpha^2 r^2 g_{vs} = 0, \tag{3.2.8a}$$

$$r^2 g_a'' + 2r g_a' - 2g_a - i\alpha^2 \frac{\gamma}{m} r^2 g_a = 0, \tag{3.2.8b}$$

subjected to the following boundary conditions

$$g_a = -\frac{i}{2} \qquad (r = 1), \tag{3.2.9a}$$

$$g_{vs} \text{ is bounded} \qquad (r = 0), \tag{3.2.9b}$$

$$g_a = g_{vs} \qquad (r = d), \tag{3.2.9c}$$

$$g_{vs}' - \frac{1}{r} g_{vs} = m\Big[g_a' - \frac{1}{r} g_a\Big] \qquad (r = d), \tag{3.2.9d}$$

where prime ($'$) denotes the derivation with respect to r. Then the solution is given by:

$$w_{vs} = c_1 j_1(k_{vs} r)\sin(\theta) e^{it} + c.c., \tag{3.2.10a}$$

$$w_a = [c_2 j_1(k_a r) + c_3 y_1(k_a r)]\sin(\theta) e^{it} + c.c. \tag{3.2.10b}$$

where are the constants c_1, c_2 and c_3 are determined by the boundary conditions, j_1, y_1 are the spherical Bessel's functions and k_{vs} and k_a are given by

$$k_{vs} = \alpha\sqrt{-i}, \quad k_a = \alpha\sqrt{-i\frac{\gamma}{m}}. \tag{3.2.11}$$

The wall shear stress attains its maximum value on the equatorial plane and it is given by

$$\tau^{max}|_{\theta=\pi/2} = \Big[\Big(1 - \frac{3}{k_a^2}\Big)(c_2 \sin k_a + c_3 \cos k_a) + \frac{3}{k_a^2}(c_2 \cos k_a + c_3 \sin k_a)\Big] e^{it} + c.c. \tag{3.2.12}$$

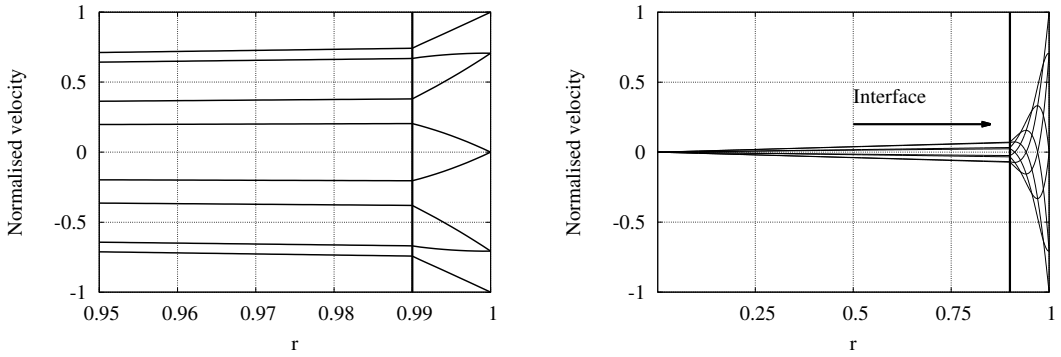

Figure 3.2.2: Velocity profiles in radial direction in the case in which the vitreous chamber contains two immiscible fluids; $r = 0$ corresponds to the center of the sphere and $r = 1$ corresponds to the location of the wall. The velocity is normalized with the maximum velocity at the wall. The frequency of rotations is equal to 10 rad/s. Vitreous substitute $\mu^*_{vs} = 1$ Pa·s; water $\mu^*_a = 0.001$ Pa·s. (a) $d = 0.01$ and (b) $d = 0.1$.

3.2.2 Results

In figures 3.2.2(a) and 3.2.2(b) we show azimuthal velocity profiles on the equatorial plane at different times. The position of the interface between the two fluids is shown in the figure with a vertical solid line. The velocity profiles are continuous across the interface between the two fluids, but their slope is not. This is due to differences between the two fluids viscosities ($\mu^*_a = 10^{-3}$ Pa·s for the aqueous and $\mu^*_{vs} = 1$ Pa·s for the vitreous substitute, e.g., a silicone oil). Figures 3.2.2(a) and 3.2.2(b) differ because the thickness d of the aqueous layer changes in two cases. In the first case (figure 3.2.2(a)) we consider a thickness of the aqueous layer smaller then the thickness δ of the boundary layer ($d < \delta$) that would form at the wall if the aqueous was alone ($\delta^*_a \approx \sqrt{\mu^*_a/\rho^*_a\omega^*}$). In the dimensionless form the boundary layer is scaled with the radius of the domain $\delta^*_a = \delta R^*$. In this case the motion of the wall is also felt in the vitreous substitute, which moves with a significant velocity. On the other hand, when $d > \delta$, most of the motion keeps confined within the aqueous layer and the velocity in vitreous substitute is very small (figure 3.2.2(b)). In other words in the latter case the vitreous substitute barely feels the motion of the wall.

This has an important implication for the wall shear stress, as it shown if figure 3.2.3. In the figure we plot the maximum stress at the wall versus the thickness of the aqueous layer. The stress is normalized with the stress that would be obtained at the wall if the vitreous substitute was completely filling the domain. The thickness of the layer d is scaled with δ. When d/δ tends to zero, the normalized stress obviously tends to 1 (vitreous substitute alone) and the stress on the wall is maximum. However, the figure shows that it is sufficient for a thin layer of aqueous to be present to make the maximum shear stress at the wall drop significantly. When $d/\delta \approx 1$ or greater, the presence of the vitreous substitute is barely felt by the wall and the stress drops to the value it would attain in the presence of aqueous alone. This simple model highlights the importance of accounting for the possible presence of the thin layer of aqueous at the wall in the calculation of the stress on the retina.

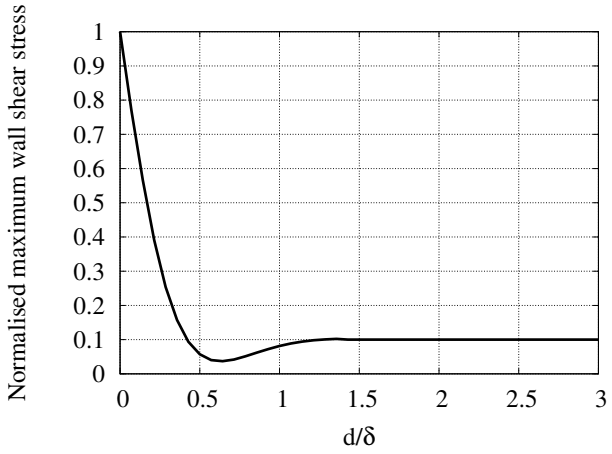

Figure 3.2.3: Maximum stress at the wall versus the thickness of the aqueous layer. The stress is normalized to 1, and the thickness of the layer d is scaled with δ, computed using the viscosity of water. Vitreous substitute $\mu^*_{vs} = 0.96$ Pa·s; water $\mu^*_a = 0.001$ Pa·.

3.2.3 Discussion

In Chapter 2, section 2.1 we have discussed how the stress on the retina depends on the viscosity of a vitreous substitute, under the assumption that the fluid completely fills the vitreous chamber of the eye. In particular, we have shown that the mechanical actions on the retina grow with increasing the fluid viscosity. In reality, the situation is more complicated that this, because, owing to the hydrophobic nature of vitreous substitutes, a thin layer of aqueous may form between the retina and the vitreous substitute.

Therefore, we have considered in this section how the scenario is modified when we account for the presence of a thin layer of aqueous close to the retina.

The results show that when the thickness of the aqueous layer d is relatively small (i.e. it is smaller then the boundary layer δ that would formed if only aqueous filled the domain completely), the vitreous substitute feels the motion of the wall and moves with significant velocity. When the situation is opposite, i.e. $d > \delta$, the velocity of the vitreous substitute is very small.

The presence of aqueous humor layer influences the magnitude of the maximum shear stress on the retina as well. Even though the maximum wall shear stress grows with the fluid viscosity, once a thin layer of aqueous is present, its magnitude drops significantly. In the case when the thickness of the aqueous layer d is larger then the one of the boundary layer δ the value of the maximum shear stress is equal to the one related to the case when only the aqueous humor fills the domain completely. These results have a significant clinical implications, and should be taken into account.

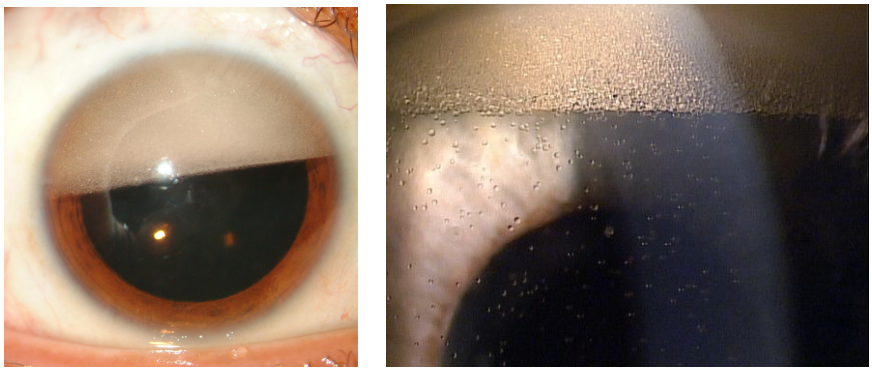

(a) (b)

Figure 3.3.1: Usage of hydrophobic tamponade fluids might lead to the production of emulstion, i.e to the formation of droplets of oil in the aqueous solution. The droplets then may travel to the anterior part of the eye.

3.3 Linear stability of the interface between aqueous humor and vitreous substitutes after vireoretinal surgery

Various fluids can be used during vitrectomy, depending on the particular condition of the patient. Those immiscible with water are silicone oils, perfluorocarbon liquids, and semifluorinated alkane liquids. Depending on the location of the retinal damage, tamponade fluids with densities either smaller (for breaks in the superior part of the chamber) or larger than the aqueous density can be adopted.

At present no vitreous substitute exists that can be left indefinitely in the vitreous chamber, since various complications might arise. In particular, the interface between the vitreous substitute and the aqueous humor might break down and, eventually, an emulsion of droplets might form in the aqueous (see figure 3.3.1). This can lead to various postoperative complications, including cataract, keratopathy, and glaucoma [64].

Owing to the hydrophobic properties of vitreous substitutes, the fluid might not be in direct contact with the retina and some aqueous humor is likely to line the wall of the eye. Winter et al [65] estimated the minimum thickness of the aqueous layer separating the tamponade fluid from the retina to be of the order of 5-10 μm. Vitreous substitute-aqueous interface breakdown may occur both at the wall (in correspondence of this thin film) [66, 67] and at the tamponade fluid-aqueous free interface where, in the case of incomplete filling of the vitreous chamber, the thickness of the aqueous pocket can be quite large (see figure 3.3.2).

Several clinical studies have investigated the conditions leading to the formation of an emulsion. It is generally believed that shear stresses at the tamponade fluid-aqueous interface generated during eye rotations play a crucial role on the generation of the interface instability [66, 68]. This problem remains, however, poorly understood from the mechanical point of view and no modeling approaches have yet been attempted to investigate it.

If the interface breakdown is originated at the wall, it can indeed be related to shear flow instability at the interface between the tamponade fluid and the aqueous. If, on the other hand, it occurs at the free interface between the two fluids, in the case of incomplete filling of the vitreous chamber, other physical mechanisms might play a role, such as sloshing. We focus in this section on the possible role of shear flow instability.

Obviously, the generation of an emulsion is a highly nonlinear process that cannot be understood through a linear stability analysis. However, it seems conceptually relevant to investigate the role that each of the physical quantities involved in the problem has in producing the instability of the vitreous replacement fluid-aqueous interface, which we regard as a possible very initial step toward emulsification.

Owing to the lack of understanding of this instability process, we consider a highly idealized problem that represents the suitable starting point to understand the basic mechanisms underlying the instability process. We consider a flat solid surface representing the vitreous chamber wall (located at $y^* = 0$), performing sinusoidal oscillations along the x^* direction (see figure 3.3.3). We assume that two immiscible fluids occupy the region of space $y^* \geq 0$. The interface between the two fluids is at $y^* = d^*$; fluid 1 (representing the aqueous) occupies the region $0 \leq y^* \leq d^*$, and fluid 2 (representing the vitreous substitute) extends in the y^* direction from d^* to infinity. This geometrical configuration represents well the real case when the thickness of the aqueous layer is much smaller than the radius of the eye, so that the curvature is negligible and the retina can be thought of as a flat surface. Obviously, real eye movements are not exactly harmonic in time. However, a sequence of saccadic rotations in opposite directions can be roughly thought of as a periodic harmonic movement. This is what has been assumed in most theoretical and experimental studies of vitreous humor dynamics [1][69]. Moreover, assuming harmonic oscillations of the plate allows us to find an analytical solution of the basic flow.

The idealized problem shown in figure 3.3.3 resembles studies which can be found in the literature. Most of these studies ([70]-[71]) are based on the so-called quasi-steady approach and/or a Floquet analysis. In the quasi-steady approach, the linear stability problem is solved by "freezing" the basic flow at each instant in time and the method is valid when the frequency of the basic flow is much smaller than that of the perturbation. This cannot be known *a priori* and must be verified from the numerical results. The Floquet analysis, on the other hand, does not depend on the scale separation. In the quasi-steady approach, it is possible to find unstable solutions during an interval within the oscillating cycle of the basic flow. However, this does not necessarily imply that amplification of the perturbation is sustained over the whole period.

In the limit in which density and viscosity of the two fluids are the same and the surface tension vanishes, we obtain the case of the flat Stokes layer. Results [70, 72, 73] show that the critical Reynolds number, based on the displacement thickness of the boundary layer, is less than 200 in the case of the quasi-steady approach while the Floquet analysis gives a critical Reynolds number of about 708.

Several investigations [71, 74, 75] concern one or more fluids above an oscillating wall. The most pertinent cases, in relation to the current study, are the investigations by Yih [74] and Or [75], who studied the stability of a single fluid layer over an oscillating flat wall. In the case of quasi-steady flow conditions and long waves Yih was the first to find that instability occurs during certain phases of the cycle if $\omega^2 Re^2/5 > Fr^{-2}$, where Re is the Reynolds number and Fr is the Froude number, both according to the definition given in the next section.

3.3.1 Mathematical formulation

We consider two immiscible fluids occupying the regions of space $0 \leq y^* < d^*$ and $y^* > d^*$, respectively, with densities ρ_1^* and ρ_2^* and dynamic viscosities μ_1^* and μ_2^*. The flow is induced by periodic motion of the rigid wall located at $y^* = 0$, and the oscillation is described by

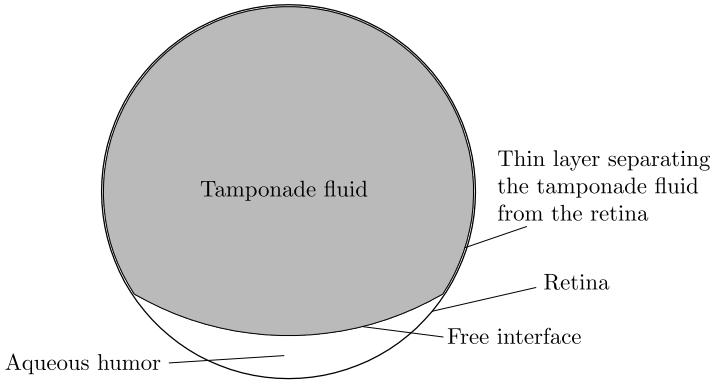

Figure 3.3.2: Schematic sketch of a cross-section on the vitreous chamber filled with a tamponade fluid.

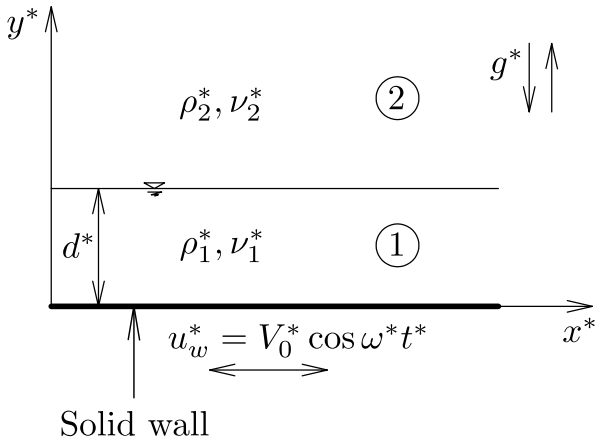

Figure 3.3.3: Sketch of the geometry considered and notation. Note that gravity can act both in the positive and negative directions of y^*, depending on the orientation of the wall.

$$u_w^* = V_0^* \cos(\omega^* t^*) = \frac{V_0^*}{2}(e^{i\omega t^*} + c.c.) \tag{3.3.1}$$

where V_0^* is a velocity representing the amplitude of the oscillations, t^* is time, ω^* is the angular frequency , and *c.c.* denotes the complex conjugate. Let $\mathbf{u}_i^*$ be a velocity vector and p_i^* the pressure, where the index i is taken to be equal to 1 for the fluid closer to the wall and 2 for the other fluid.

The governing equations are made dimensionless using V_0^*, d^*, ρ_1^* as reference velocity, length and density, respectively. The dimensionless variables can therefore be written

$$\mathbf{x} = \frac{\mathbf{x}^*}{d^*}, \quad \mathbf{u}_i = \frac{\mathbf{u}_i^*}{V_0^*}, \quad p_i = \frac{p_i^*}{\rho_1^* V_0^{*2}}, \quad t = \frac{V_0^*}{d^*} t^*, \quad \omega = \frac{d^*}{V_0^*}\omega^*, \tag{3.3.2}$$

where $\mathbf{x} = (x, y, z)$ is the vector of spatial coordinates with x, y and z being stream-wise, wall-normal and span-wise coordinates, respectively. The stability analysis is performed by introducing a decomposition of the solution of the governing equations as

$$\mathbf{u}_i = \mathbf{U}_i + \bar{\mathbf{u}}_\mathbf{i}, \quad p_i = P_i + \bar{p}_i, \tag{3.3.3}$$

where capital letters indicate the basic flow and small letters with a bar refer to perturbation quantities.

Basic flow

We consider the case in which the basic flow is laminar and fully developed in the stream-wise direction. The solution, $\mathbf{U}_i = [U_i(y,t), 0, 0]$, $i = (1, 2)$ is obtained by solving the following system of non-dimensional equations:

$$\frac{\partial U_1}{\partial t} = \frac{1}{Re}\frac{\partial^2 U_1}{\partial y^2}, \tag{3.3.4a}$$

$$\frac{\partial P_1}{\partial y} = -Fr^{-2}, \tag{3.3.4b}$$

$$\frac{\partial U_2}{\partial t} = \frac{m}{\gamma}\frac{1}{Re}\frac{\partial^2 U_2}{\partial y^2}, \tag{3.3.4c}$$

$$\frac{\partial P_1}{\partial y} = -\gamma Fr^{-2}, \tag{3.3.4d}$$

where $Re = V_0^* d^* \rho_1^*/\mu_1^*$ is the Reynolds number, $Fr = V_0^*/\sqrt{g^* d^*}$ is the Froude number, $m = \mu_2^*/\mu_1^*$ is the ratio between the viscosities, and $\gamma = \rho_2^*/\rho_1^*$ between the densities. The boundary conditions are the no-slip boundary condition at the wall, continuity of the velocity and the stress across the interface and zero boundary condition at the infinity. The pressure has hydrostatic distribution and the solution for the velocities U_1 and U_2 is given by:

$$U_1 = [c_1 e^{-ay} + c_2 e^{ay}]e^{i\omega t} + c.c., \tag{3.3.5a}$$

$$U_2 = c_3 e^{-by} e^{i\omega t} + c.c., \tag{3.3.5b}$$

where

$$a = \sqrt{i\omega Re}, \tag{3.3.6a}$$

$$b = \sqrt{\frac{\gamma}{m} i\omega Re}, \tag{3.3.6b}$$

$$c_1 = \frac{e^{a-b}(a+mb)}{2[e^{a-b}(a+mb) + e^{-a-b}(a-mb)]}, \tag{3.3.6c}$$

$$c_2 = \frac{e^{-a-b}(a-mb)}{2[e^{a-b}(a+mb) + e^{-a-b}(a-mb)]}, \tag{3.3.6d}$$

$$c_3 = \frac{a}{[e^{a-b}(a+mb) + e^{-a-b}(a-mb)]}. \tag{3.3.6e}$$

Linear stability analysis

In our analysis we adopt the quasi-steady approach, i.e. we assume that the perturbations evolve on a time scale that is significantly smaller than the characteristic scale of the basic flow. This implies that we study the stability of a "frozen" basic flow at time τ, with $0 \leq \tau \leq 2\pi/\omega$. The validation of this approach can be performed *a posteriori* by checking the relative magnitude of the time scale of perturbations with respect to that of the basic flow.

According to the Squire's theorem, a steady parallel shear flow first becomes unstable to two-dimensional perturbations [76]. The theorem is also valid for quasi-steady flows [77]. Thus, we consider only two-dimensional perturbations, so that $\bar{\mathbf{u}}_\mathbf{i} = (\bar{u}_i, \bar{v}_i, 0)$, $i = (1, 2)$. This allows us to introduce the stream functions

$$\bar{u}_i = \frac{\partial \bar{\psi}_i}{\partial y}, \quad \bar{v}_i = -\frac{\partial \bar{\psi}_i}{\partial x}. \tag{3.3.7}$$

Due to the infinite domain size in stream-wise direction, the solution can be expanded in Fourier modes:

$$\bar{\psi}_i = e^{i\alpha(x-\Omega t)}\psi_i(y,\tau) + c.c., \tag{3.3.8}$$

where α is real-valued dimensionless wavenumber and Ω is the complex-valued phase velocity. Stable and unstable solutions are defined by $\mathcal{I}(\Omega) < 0$ and $\mathcal{I}(\Omega) > 0$, respectively, where $\mathcal{I}$ stands for the imaginary part.

By $\bar{\eta}$ we denote the dimensionless perturbation of the interface position:

$$\bar{\eta} = \eta(\tau)e^{i\alpha(x-\Omega t)+c.c.}. \tag{3.3.9}$$

The governing stability equations are derived by introducing the flow decomposition (equation (3.3.3)), stream function (equation (3.3.7)), and solution forms (equations (3.3.8) and (3.3.9)) into the Navier-Stokes equations, and neglecting nonlinear perturbation terms. The two equations, one for each fluid, read

$$\psi_1'''' - 2\alpha^2\psi_1'' + \alpha^4\psi_1 + i\alpha Re\Big[\psi_1\frac{\partial^2 U_1}{\partial y^2} - U_1(\psi_1'' - \alpha^2\psi_1)\Big] = -i\alpha Re\Omega(\psi_1'' - \alpha^2\psi_1), \tag{3.3.10a}$$

$$\psi_2'''' - 2\alpha^2\psi_2'' + \alpha^4\psi_2 + \frac{i\alpha\gamma}{m}Re\Big[\psi_1\frac{\partial^2 U_2}{\partial y^2} - U_2(\psi_2'' - \alpha^2\psi_2)\Big] = -\frac{i\alpha\gamma}{m}Re\Omega(\psi_2'' - \alpha^2\psi_2), \tag{3.3.10b}$$

where subscript $'$ denotes derivation with respect to y and the basic flow velocity U_i is computed at the generic time τ. The above equations have to be solved subject to following boundary conditions:

$$\psi_1 = 0 \quad (y = 0), \tag{3.3.11a}$$
$$\psi_1' = 0 \quad (y = 0), \tag{3.3.11b}$$
$$U_1\eta + \psi_1 = \Omega\eta \quad (y = 1), \tag{3.3.11c}$$
$$\psi_1' + \eta\frac{\partial U_1}{\partial y} = \psi_2' + \eta\frac{\partial U_2}{\partial y} \quad (y = 1), \tag{3.3.11d}$$
$$\psi_1'' + \alpha^2\psi_1 + \eta\frac{\partial^2 U_1}{\partial y^2} = m\Big(\psi_2'' + \alpha^2\psi_2 + \eta\frac{\partial^2 U_2}{\partial y^2}\Big) \quad (y = 1), \tag{3.3.11e}$$
$$\begin{aligned} &i\alpha Re(\psi_1 U_1' - U_1'\psi_1) - i\alpha Re(\psi_2 U_2' - U_2\psi_2') + (\psi_1''' - 3\alpha^2\psi_1') \\ &- m(\psi_2''' - 3\alpha^2\psi_2') - i\alpha Re\Big((\gamma - 1)Fr^{-2} + \alpha^2 S\Big)\eta = -i\alpha Re\Omega(\psi_1' - \psi_2') \quad (y = 1), \end{aligned} \tag{3.3.11f}$$
$$\psi_1 = \psi_2 \quad (y = 1), \tag{3.3.11g}$$
$$\psi_2 = 0 \quad (y \to \infty), \tag{3.3.11h}$$
$$\psi_2' = 0 \quad (y \to \infty) \tag{3.3.11i}$$

with $S = \sigma^*/(\rho_1^* d^* V_0^{*2})$ being the dimensionless surface tension, where σ^* represents the dimensional surface tension.

The boundary conditions are the no-slip boundary condition (3.3.11a) and (3.3.11b); continuity of the tangential and normal components of the velocity across the interface (3.3.11c) and (3.3.11d). Condition (3.3.11e) imposes the continuity of the tangential stress at the interface and (3.3.11f) states that the difference between the normal stresses across the interface is balanced by surface tension. Finally, (3.3.11h) and (3.3.11i) enforce vanishing of the velocity as $y \to \infty$. Note that, owing to the linearization, the conditions at the interface are imposed in the undisturbed position of the surface, $y = 1$.

The above system of equations (3.3.10) and (3.3.11) has been discretized using a second-order finite difference scheme on discrete points with a constant spacing. Boundary conditions (3.3.11h) and (3.3.11i) are enforced using standard asymptotic inviscid solution. We assume the solution decays at the infinity as an exponent function:

$$\psi_2 \propto e^{-\lambda y}. \tag{3.3.12}$$

Substituting the final expression 3.3.12 in the governing equation 3.3.10 we found that $\lambda = \alpha$.

The discrete system can be written as a generalized eigenvalue problem

$$\mathbf{A}\mathbf{v} = \Omega\mathbf{B}\mathbf{v}. \tag{3.3.13}$$

where $\mathbf{v} = (\psi_1, \eta.\psi_2)$.

3.3.2 Model validation

The physical solution of the linear stability problem is given as a function of the discrete Fourier modes obtained from the solution of equation 3.3.13. It is well known ([72, 72, 78]), that the solution of the linear stability problem of parallel flows in semi-infinite domains is composed of a set of discrete modes and a continuous spectrum. This is true also in this case.

The eigenfunctions corresponding to the discrete modes have their maximum value within the boundary layer, while the continuous modes are traveling waves which are bounded far from the wall and decay in time.

In order to perform the code validation, we compare our results with those of Yih [74], who studied the stability of a single fluid layer over an oscillating flat wall. In the case of quasi-steady flow conditions and long waves, he found that instability occurs during certain phases of the cycle if $\omega^2 Re^2/5 > Fr^{-2}$. We checked our numerical solution in the limit $\gamma \to 0$ and $\alpha \to 0$ against this analytic results, finding excellent agreement.

3.3.3 Energy analysis

In this subsection we study the evolution of the disturbance kinetic energy of the two-fluid system. An equation for the kinetic energy is obtained by first taking the scalar product between the velocity vector and the linearized Navier-Stokes equations, and then integrating over the respective domain $\mathcal{V}_i$. For a given volume, the energy is defined as

$$E_i = \frac{1}{2}\int_{\mathcal{V}_i} \frac{\overline{\mathbf{u}_i}\overline{\mathbf{u}_i}}{2} \tag{3.3.14}$$

And the total disturbance kinetic energy is given by

$$E = E_1 + \gamma E_2 \tag{3.3.15}$$

In vector form, the evolution equation for the disturbance kinetic energy, for the domain $\mathcal{V}_i$, reads

$$\frac{dE_i}{dt} = -\int_{\mathcal{V}_i} \overline{\mathbf{u}}_i \cdot (\nabla \mathbf{U}_i)\overline{\mathbf{u}}_i d\mathcal{V}_i - \frac{1}{Re}\int_{\mathcal{V}_i} \bar{\mathbf{u}}_i \cdot \Delta \overline{\mathbf{u}}_i d\mathcal{V}_i + \int_{\mathcal{S}} \overline{\mathbf{u}}_i \cdot \overline{\sigma}_i \overline{\mathbf{n}} d\mathcal{S}, \tag{3.3.16}$$

where $\overline{\sigma}_i$ is the stress tensor, $\mathcal{S}$ denotes the surface of the interface, and Δ denotes the Laplacian operator. The first term on the right hand side of the above expression is the contribution due to the base flow shear, the second is due to the dissipation, and the third to the interface between the two fluids. The resulting equation, in primitive variable form reads

$$\begin{aligned}
\frac{\alpha}{2\pi}\frac{dE}{dt} = &-\int_0^1 u_1 v_1 U_1' dy - \gamma \int_1^{+\infty} u_2 v_2 U_2' dy \\
&-\frac{1}{Re}\int_0^1 \Big[\Big(\frac{\partial u_1}{\partial x}\Big)^2 + \Big(\frac{\partial u_1}{\partial y}\Big)^2 + \Big(\frac{\partial v_1}{\partial x}\Big)^2 + \Big(\frac{\partial v_1}{\partial y}\Big)^2\Big] dy \\
&-\frac{m}{Re}\int_1^{+\infty} \Big[\Big(\frac{\partial u_2}{\partial x}\Big)^2 + \Big(\frac{\partial u_2}{\partial y}\Big)^2 + \Big(\frac{\partial v_2}{\partial x}\Big)^2 + \Big(\frac{\partial v_2}{\partial y}\Big)^2\Big] dy \\
&\Big(v_1\Big[(\gamma-1)Fr^{-2} + \alpha^2 S\Big]\eta - \frac{v_1}{Re}\Big(\frac{\partial v_1}{\partial y} - m\frac{\partial v_2}{\partial y}\Big) + \frac{1}{Re}\Big(u_1\frac{\partial u_1}{\partial y} - m u_2 \frac{\partial u_2}{\partial y}\Big)\Big)\Big|_{y=1}.
\end{aligned} \tag{3.3.17}$$

In the equation (3.3.17) the dissipation terms are always negative, thus they invariably have a damping effect on the energy evolution. We further note that the effect of the interface dissapears in the case when $S = 0$, $\gamma = 1$ and $m = 1$, i.e. the single fluid.

By definition, the growth rate $\mathcal{I}(\Omega)$ obtained from the solution of the equation 3.3.13 is equal to the logarithmic derivative of the disturbance kinetic energy

$$\frac{1}{2\alpha E}\frac{dE}{dt} = \mathcal{I}(\Omega) \tag{3.3.18}$$

Therefore, by multiplying the left and right-hand side of equation 3.3.17 with $\pi/(\alpha^2 E)$ we can compare the contributions to the total growth rate from the individual terms in the right hand side of 3.3.17.

3.3.4 Estimation of the range of variability of the dimensionless parameters

In this section, we estimate the range of variation of the dimensionless parameters Re, ω, γ, Fr and S, that govern the stability problem referring to the ocular application that motivates this work. Saccadic eye rotations are the fast movements performed when the direction of sight is redirected from one target to another. Becker [79] reports that the relationship between saccade duration T^* and saccade amplitude A is well described by the following linear relationship:

$$T^* = t_0^* + t^* A, \tag{3.3.19}$$

with $t^* \approx 0.0025$ s/deg and $0.02 \leq T_0^* \leq 0.03$ s. In equation (3.3.19), the amplitude A has to be expressed in degree. In this work, we approximate a sequence of eye rotations by describing the eye wall velocity as a sinusoidal function of time, according to 3.3.1. Assuming that this periodic motion is the result of successive eye rotations in opposite directions we can estimate a relationship between the frequency and the amplitude of eye rotations as $\omega^* = 2\pi/(2T^*)$, with T^* computed from 3.3.19. Since, owing to 3.3.19, $A = V_0^*/(\omega^* R_{eye}^*)$, with $R_{eye}^* \approx 0.01$ m being the radius of the eye, this establishes a relationship between the dimensionless parameters Re and ω, which is plotted in figure 3.3.4a. The different curves in the figure correspond to different values of the thickness of the aqueous layer d^*; each point of the curves refers to a different value of the amplitude A, with small values of ω corresponding to large amplitude rotations.

The density and viscosity of the aqueous humor are approximately equal to those of water, thus we assume $\rho_1^* = 10^3$ kg/m^3 and $\nu_1^* = 10^{-6}$ m^2/s.

Vitreous substitutes are characterized by physical properties varying in a very wide range. In this paper, we do not focus on the behavior of a particular vitreous substitute. Rather, we investigate the role of the mechanical properties of the fluid on the instability mechanism. Thus, we will vary the parameters m and γ within a fairly large range of values ($1 \leq m \leq 200, 0.8 \leq \gamma \leq 2$). We note, however, that in the case of silicon oils much higher values of the ratio m than those considered here can be attained.

We finally note that, once values for d^* and σ^* are prescribed, relationships between Re and S, figure 3.3.4b, and between Re and Fr 3.3.4c, can be established.

3.3.5 Results

We first consider pure shear instability and neglect the effect of density differences between the two fluids, thus assuming $\gamma = 1$. Note that in the equations governing the stability problem, the Froude number only appears in the boundary condition 3.3.11f, where it is multiplied by $(1 - \gamma)$. Therefore Fr does not play a role in the stability of the system when the two fluids have the same density.

In order to determine baseline values for the dimensionless parameters, we assume that the layer of fluid 1 has a thickness $d^* = 3 \times 10^{-5}$ m, and that the dimensional surface tension is $\sigma^* \approx 0.02$ N/m. The actual value of the surface tension between silicon oils used in vitreoretinal surgery and aqueous humor can vary within a relatively wide range, owing to the possible presence of surfactants. Here we have chosen a relatively small value for σ^* that

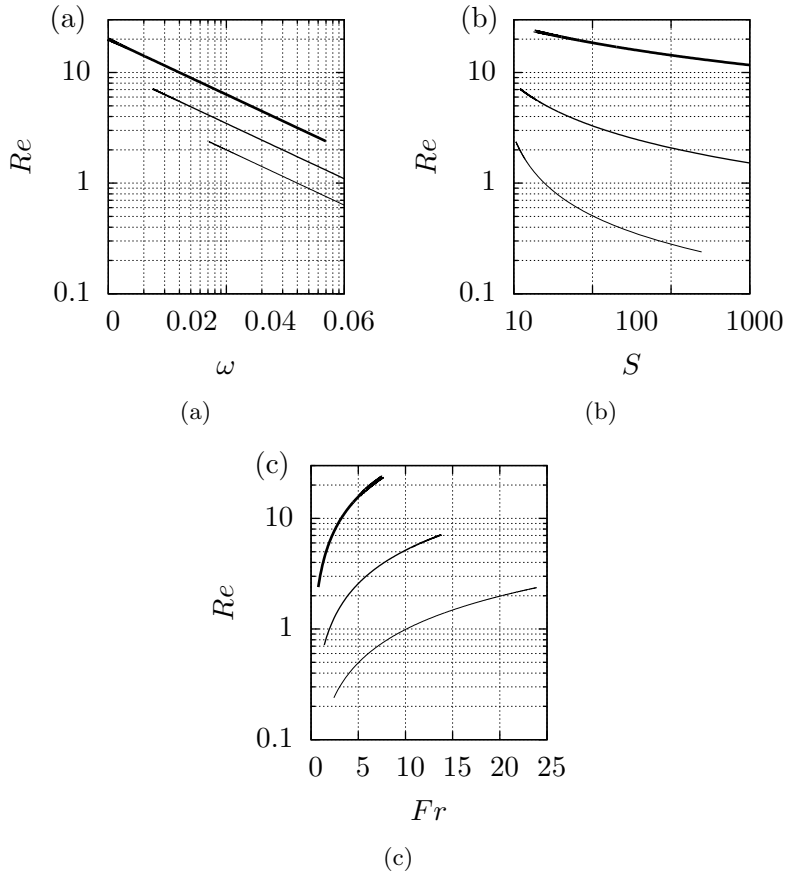

Figure 3.3.4: Relationship between Re and ω (a), S (b) and Fr (c) obtained adopting feasible values for eye movements. From thin to thick curves: $d^* = 1 \times 10^{-5}$ m, $d^* = 3 \times 10^{-5}$ m, $d^* = 1 \times 10^{-4}$ m. Each poit on the curve corresponds to a different value of A.

is representative of what happens in patients who develop oil emulsification, in which cases surfactants are likely to be present [80]. Referring to the curves reported in figure 3.3.4 we assume as baseline values $Re = 7$, $\omega = 0.001$ and $S = 14$. We note that in all cases discussed in the following $\alpha\mathcal{R}(\Omega)$ (which is the measure of the dimensionless frequency of perturbations) is significantly larger than ω, thus ensuring the separation of time scales required for the quasi-steadiness approach to be valid (see figure 3.3.9 and the related discussion below). Where $\mathcal{R}$ refers to the real part.

In figure 3.3.5 we show neutral stability curves, i.e., curves on which $\mathcal{I}(\Omega) = 0$, on the plane $(\omega t/\pi)$-L, where $L = 2\pi/\alpha$ is the dimensionless wave length of the perturbation. Each curve corresponds to a different value of the ratio between fluid viscosities m, and all other dimensionless parameters are kept fixed. In the range of values of the parameters shown in the figures, sufficiently long waves are linearly unstable during certain phases of the basic flow cycle. Note, however, that in all cases shown in the figure, the interface is stable during most time instants. Whether amplification will actually occur, over one or more periods, depends on the value of the growth rate and on the initial magnitude of perturbations.

By definition, the growth rate computed with the energy analysis (subsection 3.3.3) coincides with that computed solving the eigenvalue problem 3.3.13. However, the energy analysis allows us to obtain a better insight on the mechanisms governing the instability. In figure 3.3.6 we show how the various contributions to the energy change appearing in equation 3.3.17 depending on L, for a given time (3.3.6 (a)) and on ωt, for a given perturbation wave length (3.3.6 (b)). In the figure we also plot the growth rate $\mathcal{I}(\Omega)$, suitably scaled to fit in the plot ($\mathcal{I}(\Omega)$ has been multiplied by 300). The figure shows that the leading energy production term is related to the existence of the interface, i.e., the term computed in $y = 1$ in equation 3.3.17. Note that this contribution vanishes when $m = 1$, $S = 0$, and $\gamma = 1$, i.e. when a single fluid is present.

In figure 3.3.7 we show the effect of changing the ratio m between two fluid viscosities. In the figure, we plot the value of the growth rate $\mathcal{I}(\Omega)$ versus m for different values of the perturbation wave length L. As the value m increases, the minimum length of unstable waves grows. However, there exists a value of m (≈ 21.6) for which a maximum value of $\mathcal{I}(\Omega)$ is attained. Thus increasing m has a twofold effect: on one hand short waves are stabilized, on the other hand, for relatively small values of m (< 21.6) he system becomes effectively more unstable, since the growth rate also increases. For $m > 21.6$ further increase of the ratio between the fluid viscosities has an overall stabilizing effect.

In figures 3.3.8(a) and 3.3.8(b) we investigate the effect of modifying the values of S and Re (keeping m fixed and equal to 5). In particular, we show how the shortest unstable wavelength changes with these parameters. As one would intuitively expect, when the surface tension parameter S is decreased, the flow becomes more unstable, in the sense that progressively shorter waves become unstable. In a similar manner, the flow becomes more unstable if the Reynolds number is increased.

We finally consider the effect of changing the value of γ. If the lighter fluid is on top, the effect of gravity is to stabilize the interface. We therefore focus on cases in which the aqueous layer is very thin and the heavier fluid is on top. This means that we consider either the lower portion of the vitreous chamber when a heavier than water vitreous substitute is adopted, or the upper region of the retina when a lighter than water fluid is used. These situations are believed to possibly occur in practice [66, 67, 80]. Figure 3.3.8 (c) shows that if γ increases, the system moves toward instability, again meaning with this statement that progressively shorter waves are found to be unstable.

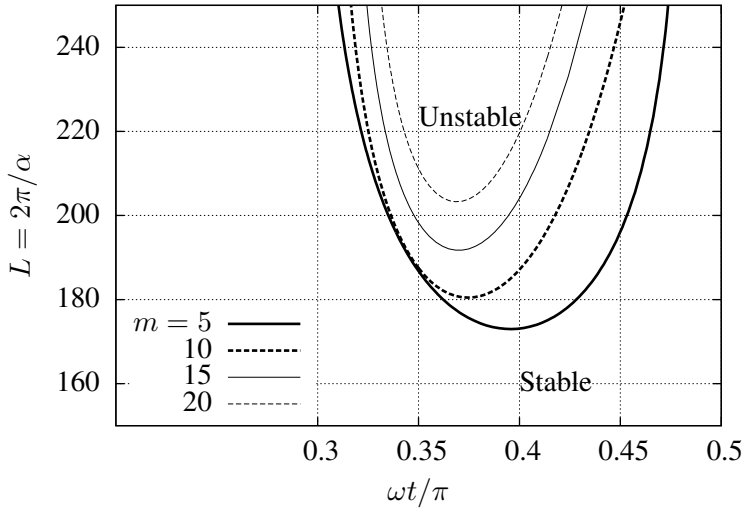

Figure 3.3.5: Natural stability curves in the $\omega t - L$ plane for different values of parameter m(=5, 10, 15, 20), $Re = 7$, $\omega = 0.001$, $S = 14$, $\gamma = 1$.

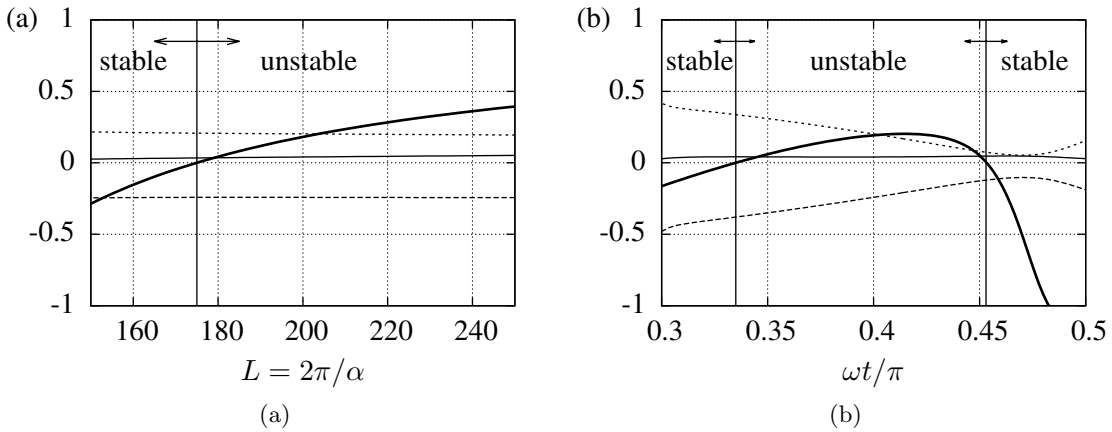

(a) (b)

Figure 3.3.6: Contribution to the perturbation energy growth versus L for $\omega t/\pi = 0.4$(a) and $\omega t/\pi$ for $L = 200$ (b) (see equation 3.3.17). Thin solid curve: volume integral production term. Dashed curve: volume integral dissipation term. Dotted curve: surface integral on the interface. In the figures, we also report with a thick solid curve the growth rate as computed solving the eigenvalue problem, suitably scaled for readibility. This curve allows one to distinguish stable and unstable regions in the plot. In both figures $Re = 7$, $S = 14$, $m = 5$.

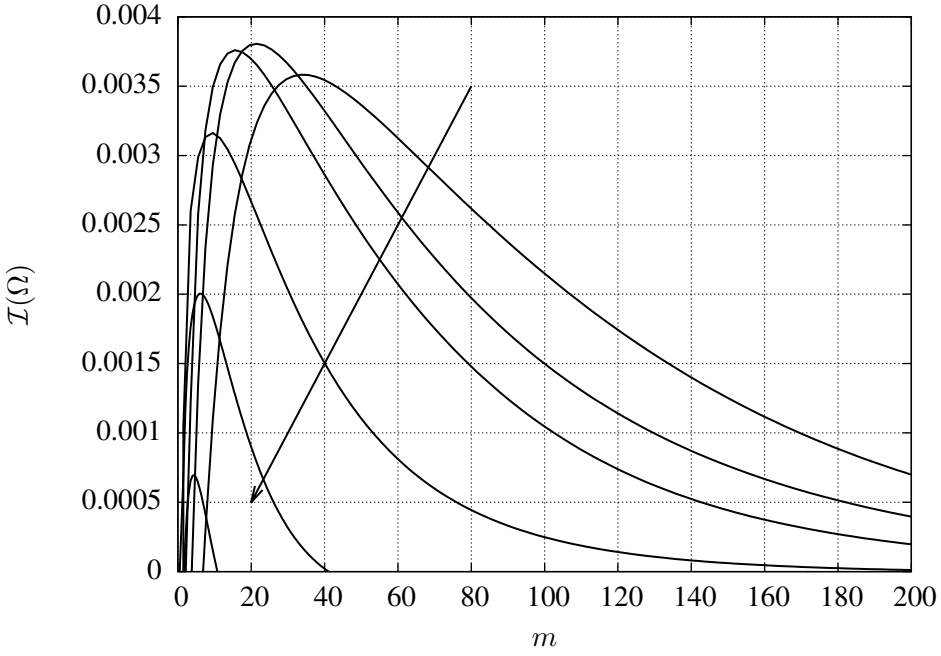

Figure 3.3.7: Growth rate $\mathcal{I}(\Omega)$ versus m for different values of perturbation wave length L (= 200, 300, 500, 800, 1000, 1400). The arrow points to decreasing values of L. $\omega = 0.001$, $Re = 7$, $S = 14$, $\gamma = 1$.

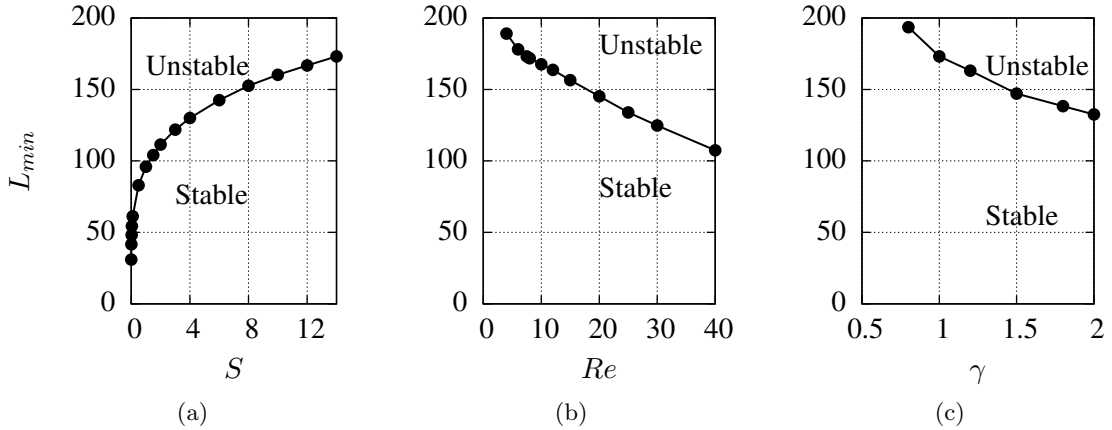

Figure 3.3.8: Length of the shortest unstable perturbation L_{min} versus S (a), Re (b) and γ (c) with $\omega = 0.001$ and $m = 5$. The values of $Re = 7$ in (a) and (c), $S = 14$ in (b) and (c), and $\gamma = 1$ in (a) and (b) respectively.

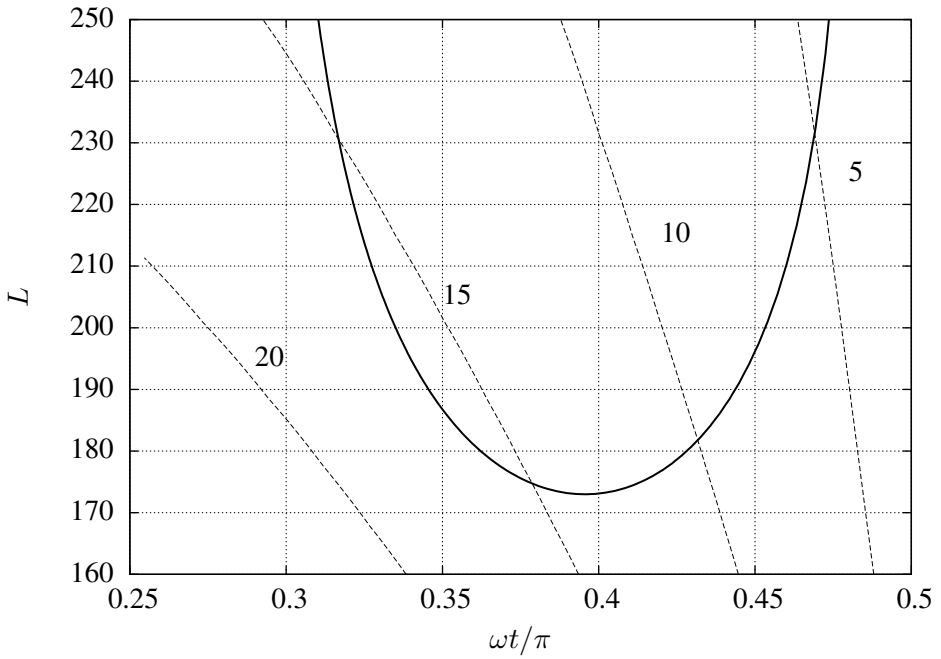

Figure 3.3.9: Neutral stability curve (solid line) in the ($\omega t/pi$)-L plane for the case $m = 5$, $Re = 7$, $\omega = 0.001$,$S = 14$, $\gamma = 1$. The dotted lines show the values of the ratio $\alpha\mathcal{R}(\Omega)/\omega$

.

3.3.6 Discussion

In this section we consider the geometry shown on figure 3.3.3 and study the linear stability of the interface between the two immiscible fluids 1 and 2, assuming that fluid motion is induced by periodic oscillations of the solid wall along the x^*-direction. We adopt quasi-steady approach, thus assuming that perturbations evolve on a time scale which is shorter than the time scale of evolution of the basic flow.

We first consider the case in which two fluids have the same density and different viscosities ($\gamma = 1$, $m \neq 1$). The linear stability analysis shows that, for the range of the controlling parameters considered, long enough waves are linearly unstable during certain phases of the cycle.

There is a value of the ratio $m = \mu_2^*/\mu_1^*$ between the viscosities of two fluids for which the instability of the interface is maximized. When m is large enough or when the viscosities of the two fluids are almost matching, the system is found to be stable, in the range of values of the controlling parameters considered in this section.

Investigation of the dependency of results on the other controlling parameters shows that the system can be destabilized either by decreasing the surface tension parameter S or increasing the Reynolds number characteristic of the flow. We also consider the effect of changing the ratio γ between fluid densities. In particular, we focus on the case in which the heavier fluid is on top. As expected, in this case the system moves toward instability. Among the considered dimensionless parameter, those with a larger influence on the stability of the system are found to be the ratio m between fluid densities and the surface tension parameter S.

The analysis performed in this section is motivated by the need of understanding the stability conditions of the interface between the aqueous humor layer close to the retina and a vitreous substitute in vitrectomized eyes. We adopt a highly idealized geometry and fluid flow structure, which obviously, represent a gross simplification of the fluid dynamics inside of a real eye. However, the idealized geometry can provide insight on the onset of the aqueous-vitreous substitute interface instability in the case in which the thickness of the aqueous layer is much smaller than the eye radius and perturbations are not too long. We note that no theoretical models have been proposed so far to explain, on mechanical grounds, the onset of the aqueous-vitreous substitute interface instability. Therefore, this exploratory work, in spite of the significant simplifying assumptions it is based on, represents a suitable starting point to understand the mechanics of this problem. In particular, we believe, it has the strength of allowing us to assess the role of all parameters involved in the instability mechanism.

Our findings are in qualitative agreement with empirical observations, to which they therefore provide a sound physical foundation. In particular, our results are in agreement with the observation that highly viscous vitreous substitutes are more resistant to emulsification than less viscous ones [81]-[82]. Moreover, the stabilizing role of the surface tension parameter is in agreement with empirical observations [83, 84], according to which the tendency to emulsification is significantly enhanced by the presence of surfactants that decrease the surface tension between the two fluids. Finally, the model predicts that the system becomes more unstable as the Reynolds number of the flow is increased, which explains why patients with increased eye mobility are more prone to develop emulsification [85]. Notwithstanding the fact that the stabilizing role of surface tension and the destabilizing role of the Reynolds number are not surprising from the mechanical point of view, the model allows us to quantify their effect.

In this analysis as a baseline dimensional values we have assumed $d^* = 3 \times 10^{-5}$ m for the thickness of the aqueous layer and $\sigma^* = 0.02$ N/m for the surface tension between two fluids. Figure 3.3.8(a) shows that the shortest unstable perturbation has a dimen- sional wavelength $L^*_{min} = L_{min} d^* \approx 5$ mm. This value has to be compared with the radius of the eye ($R^*_{eye} \approx 12$ mm). Following the above estimates, our models direct applicability to the eye might be questioned, since the length of the shortest unstable wave is not much smaller than the eye radius and, therefore, additional effects that have been neglected here, such as the sphericity of the domain, might not be negligible. Results, however, show that once additional effects are accounted for (possibly in combination to one another), such as, in particular, changes in the surface tension, increased eye mobility, or gravitational effects in the case in which the heavier fluid is on top of the lighter one, the wavelength of unstable perturbations is small enough for the model to be a good representation of the real case. Thus we can conclude that shear instability is likely to be a possible mechanism triggering the onset of vitreous substitutesaqueous interface instability.

Several other assumptions underlie the present work, which are listed and briefly discussed in the following.

Our stability analysis is based on the quasi-steady approach. In other words, we assume that a separation of time scales exists, such that perturbations evolve on a shorter time scale than the basic flow. This assumption holds in certain parameter regimes, on which we focus our attention. In particular, this implies considering large amplitude and relatively low frequency eye rotations. In figure 3.3.9 we report a verification of the scale separation, by plotting the contour lines of the ratio $\alpha\mathcal{R}(\Omega)/\omega$ of the perturbation frequency to the frequency of the basic flow (dashed curves). In the figure we also plot, with the solid line, the neutral

stability curve corresponding to $m = 5$, the same as shown in figure 3.3.5. As discussed earlier, in order for the assumption of scale separation to hold the ratio $\alpha\mathcal{R}(\Omega)$should be significantly larger than one in most of the unstable region. This is indeed shown to be the case in the figure. The same analysis has been carried out for all results.

In order to account for high frequency oscillations of the wall, a stability analysis based Floquets theory should be adopted [86].

We assume that the retina has a perfectly smooth surface. In reality, the retinal surface is characterized by a roughness that might have an amplitude comparable to the thickness of the aqueous layer, when the latter is very thin. The presence of this roughness is likely to contribute to the destabilization of the interface between the two fluids.

We assume periodic rotations of the eye. Real eye rotations are not necessarily periodic and not sinusoidal in time. Adoption of a more realistic time law for the wall motion might have some influence on the results.

We focus our attention on the instability mechanism induced by shear between the two fluids. In the case of incomplete filling of the vitreous chamber with the vitreous substi- tute, a thick pocket of aqueous forms in the chamber (see figure 3.3.2). In this case, the interface instability can also be triggered by other physical mechanisms, such as sloshing.

Accounting for all complexities inherent to the real fluid motion inside an eye in the presence of vitreous replacement fluids would need a fully numerical approach to the problem. However, we strongly believe that stability analyses such as the one proposed here can contribute to highlight basic physical mechanisms and are an indispensable tool to guide and interpret more realistic numerical simulations.

Chapter 4

Conclusions

The aim of this thesis was to build mathematical models describing fluid motion in the vitreous chamber of the human eye in order to obtain a better understanding of the stress distribution on the retina in the presence of some pathologies, that usually lead to retinal detachment. In addition, we consider a motion of tamoponade fluids injected into the vitreous chamber after the vitrectomy with the aim of understanding different possible complications related to thie usage from the mechanical point of view.

We first considered the motion of the natural vitreous humor in the vitreous chamber in the presence of some pathologies, that lead to retinal detachment. In particular, we considered vitreous humor liquefaction, vitreoschisis and focal vitreoretinal tractions. It has been found in clinical practice that these pathologies put patients under higher risk of developing macular holes, macular puckers and, consequently, retinal detachment. We modelled the vitreous chamber as a sphere filled with viscous or viscoelastic fluid. The viscoelastic fluid has been considered since the natural vitreous humor has an elastic component.

In order to study the retinal tractions in the presence of vitreoschisis, a split in vitreous cortex, we considered a mathematical model based on the assumption that the thickness of the split is much smaller the the radius of the eye. The results showed that in the re-joining points of the split the retina experiences higher stresses with respect to the normal case with no vitreoschisis present. These results are in a good agreement with the available clinical observations.

Inhomogeneous properties of the vitreous humor might be another possible factor leading to high retinal tractions. We set up a mathematical model, assuming that the vitreous chamber has a spherical shape and it is filled with a fluid the properties of which vary in space. The results show that in the regions with stronger adherence the stresses exerted on the retina are higher with respect to the rest of the domain.

The presence of the hydrophobic tamponade fluid in the vitreous chamber leads to the formation of an aqueous layer between the vitreous substitute and the retina. We studied the tamponating effect of the two most commonly used fluids: silicone oil and itraocular gas. The tamponated surface strongly depends on the shape of the interface between the tamponade fluid and the aqueous humor. We computed such an interface and the corresponding tamponated surface in the real eye domain. The results show that the gas has a better tamponating effect with respect to the silicone oil due to higher contact angle and larger density difference with water. In the case of myopic eyes the tamponating effect is reduced with respect to the normal eye using same volume fraction of tamponade fluid.

We also studied how the stresses exerted on the retina change due to the presence of a thin layer of aqueous humor, by setting up a simple mathematical model, where the vitreous chamber is assumed to have a spherical shape and it is filled with two fluids placed concentrically. The inner layer is the vitreous humor, which is a viscoelastic fluid, and the outer layer, attached to the boundary, is the aqueous humor. The results showed that the stresses exerted on the retina are significantly reduced when an aqueous layer is present and when the thickness of this layer is large enough the wall does not feel the presence of the oil at all. In addition, we also investigated the role of the visosity of the tamponade fluid. The wall shear stress increases in a nonlinear way with viscosity and attains a limiting value for large viscosity, which can be predicted analytically.

Emulsification is one of the most common complications related to the use of silicone oils. The mechanisms leading to the formation of emulsion are still poorely understood. However, it is believed that shear instability might be a major factor. We set up a simple mathematical model based on the assumption that the thickness of the aqueous humor in contact with the retina is much smaller than the radius of the eye, and studied the linear stability of the interface between the tamponade fluid and the aqueous humor. We found that instability is possible in a range of parameters that can occur in real eyes.

Acknowledgements

Firs of all I would like to express my deep and sincere gratitude to my advisor Rodolfo Repetto for his constant support and faith in me.

Moreover, I would like to thank my co-advisor, Jan Oscar Pralits, for his support throughout the years of my PhD and encouragement during my first presentations.

Besides my advisors, I would like to thank all my office collegues for all that fun that we had during scientific and not scientific discussion. A special thank to Davide, who was keeping me company in the office and to Daniele who truly understands the beauty of spherical harmonics. Thank you Peyman for your priceless advices.

My sincere thanks goes to my girlsfriends - Masha, Irene, Valeria, Lisa, Inna for their constant support and presence in all the difficult and happy moments.

I would like to thank also to my good and closest friends Sashko and Alex who were there for me all the time even being so far away.

Finally, I would like to thank my family: my parents, my sister, my nieces Marta and Marianna for believing in me, for being there all the time. And the very special thanks' goes to my grandmother.

Appendices

Appendix A

Volume of fluids method

The complexity of modeling two-phase flows arises from the presence of an interface surface where the physical properties are not continuous (density, viscosity etc.). This surface may be considered as a moving boundary, where a proper boundary conditions must be imposed. The evolution of such interface then is considered as a part of the solution.

There are many methods which are dealing with the interface tracking. The most popular of those are: the front tracking method [87], where the interface is modeled as a set of connected markers; the Level Set method [88], where the interface is a zero leverl set of signed distance function; and Volume of Fluid method (VOF).

The VOF method has been used in a large range of applications for both compressible and incomressible flows. The basic idea is as follows. Imagine a fixed grid on the comutational domain, and assign values to each cell based on the fraction of that cell. Given two phases (fluid 1 and fluid 2) and the interface separating them, we assing a value of unity to those cells containing fluid 1, a cell value of zero to those cells containing fluid 2, and a fraction between 0 and 1 to cells that contain interface:

$$C_{i,j} = \begin{cases} 1, & \text{if cell } (i,j) \text{ is occuied by fluid 1,} \\ 0, & \text{if cell } (i,j) \text{ is occuied by fluid 2,} \\ (0,1) & \text{if cell } (i,j) \text{ contains the interface.} \end{cases} \tag{A.0.1}$$

For the simplicity let us consider a two-dimensional domain. If $\chi(x,y)$ is the characteristic function, then the fraction function for each cell (i,j) is given by

$$C_{i,j} = \frac{1}{\Delta x \Delta y} \int_0^{\Delta x} \int_0^{\Delta y} \chi(x,y) dx dy, \tag{A.0.2}$$

where Δx and Δy are the grid size. Since χ is passibely advected with the flow, its material derivative is equal to zero:

$$\frac{\partial \chi}{\partial t} + \mathbf{V} \cdot \nabla \chi = 0 \tag{A.0.3}$$

, where $\mathbf{V} = [u, v]$ is the velocity vector. The velocity vector is divergence free:

$$\nabla \cdot \mathbf{V} = \frac{\partial u}{\partial x} + \frac{\partial v}{\partial y} = 0, \tag{A.0.4}$$

which gives

$$\frac{\partial \chi}{\partial t} + \frac{\partial (\chi u)}{\partial x} + \frac{\partial (\chi v)}{\partial y} = 0. \tag{A.0.5}$$

Figure A.0.1: Values of the fraction function C in different computational cells. When cell is completely occupied by the fluid 1 (blue region), the value of C in this cell is equal to 1; when the cell is occupied by the fluid 2 (empty region), its value is equal to 2; and it takes intermediate values in the cells that contain interface.

Let us denote by $C^n_{i,j}$ the value of C in n-th timestep for (i,j)-th cell and by $F^n_{i,j}$, $G^n_{i,j}$ the flux of volume fraction C leaving the cell (i,j) in the direction x and y respectively. We thus have:

$$\frac{C^{n+1}_{i,j} - C^n_{i,j}}{\Delta t} = \frac{F^n_{i-1/2,j} - F^n_{i+1/2,j}}{\Delta x} + \frac{G^n_{i,j-1/2} - G^n_{i,j+1/2}}{\Delta y}, \tag{A.0.6}$$

which can be solved for $C^{n+1}_{i,j}$ when the fluxes are computed.

The way of computing fluxes depends on the chosen fluid interface representation. Many techniques have been developed to include pitched slopes and curved surfaces.

The advantage of using VOF method is in its Eulerian nature, which allows to avoid many of the Lagrangian time step and topological change problems. However, there are some drawbacks related to the use of the VOF method:

- With respect to other methods such technique is less accurate.
- Evolution under complex speed functions is problematic. The results strongly depend on the orientation of the grid. The problem becomes even more complicated to deal with in non-convex cases.
- Calculation of geometric properties, such as curvature and normal, can be icaccurate.
- An additional efforts are required when a more accurate schemes are desirable.

Appendix B

Basic concepts of elasticity

Viscoelastic materials have both viscous and elastic properties and the relationship between stress and strain they experience is time-dependent. In our work we consider only linear viscoelasticity. One on the most convenient tool to present such approach is the spring-dashpot models.

We consider the stres relaxation and the creep of a linear viscoelastic material in responce to applied single-step shear strain. Note that in the ideal viscous fluids the stress is proportional to the strain rate and in purely elastic solids the stress is proportional to the strain.

When a shear strain of the form $\gamma(t) = \gamma_0 H(t)$ is applied, where $H(t)$ is a Heaviside function

$$H(t) = \begin{cases} 0, & \text{if } t < 0, \\ 1, & \text{if } t \geq 0, \end{cases} \tag{B.0.1}$$

then the resulting stress in a purely elastic solid is again a step function

$$\tau(t) = \tau_0 H(t), \tag{B.0.2}$$

(Figure B.0.1(a)). In purely viscous fluid the responce would be instantaneously infinite for $t = 0$ and equal to zero at any other time (Figure B.0.1(b)).

In the case of viscoelastic material, the properties of which are in between these two liminting cases, the responce can be described by the stress relaxation function R, which is continuous and antisymmetric with respect to γ function:

$$R(\gamma, t) = G(t)\gamma + O(\gamma^3), \tag{B.0.3}$$

where $G(t)$ is a linear stress relaxation modulus. In Figure B.0.2 we plot the resulting responce to the step shear strain in the case of viscoelastic material.

In the case when stress $\tau(t) = \tau_0 H(\tau)$ is applied, the resulting strain in an elastic solid would be $\gamma(t) = \gamma_0 H(t)$ and in a viscous fluid $\gamma(t) = \tau_0 t/\eta$, where η is a fluid viscosity.

The responce of a viscoelastic material is again in between these two cases, and it is described by the creep function

$$C(\tau, t) = J(t)\tau + O(\tau^3), \tag{B.0.4}$$

where $J(t)$ is called the linear creep complience.

In order to describe the linear viscoelasticity we consider a spring-dashpot model, where the spring represents an ideal elastic element with a linear relaxation modulus $G(t) = \mu H(t)$ and a linear creep complience $J(t) = H(t)/\mu$, where μ is a spring constant. The dashpot, on the other hand, represents an ideal viscous element with $G(t) = \eta\delta(t)$ and $J(t) = tH(t)/\eta$, where η is a dashpot constant.

When two elements are connected in series, their compliences add while their relaxation moduli are equal, whereas when they are connected in parallel, their moduli add and their compliences are equal.

The input signal can be approximated by a sum of step functions. Then, owing to the linearity, the final responce is given by the sum of responces to single steps. In the limit of infinitesimal small steps the stress-relaxation is given by the integral

$$\tau(t) = \int_{-\infty}^{t} G(t-t')d\gamma(t') \tag{B.0.5}$$

and creep is given by

$$\gamma(t) = \int_{-\infty}^{t} J(t-t')d\tau(t'). \tag{B.0.6}$$

However a step shear is really difficult to achieve in practice. Let us consider a sinusoidal shear strain

$$\gamma = \hat{\gamma}\exp(i\omega t). \tag{B.0.7}$$

Hence

$$\tau = \sigma\exp(i\omega t). \tag{B.0.8}$$

Note that $\dot{\gamma} = i\omega\hat{\gamma}\exp(i\omega t)$. Then

$$\hat{\sigma}\exp(i\omega t) = i\omega\hat{\gamma}\int_{-\infty}^{t} G(t-t')\exp(i\omega t')dt'. \tag{B.0.9}$$

We define complex modulus $\tilde{G}$ as the ratio $\hat{\sigma}/\hat{\gamma}$ and its given by

$$\tilde{G}(\omega) = \frac{\hat{\sigma}}{\hat{\gamma}} = i\omega\int_{0}^{\infty} G(s)\exp(-i\omega s)ds, \tag{B.0.10}$$

where $s = t - t'$.

The real part of the complex modulus $\mathcal{R}(\tilde{G}(\omega))$ is called the storage modulus and the imaginary part $\mathcal{I}(\tilde{G}(\omega))$ - loss modulus.

$$G'(\omega) = \mathcal{R}(\tilde{G}(\omega)); \quad G''(\omega) = \mathcal{I}(\tilde{G}(\omega)). \tag{B.0.11}$$

Then the complex viscosity $\tilde{\eta}$ is given by

$$\tilde{\eta} = \eta' - i\eta'' = \frac{\tilde{G}}{i\omega} = \frac{G''}{\omega} - i\frac{G'}{\omega}. \tag{B.0.12}$$

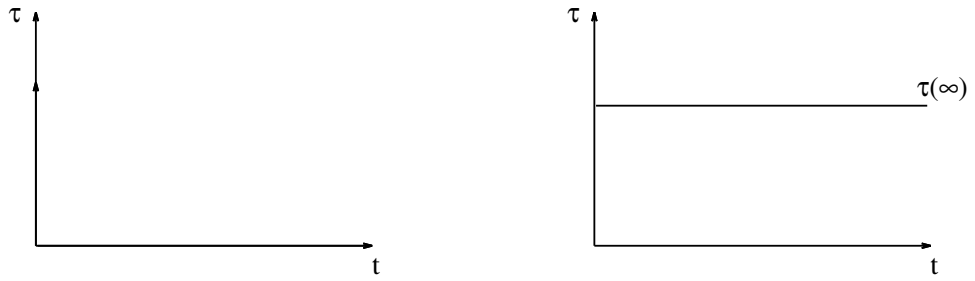

(a) (b)

Figure B.0.1: Viscous (a) and elastic (b) responces to the step shear strain.

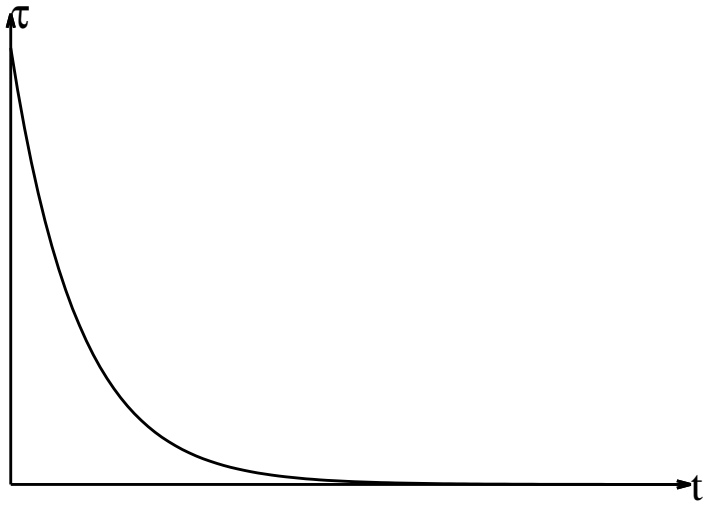

Figure B.0.2: Responce to an applied step shear strain in a case of viscoelastic material

Bibliography

[1] T. David, S. Smye, T. Dabbs, and T. James. A model for the fluid motion of vitreous humour of the human eye during saccadic movement. *Phys. Med. Biol.*, 43:1385–1399, 1998.

[2] Julia Meskauskas, Rodolfo Repetto, and Jennifer H. Siggers. Oscillatory motion of a viscoelastic fluid within a spherical cavity. *Journal of Fluid Mechanics*, 685:1–22, 2011.

[3] Krystyna Isakova, Jan O Pralits, Rodolfo Repetto, and Mario R Romano. Mechanical models of the dynamics of vitreous substitutes. *BioMed Research International*, 2014, 2014.

[4] Krystyna Isakova, Jan O Pralits, Rodolfo Repetto, and Mario R Romano. A model for the linear stability of the interface between aqueous humor and vitreous substitutes after vitreoretinal surgery. *Physics of Fluids*, 26(12):124101, 2014.

[5] David A. Atchison and George Smith. *Optics of the human eye*. Butterworth-Heinemann, 2000.

[6] David A. Atchison, Catherine E. Jones, Katrina L. Schmid, Nicola Pritchard, James M. Pope, Wendy E. Strugnell, and Robyn A. Riley. Eye shape in emmetropia and myopia. *Investigative Ophthalmology & Visual Science*, 45(10):3380–3386, October 2004.

[7] Pooria Sharif-Kashani, Jean-Pierre Hubschman, Daniel Sassoon, and H Pirouz Kavehpour. Rheology of the vitreous gel: effects of macromolecule organization on the viscoelastic properties. *Journal of Biomechanics*, 44(3):419–423, February 2011. PMID: 21040921.

[8] Einar Stefánsson. Physiology of vitreous surgery. *Graefe's archive for clinical and experimental ophthalmology*, 247(2):147–163, 2009.

[9] J. Xu, J. J. Heys, and V. H. Barocas. Permeability and diffusion in vitreous humor: implications for drug delivery. *Pharmaceutical Research*, 17(6):664–669, 2000.

[10] R. L. Zimmerman. In vivo measurements of the viscoelasticity of the human vitreous humor. *Biophys. J.*, 29:539–544, 1980.

[11] Paul N. Bishop. Structural macromolecules and supramolecular organisation of the vitreous gel. *Progress in Retinal and Eye Research*, 19(3):323–344, May 2000.

[12] J. Sebag. *The vitreous: Structure, Function and Pathobiology*. Springer and Verlag, 1989.

[13] S. Donati, S.M. Caprani, and G. Airaghi et al. Vitreous substitutes: the present and the future. *BioMed research international*, 2014.

[14] H Stevie Tan, Sarit Y Lesnik Oberstein, Marco Mura, and Heico M Bijl. Air versus gas tamponade in retinal detachment surgery. *British Journal of Ophthalmology*, 97(1):80–82, 2013.

[15] Dennis M Marcus, Donald J D'Amico, and Shizuo Mukai. Pneumatic retinopexy versus scleral buckling for repair of primary rhegmatogenous retinal detachment. *International ophthalmology clinics*, 34(3):97–108, 1994.

[16] Aranzazu Mateo-Montoya and Marc D de Smet. Air as tamponade for retinal detachments. *European journal of ophthalmology*, 24(2):242–246, 2013.

[17] Ahmad M Mansour. Pneumatic retinopexy for inferior retinal breaks. *Ophthalmology*, 112(10):1771–1776, 2005.

[18] Eric J Sigler, John C Randolph, Steve Charles, and Jorge I Calzada. Intravitreal fluorinated gas preference and occurrence of rare ischemic postoperative complications after pars plana vitrectomy: a survey of the american society of retina specialists. *Journal of ophthalmology*, 2012, 2012.

[19] John T Thompson. The absorption of mixtures of air and perfluoropropane after pars plana vitrectomy. *Archives of ophthalmology*, 110(11):1594–1597, 1992.

[20] Francesco Baino. Towards an ideal biomaterial for vitreous replacement: Historical overview and future trends. *Acta biomaterialia*, 7(3):921–935, 2011.

[21] Ingrid U Scott, Timothy G Murray, Harry W Flynn, William J Feuer, Joyce C Schiffman, Perfluoron Study Group, et al. Outcomes and complications associated with giant retinal tear management using perfluoro-n-octane. *Ophthalmology*, 109(10):1828–1833, 2002.

[22] Jerzy Mackiewicz, Kristel Maaijwee, Christoph Lüke, Norbert Kociok, Wilfried Hiebl, Hasso Meinert, and Antonia M Joussen. Effect of gravity in long-term vitreous tamponade: in vivo investigation using perfluorocarbon liquids and semi-fluorinated alkanes. *Graefe's Archive for Clinical and Experimental Ophthalmology*, 245(5):665–675, 2007.

[23] Teri T Kleinberg, Radouil T Tzekov, Linda Stein, Nathan Ravi, and Shalesh Kaushal. Vitreous substitutes: a comprehensive review. *Survey of ophthalmology*, 56(4):300–323, 2011.

[24] Maiko Inoue, Aya Iriyama, Kazuaki Kadonosono, Yasuhiro Tamaki, and Yasuo Yanagi. Effects of perfluorocarbon liquids and silicone oil on human retinal pigment epithelial cells and retinal ganglion cells. *Retina*, 29(5):677–681, 2009.

[25] Giovanni G Giordano and Miguel F Refojo. Silicone oils as vitreous substitutes. *Progress in polymer science*, 23(3):509–532, 1998.

[26] Joachim H Dresp and Dirk-Henning Menz. The phenomenon of sticky silicone oil. *Graefe's Archive for Clinical and Experimental Ophthalmology*, 245(6):863–868, 2007.

[27] J. Sebag. Vitreoschisis. *Graefes Archive for Clinical and Experimental Ophthalmology*, 246(3):329–332, March 2008. WOS:000252992000001.

[28] R. Dyson, A. J. Fitt, O. E. Jensen, N. Mottram, D. Miroshnychenko, S. Naire, R. Ocone, J. H. Siggers, and A. Smithbecker. Post re-attachment retinal re-detachment. In *Proceedings of the Fourth Medical Study Group, University of Strathclyde, Glasgow*, 2004.

[29] R. Repetto. An analytical model of the dynamics of the liquefied vitreous induced by saccadic eye movements. *Meccanica*, 41:101–117, 2006.

[30] A. Stocchino, R. Repetto, and C. Cafferata. Eye rotation induced dynamics of a newtonian fluid within the vitreous cavity: the effect of the chamber shape. *Phys. Med. Biol.*, 52:2021–2034, 2007.

[31] R. Repetto, J. H. Siggers, and A. Stocchino. Mathematical model of flow in the vitreous humor induced by saccadic eye rotations: effect of geometry. *Biomechanics and Modeling in Mechanobiology*, 9(1):65–76, 2010.

[32] Omid Abouali, Amirreza Modareszadeh, Alireza Ghaffarieh, and Jiyuan Tu. Investigation of saccadic eye movement effects on the fluid dynamic in the anterior chamber. *Journal of biomechanical engineering*, 134(2):021002, February 2012. PMID: 22482669.

[33] Julia Meskauskas, Rodolfo Repetto, and Jennifer H Siggers. Shape change of the vitreous chamber influences retinal detachment and reattachment processes: is mechanical stress during eye rotations a factor? *Investigative ophthalmology & visual science*, August 2012. PMID: 22899755.

[34] Roger I. Tanner. *Engineering Rheology*. Oxford University Press, USA, 2 edition, May 2000.

[35] Charles S Nickerson, John Park, Julia A Kornfield, and Hampar Karageozian. Rheological properties of the vitreous and the role of hyaluronic acid. *Journal of Biomechanics*, 41(9):1840–6, 2008.

[36] KE Swindle, PD Hamilton, and N Ravi. In situ formation of hydrogels as vitreous substitutes: Viscoelastic comparison to porcine vitreous. *Journal of Biomedical Materials Research - Part A*, 87A(3):656–665, December 2008.

[37] N.Soman and R.Banerjee. Artificial vitreous replacements. 17, March 2002. BJM shcool of Bioscience and Bioengineering, Biomedical Engineering Division, Indian Institute of Technology, Bombay.

[38] K. E. Swindle and N. Ravi. Recent advances in polymeric vitreous substitutes. *Expert Rev Ophthalmol.*, 2(2):255–265, 2007.

[39] Andrea Bonfiglio, Alberto Lagazzo, Rodolfo Repetto, and Alessandro Stocchino. An experimental model of vitreous motion induced by eye rotations. *Eye and Vision*, 2(1):10, 2015.

[40] J Sebag and EA Balazs. Morphology and ultrastructure of human vitreous fibers. *Investigative ophthalmology & visual science*, 30(8):1867–1871, 1989.

[41] WR Green and J Sebag. Vitreoretinal interface. *Retina*, 3:1882–1960, 2006.

[42] Claude LMH Navier. *Mémoire sur les lois de l'équilibre et du mouvement des corps solides élastiques*. 1827.

[43] Martin Z Bazant and Olga I Vinogradova. Tensorial hydrodynamic slip. *Journal of Fluid Mechanics*, 613:125–134, 2008.

[44] R L Pickett-Seltner, M J Doughty, J J Pasternak, and J G Sivak. Proteins of the vitreous humor during experimentally induced myopia. *Investigative Ophthalmology & Visual Science*, 33(12):3424–3429, November 1992. PMID: 1428715.

[45] N Ueno. [changes in vitreous structure caused by oxygen free radicals]. *Nippon Ganka Gakkai Zasshi*, 99(12):1342–1360, 1995.

[46] Wallace S Foulds. Role of vitreous in the pathogenesis of retinal detachment. In Sebag J., editor, *Vitreous in Health and Disease*, pages 375–393. Springer-Verlag, 2014.

[47] Mario R Romano, Ronald Das, Carl Groenwald, Theo Stappler, Joaquin Marticorena, Xavier Valldeperas, David Wong, and Heinrich Heimann. Primary 23-gauge sutureless vitrectomy for rhegmatogenous retinal detachment. *Indian journal of ophthalmology*, 60(1):29, 2012.

[48] Donald J D'Amico. Primary retinal detachment. *New England Journal of Medicine*, 359(22):2346–2354, 2008.

[49] Stephen F Oster, Francesca Mojana, Dirk-Uwe G Bartsch, Michael Goldbaum, and William R Freeman. Dynamics of the macular hole-silicone oil tamponade interface with patient positioning as imaged by spectral domain optical coherence tomography. *Retina (Philadelphia, Pa.)*, 30(6):924, 2010.

[50] John D Scott. Prevention and perspective in retinal detachment. *Eye*, 3(5):491–515, 1989.

[51] IM Fawcett, RL Williams, and D Wong. Contact angles of substances used for internal tamponade in retinal detachment surgery. *Graefe's archive for clinical and experimental ophthalmology*, 232(7):438–444, 1994.

[52] Ian Eames, Romesh I. Angunawela, G. William Aylward, and Ali Azarbadegan. A theoretical model for predicting interfacial relationships of retinal tamponades. *Investigative Ophtalmology & Visual Science*, 51:2243–2247, 2010.

[53] Suraj S Deshpande, Lakshman Anumolu, and Mario F Trujillo. Evaluating the performance of the two-phase flow solver interfoam. *Computational science & discovery*, 5(1):014016, 2012.

[54] Cyril W Hirt and Billy D Nichols. Volume of fluid (vof) method for the dynamics of free boundaries. *Journal of computational physics*, 39(1):201–225, 1981.

[55] Openfoam. http://www.openfoam.com/.

[56] Jan-Willem M Beenakker, Denis P Shamonin, Andrew G Webb, Gregorius PM Luyten, and Berend C Stoel. Automated retinal topographic maps measured with magnetic resonance imagingretinal topographic maps measured with mri. *Investigative ophthalmology & visual science*, 56(2):1033–1039, 2015.

[57] J.W.M.Beenakker, G. van Rijn, G.P.M.Luyten, and A.G.Webb. High resolution in vivo and in vitro imaging of uveal melanoma. *NMR Biomed*, 3041, October 2013.

[58] Bruce A Berkowitz. Mri of retinal and optic nerve physiology. *NMR in Biomedicine*, 21(9):927–927, 2008.

[59] C. Pozrikidis. *Fluid dynamic theory computation and numerical simulation.* Kluwer academic publishers, 2001.

[60] D Wong, JC Van Meurs, T Stappler, C Groenewald, IA Pearce, JN McGalliard, E Manousakis, and EN Herbert. A pilot study on the use of a perfluorohexyloctane/silicone oil solution as a heavier than water internal tamponade agent. *British journal of ophthalmology*, 89(6):662–665, 2005.

[61] Roxane J Hillier, Theodor Stappler, Rachel L Williams, George S Turner, and David Wong. The impact of axial length on retinal tamponade for gas, silicone oil, and heavy silicone oil, using an in vitro model. *Graefe's Archive for Clinical and Experimental Ophthalmology*, 249(5):671–675, 2011.

[62] MR Romano, T Stappler, J Marticorena, C Groenewald, I Pearce, SK Gibran, D Wong, and H Heimann. Primary vitrectomy with densiron-68 for rhegmatogenous retinal detachment. *Graefe's Archive for Clinical and Experimental Ophthalmology*, 246(11):1541–1546, 2008.

[63] Mario R Romano, Stefano Zenoni, Paolo Arpa, and Cesare Mariotti. Mixture of ether and silicone oil for the treatment of inferior complicated retinal detachment. *European journal of ophthalmology*, 23(2):230–235, 2012.

[64] Parul Ichhpujani, Anjana Jindal, and L Jay Katz. Silicone oil induced glaucoma: a review. *Graefe's Archive for Clinical and Experimental Ophthalmology*, 247(12):1585–1593, 2009.

[65] Martin Winter, Wolfgang Eberhardt, Christian Scholz, and Andreas Reichenbach. Failure of potassium siphoning by muller cells: a new hypothesis of perfluorocarbon liquid–induced retinopathy. *Investigative ophthalmology & visual science*, 41(1):256–261, 2000.

[66] D De Silva, KS Lim, and WE Schulenburg. An experimental study on the effect of encircling band procedure on silicone oil emulsification. *Investigative Ophthalmology & Visual Science*, 45(13):2038–2038, 2004.

[67] Yau Kei Chan, Chiu On Ng, Paul C Knox, Michael J Garvey, Rachel L Williams, and David Wong. Emulsification of silicone oil and eye movements. *Investigative ophthalmology & visual science*, 52(13):9721–9727, 2011.

[68] Yasin Toklu, Hasan B Cakmak, Sule B Ergun, Mucella A Yorgun, and Saban Simsek. Time course of silicone oil emulsification. *Retina*, 32(10):2039–2044, 2012.

[69] Marco Piccirelli, Oliver Bergamin, Klara Landau, Peter Boesiger, and Roger Luechinger. Vitreous deformation during eye movement. *NMR in biomedicine*, 25(1):59–66, January 2012. PMID: 21567512.

[70] P.J. Blennerhassett and A.P. Bassom. On the linear stability of stokes layers. 14, 2008.

[71] Chin-Hsiu Li. Instability of time-periodic flows of stratified fluids. 13(5), May 1970.

[72] P.Hall. The linear stability of flat stokes layer. 17, 1977. Mathematics department and Physiological flow studies unit, Imperial College, London, S.W.7, U.K.

[73] Christian Von Kerczek and Stephen H Davis. Linear stability theory of oscillatory stokes layers. *Journal of Fluid Mechanics*, 62(04):753–773, 1974.

[74] Chia-Shun Yih. Instability of a horizontal liquid layer on an oscillating plane. 31, 1968.

[75] AC Or. Finite-wavelength instability in a horizontal liquid layer on an oscillating plane. *Journal of Fluid Mechanics*, 335:213–232, 1997.

[76] HB Squire. On the stability for three-dimensional disturbances of viscous fluid flow between parallel walls. *Proceedings of the Royal Society of London. Series A, Containing Papers of a Mathematical and Physical Character*, pages 621–628, 1933.

[77] Peter W Conrad and William O Criminale Jr. The stability of time-dependent laminar flow: parallel flows. *Zeitschrift für angewandte Mathematik und Physik ZAMP*, 16(2):233–254, 1965.

[78] Peter J Schmid and Dan S Henningson. *Stability and transition in shear flows*, volume 142. Springer Science & Business Media, 2012.

[79] W. Becker. Metrics. In R.H. Wurtz and M.E. Goldberg, editors, *The neurobiology of saccadic eye movements*. Elsevier Science Publisher BV (Biomedical Division), 1989.

[80] M.E. Hammer. Vitreous substitutes. *Duane's Ophtalmology*, ISBN 9781451187441, 2013.

[81] Angela Crisp, Eugene de Juan, and James Tiedeman. Effect of silicone oil viscosity on emulsification. *Archives of ophthalmology*, 105(4):546–550, 1987.

[82] HANS-PETER HEIDENKUMMER, ANSELM KAMPIK, and SÖREN THIERFELDER. Experimental evaluation of in vitro stability of purified polydimethylsiloxanes (silicone oil) in viscosity ranges from 1000 to 5000 centistokes. *Retina*, 12(3):S28–S32, 1992.

[83] Naphtali Savion, Amir Alhalel, Giora Treister, and Elisha Bartov. Role of blood components in ocular silicone oil emulsification. *Investigative ophthalmology & visual science*, 37(13), 1996.

[84] JOACHIM H DRESP and Dirk-Henning Menz. Interaction of different ocular endotamponades as a risk factor for silicone oil emulsification. *Retina*, 25(7):902–910, 2005.

[85] T Yilmaz and M Güler. The role of nystagmus in silicone oil emulsification after pars plana vitrectomy and silicone oil injection for complex retinal detachment. *European journal of ophthalmology*, 18(1):150–154, 2007.

[86] PJ Blennerhassett and Andrew P Bassom. On the linear stability of stokes layers. *Philosophical Transactions of the Royal Society of London A: Mathematical, Physical and Engineering Sciences*, 366(1876):2685–2697, 2008.

[87] Grétar Tryggvason, Bernard Bunner, Asghar Esmaeeli, Damir Juric, N Al-Rawahi, W Tauber, J Han, S Nas, and Y-J Jan. A front-tracking method for the computations of multiphase flow. *Journal of Computational Physics*, 169(2):708–759, 2001.

[88] Stanley Osher and James A Sethian. Fronts propagating with curvature-dependent speed: algorithms based on hamilton-jacobi formulations. *Journal of computational physics*, 79(1):12–49, 1988.